Si NANOCRYSTALS IN SiC MATRIX AND INFRARED SPECTROSCOPY OF NANOCRYSTALS IN A DIELECTRIC MATRIX

A THESIS SUBMITTED TO
THE GRADUATE SCHOOL OF NATURAL AND APPLIED SCIENCES
OF
MIDDLE EAST TECHNICAL UNIVERSITY

BY

ARİFE GENCER İMER

IN PARTIAL FULFILLMENT OF THE REQUIREMENTS
FOR
THE DEGREE OF DOCTOR OF PHYLOSOPHY
IN
PHYSICS

APRIL 2010

Approval of the thesis:

Si NANOCRYSTALS IN SiC MATRIX AND INFRARED SPECTROSCOPY OF NANOCRYSTALS IN A DIELECTRIC MATRIX

submitted by **ARİFE GENCER İMER** in partial fulfillment of the requirements for the degree of **Doctor of Philosophy in Physics Department, Middle East Technical University** by,

Prof. Dr. Canan Özgen
Dean, Graduate School of **Natural and Applied Sciences** _____

Prof. Dr. Sinan Bilikmen
Head of Department, **Physics** _____

Prof. Dr. Raşit Turan _____
Supervisor, **Physics Dept., METU**

Examining Committee Members:

Prof. Dr. Mürvet Volkan
Chem. Dept., METU _____

Prof. Dr. Raşit Turan
Physics Dept., METU _____

Prof. Dr. Mehmet Parlak _____
Physics Dept., METU

Prof. Dr. Mehmet Erbudak
Physics Dept., ETH _____

Assoc. Prof. Dr. Hakan Altan _____
Physics Dept., METU

Date: **05.04.2010**

I hereby declare that all information in this document has been obtained and presented in accordance with academic rules and ethical conduct. I also declare that, as required by these rules and conduct, I have fully cited and referenced all material and results that are not original to this work.

Name, Last name : ARİFE GENCER İMER

Signature :

ABSTRACT

Si NANOCRYSTALS IN SiC MATRIX AND
INFRARED SPECTROSCOPY OF NANOCRYSTALS
IN A DIELECRIC MATRIX

Gencer İmer, Arife
Ph.D., Department of Physics
Supervisor : Prof. Dr. Raşit Turan

April 2010, 143 pages

This study focuses on various aspects of nanocrystals embedded in a dielectric matrix. In the first part of this work, a new approach with the use of Fourier Transform Infrared spectroscopy (FTIR) in the nanocrystal analysis was developed and presented. Si and Ge nanocrystals embedded in SiO_2 matrix were mainly studied. This new approach is based on the analysis of structural variations of SiO_2 matrix during the formation of semiconductor nanocrystlas. It is shown that the chemical and structural variations of the host matrix are directly related to the precipitation of nanocrystals in it. This correlation provides valuable information about the presences of nanocrystals in the matrix.

In the second part of this work, fabrication of SiC films with and without Si nanocrystals inclusions was studied. With this aim, stoichiometric SiC and Si rich SiC thin films were fabricated by using magnetron co-sputtering and Plasma Enhanced Chemical Vapor Deposition (PECVD) techniques. For SiC films, the

structural and optical analyses were performed. For Si rich SiC films, the formation conditions of Si nanocrystals were investigated. Post annealing studies were carried out to track the evolution of the SiC matrix and formation of Si nanocrystals at different temperatures. Chemical and structural properties of the SiC host matrix were investigated with FTIR spectroscopy. Optimum conditions for the fabrication of stoichiometric SiC layers were determined. The crystallography of the nanocrystals was investigated by X-Ray Diffraction (XRD). The variation of the atomic concentrations and bond formations were investigated with X-Ray Photoelectron Spectroscopy (XPS). Raman spectroscopy and Transmission Electron Microscopy (TEM) were used to verify the formation of Si nanocrystals. We have shown that both single and multilayer Si nanocrystals can be fabricated in the amorphous SiC matrix for applications such as light emitting diodes and solar cells.

Keywords: Magnetron Co-Sputtering, SiC, Si Nanocrystals, Fourier Transform Infrared Spectroscopy, Raman Spectroscopy, X-Ray Diffraction, X-Ray Photoelectron Spectroscopy.

ÖZ

SiC MATRİS İÇİNDEKİ Si NANOKRİSTALLER VE
DİELEKTRİK İÇİNDEKİ NANOKRİSTALLERİN KIZIL ÖTESİ
SPEKTROSKOPİSİ

Gencer İmer, Arife
Lisans Sonrası Doktora, Fizik Bölümü
Tez Yöneticisi : Prof. Dr. Raşit Turan

Nisan 2010, 143 sayfa

Bu calışma, dielektrik malzemeler içinde oluşturulan nanokristallerin çeşitli özellikerine odaklanmıştır. Çalışmanın birinci bölümünde, Fourier Dönüşümlü Kızıl Ötesi Spektroskopisinin (FTIR) nanokristal analizinde kullanımına yönelik yeni bir yaklaşım geliştirilmiş ve sunulmuştur. Bu yeni yaklaşımda, SiO_2 matris yapısında meydana gelen değişim incelenerek Si ve Ge nanokristallerin oluşumu hakkında bilgiye ulaşılmıştır. Matris yapısında meydana gelen değişikliklerin, nanokristal oluşumu ile doğrudan ilintili olduğu gösterilmiştir.

Çalışmanın ikinci bölümünde, SiC ve Si zengin SiC ince filmlerin üretimi çalışılmıştır. Bu amaca yönelik olarak, mıknatıslı eş-saçtırma ve plazmayla desteklenmiş kimyasal buhar biriktirme yöntemi ile çeşitli filmler üretilmiştir. SiC ince filmler için, yapısal ve optik analizler gerçekleştirilmiştir. Si zengin SiC örnekler için ise, Si nanokristallerin oluşum şartları araştırılmıştır. SiC matrisin ve Si nanokristallerin değişik sıcaklıklardaki evrimini incelemek için örnekler üretim

sonrası fırınlamaya tabi tutulmuştur. SiC matrisin stokiyometrik özellikleri FTIR yardımıyla incelenmiştir. Stoikiometrik SiC oluşumu için optimum şartlar belirlenmiştir. Si zengin SiC filmlerde, nanokristallerin kristalografik özellikleri ve boyutları X-Işını Kırınımı (XRD) tekniği ile belirlenmiştir. Atomik konsantrasyonlardaki değişim ve bağ oluşumları X-Işını Fotoelektron Spektroskopisi (XPS) ile incelenmiştir. Raman spectroskopisi ve geçişli elektron mikroskopisi yardımıyla Si nanokristallerin oluştuğu belirlenmiştir. Bu bilgiler ışığında çok katmanlı SiC ve Si zengin SiC yapı üretilmiş ve farklı analiz teknikleri kullanılarak yapısal ve optik özellikleri incelenmiştir. Bu çalışmada, ışık yayan aygıtlar ve güneş pili uygulamaları için amorf SiC matris içinde Si nanokristallerin başarı ile oluşturulabildiği gösterilmiştir.

Anahtar Kelimeler: Mıknatıslı Eş Saçtırma, SiC, Si Nanokristaller, X-Işını Kırınımı, Raman Spektroskopisi, X-Işını Fotoelektron Spektroskopisi

to my husband Mehmet and my son Ahmet Erdem; with Love...

ACKNOWLEDGEMENTS

I would like to thank to my supervisor Prof. Dr. Raşit Turan, for his continuous support, perceptiveness, encouragement. Without his guidance, it would be harder to improve my knowledge.

I also would like to thank to Prof. Dr. Mehmet Parlak, Prof. Dr. Mürvet Volkan, Prof. Dr. Mehmet Erbudak, and Assoc. Prof. Dr Hakan Altan for their critical comments and advices on my thesis.

I want to thank to my present and former group partners Ayşe Seyhan, Arif Sinan Alagöz, Buket Kaleli, Döndü Şahin, Fırat Es, İlker Doğan, Mehmet Karaman, Olgu Demircioğlu, Nader A. P. Moghaddam, Seda Bilgi, Sedat Canli, Seçkin Öztürk, Selçuk Yerci, Umut Bostancı, Urcan Güler, Z. Deniz Eygi for their friendliness and endless support during this work. I really learned a lot from them about variety of things. My special thanks goes to Mustafa Kulakcı, for his support both experimentally and mentally during the whole period of my study. I would like to thank to İlker Yıldız for XPS measurements and to Yücel Eke for his technical support. I thank METU Central Laboratory for valuable results they generated with XPS, XRD and SEM.

Besides my group members, I would like to thank to Selmin Ener, Emel Kilit, Dr. Kadir Gökşen, Elif Beklen, İpek Güler, E. Deniz Tekin, Özge Amutkan, Olcay Üzengi Aktürk, Volkan Çuha, Hakan Karaağaç, Halil Kuyrukçu, Murat Kaleli, Doğan Mansuroğlu, Nazım Dugan for their great friendship and making some heavy times enjoyable, and Arife Özdemir for special tea service on everydays.

I would like to thank to my best roommate Selcan Çuha for a lot of good time spent together, and Bahar Oğuz, Dr. Ayşegül Gümüş for being best friends and

neighbors, you will always with me. I am extremely grateful to my family members for their continued moral support, invaluable patience and love.

I would like to give my endless gratitude to my husband Mehmet İmer, who supported and motivated me with his understanding during the whole period of my study.

I would like to thank to Scientific and Technical Research Council of Turkey for financial support during this study.

TABLE OF CONTENTS

LIST OF TABLES

TABLES

LIST OF FIGURES

FIGURES

LIST OF ABBREVIATIONS

AS	Asymmetric Stretching
CB	Conduction Band
DC	Direct Current
DFT	Density Functional Theory
EDX	Energy Dispersive X-Ray
FTIR	Fourier Transform Infrared
FWHM	Full-Width Half-Maximum
GIXRD	Grazing Incidence XRD
HRTEM	High Resolution TEM
LA	Longitudinal Accustic
LDA	Local Density Approximation
LED	Light Emitting Diode
LO	Longitudinal Optical
MOS	Metal Oxide Semiconductor
MOSFET	Metal Oxide Semiconductor Field Effect Transistor
NC	Nanocrystal
PECVD	Plasma Enhanced Chemical Vapor Deposition

PVD	Physical Vapor Deposition
R_d	Deposition Rate
RF	Radio Frequency
R_H	Hydrogen Dilution Ratio
SAD	Selected Area Diffraction
SCCM	Standard Cubic Centimeters per Minute
SEM	Scanning Electron Microscopy
TEM	Transmission Electron Microscopy
TEOS	Tetra Ethyl Ortho Silicate
TO	Transverse Optical
UHV	Ultra High Vacuum
X_c	Methane Fraction
XPS	X-Ray Photoelectron Spectroscopy
XRD	X-Ray Diffraction
VB	Valance Band

CHAPTER 1

INTRODUCTION

1.1 Introduction

From the invention of the first transistor by Bardeen, Brattain and Shockly in 1947 to now, the microelectronic technology has been remarkably developed [1]. At that time nobody could imagine the level in today's technology. The incredible improvement in this technology follows the empirical theory predicted by Gordon Moore, co-fander of Intel, in 1965 [2]. The observation is stated that the density and the performance of integrated circuits doubles every two years, which is known as Moore's law [2,3]. Since that time, his observation stands in the microelectronic industry. In order to sustain the increase in the density of the transistor in a single chip, the feature size has to be shrunk further. Nowadays, transistor size is downscaled to 30 nm and billions of them can be put together in a single chip to form integrated circuits. If a material size is downscaled to nanometer order, the physical properties of the material are changed, due to the confinement of electrons. Most of the recent research efforts have been focusing on nanomaterials in order to control the size dependent physical properties and to apply in microelectronic and optoelectronic circuits [4-6]. Fabrication of materials in low dimension is also desirable to build denser, and more reliable devices for various technological applications. For instance, the charge storage reliability of flash memories is shown to be improved by the use of nanocrystals instead of continuous layer [7].

1.2 Semiconductor Nanocrystals : A Material System for New Electrical and Optical Applications

Semiconductor nanocrystals gain new and improved physical properties due to the size reduction. These new physical properties like enhancement of optical emission and absorption or better charge storage properties can be utilized in many applications. The following section summarizes some of the most promising applications of semiconductor nanocrystals which have been of interest in recent years.

1.2.1 Nanocrystal Based Flash Memory Cell

The metal oxide semiconductor field effect transistor (MOSFET) is one of the cornerstones of modern semiconductor technology. These types of structures can be used for different purposes in today's microelectronic industry. One of the applications of MOSFETs is in non-volatile flash memories. In conventional flash memories, a floating Si layer is completely surrounded by a dielectric, usually this is natural oxide SiO_2 as shown in Figure 1.1. The electrons can be injected or ejected from the tunneling oxide layer by Fowler-Nordheim tunneling [8]. The reliability and performance of these devices are dependent on the quality and thickness of the tunneling oxide [8]. The big disadvantage of these structures is that the tunneling oxide should be very thin, so as to allow the easy tunneling for write-erase operation. However, a thin oxide layer may also allow the undesired tunneling causing the loss of the information stored in that cell.

In order to overcome this problem and improve the reliability of the flash memory cells, Si nanocrystals have been proposed as an alternative charge storage medium [12].

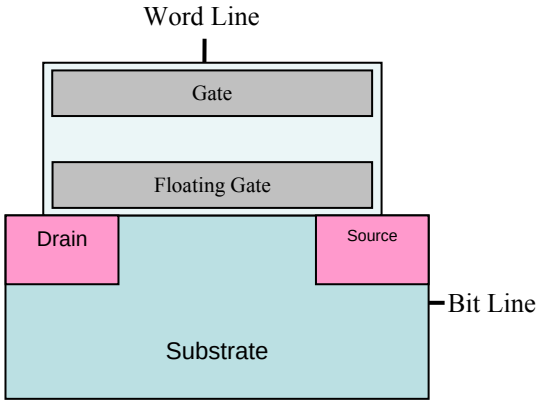

Figure 1.1 Schematic diagram of conventional floating gate flash memory cell

Recent developments showed [13,14] that a nanocrystal embedded in dielectric matrices can be used in classical flash memory cells. In nanocrystal based flash memory devices shown in Figure 1.2, a small leakage current through the tunneling oxide does minimize the loss of the information, because the charge pocket is stored in many independent nanocrystals and the information is preserved even if a few nanocrystals are shorted. The nanocrystal based flash memory devices have thus attracted great interest in recent years.

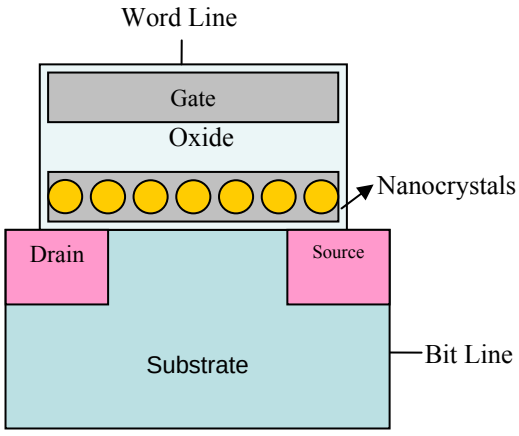

Figure 1.2 Schematic diagram of nanocrystal based flash memory cell

1.2.2 Light Emitting Devices with Nanocrystals

Another application of nanostructures is in the field of light emitting diode (LED), which is widely used as the optical component in electro-optical circuits. In most of the LED applications, II-VI and III-V compound semiconductors are commonly used owing to their high luminescence efficiency. Unfortunately, the production of these light emitting devices is not feasible in Si based microelectronic technology. This is due to the fact that the indirect band structure of bulk Si crystal does not allow efficient light emission (Figure 1.3). In order to generate a photon emission from the Si crystal, a phonon absorption/emission process is needed to satisfy the momentum conservation principle. This requirement reduces the probability of light emission from Si significantly.

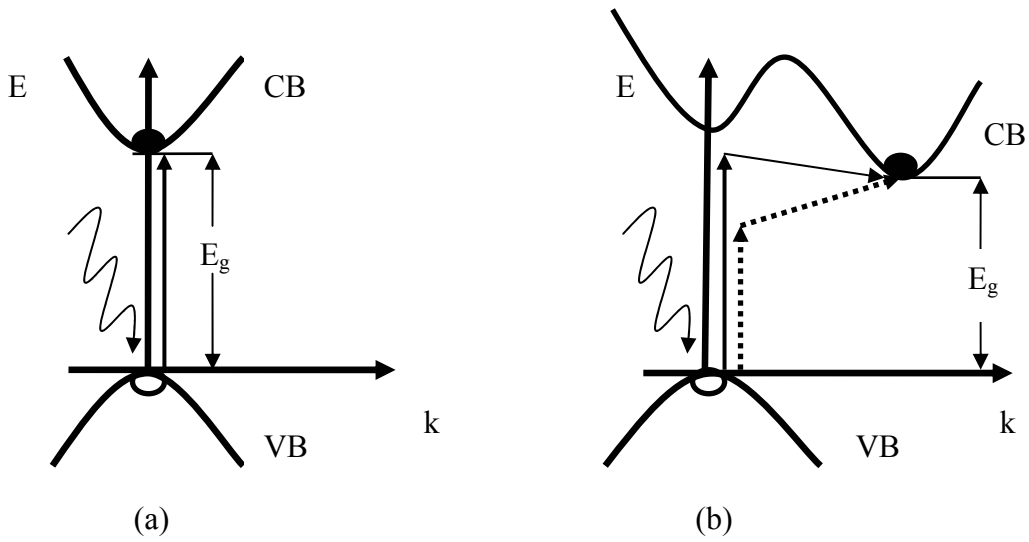

Figure 1.3 Schematic diagram for a) a direct transition of an exited electron by a photon absorption and b) an indirect transition of an exited electron by a photon absorption accompanied by phonon absorption (dashed arrow) or emission (solid arrow) from the valance band to the conduction band

This problem in making the Si crystal an efficient light emitter can be overcome by reducing the size of the crystal down to a few nanometers. The localization of the electrons in a quantum dot having a diameter of 1-5 nm satisfies the momentum conservation principle easily ($\Delta x \Delta p \geq \hbar/2$). This has been confirmed by many research laboratories experimentally. The observation of the photoluminescence from the Si nanocrystal has recently attracted a lot of attention in many leading research laboratories to fabricate a new class of optical and electro optical components with Si based light emission [9,10,11].

1.2.3. High Efficiency Solar Cells with Nanocrystals

One of the most exciting applications of nanocrystals has been in the field of photovoltaic conversion of solar energy, where nanocrystals offer a more efficient conversion due to the quantum size effect. The quantum confinement effect in Si nanocrystals allows us to adjust the bandgap Si, and thus makes it possible to cover the whole solar spectrum. In the conventional solar cell devices the most efficient absorption can only happen around the single bandgap energy of the main absorbing region of the device. The remaining part of the spectrum, which does not satisfy this condition, can not be absorbed efficiently.

Figure 1.4 shows the possible energy loss mechanisms in a standard p-n junction solar cell The two important power loss mechanisms in a p-n junction solar cell can occur if the incident photons have energy lower than the band gap (1) and the incident photon energy is higher than the band gap (2). In the former case, photons do not have enough energy to excite an electron from the valence band to the conduction band, whereas in the latter case, the excess energy is converted to the heat through a thermalization process. Other loss mechanism can also take part in junctions and contact which are not taken into the consideration for an ideal device. An ideal device can convert all absorbed photon to electrical signal. These loss mechanisms limit the maximum efficiency that can be obtained in a solar cell device (for Si, this limit is 31%). In order to fabricate solar cells with an

efficiency exceeding the limit, new type of devices using new concepts are needed. One such approach is to use multi-junction (tandem) structure in the same solar cell.

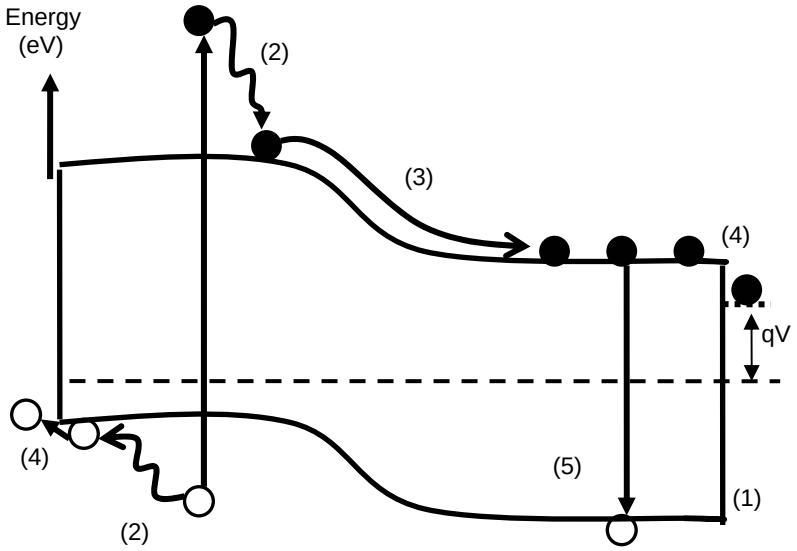

Figure 1.4. Loss mechanisms in a standard p-n junction solar cell: (1) nonabsorption of below-band gap photons, (2) lattice thermalization loss, (3) contact voltage loss, and (5) recombination loss [15].

The concept of a multilayer tandem solar cell shown in Figure 1.5 is based on the use of several solar cells containing different sizes of the nanocrystals in each layer stacked on top of each other [16]. Different parts of the solar spectrum are absorbed by different band regions of the solar cells. Thus, the efficiency of the solar cell exceeds the limit (called Schokly-Quessier limit) [15,16] and in principle can reach 100% for a solar cell with infinite number of junctions. Si nanocrystals imparted in a semiconductor or an oxide matrix is forming a promising material system where these types of solar cells are called “third generation solar cells”.

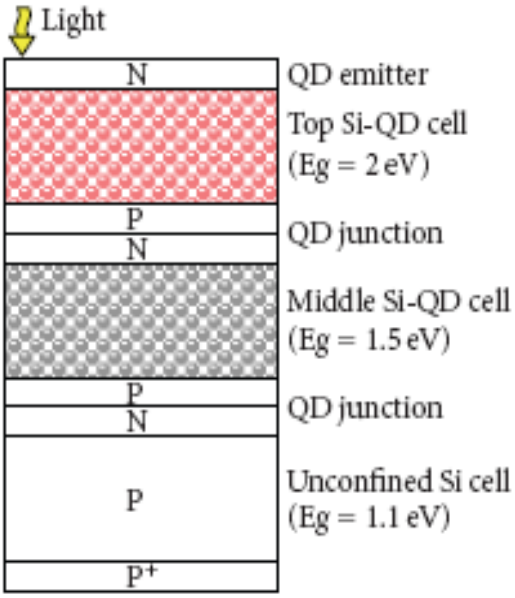

Figure 1.5. Schematic diagram of tandem solar cell with silicon substrate

1.3 SiC as an Alternative Host Matrix for Si Nanocrystals

Until very recently, SiO_2 which is natural oxide form of Si was commonly used as a dielectric host matrix for Si nanocrystals. Due to its applications in microelectronic industry, this matrix has been studied extensively [17-19]. The advantage of SiO_2 is that it is the natural oxide of Si, and it can be grown on Si by thermal oxidation. The disadvantage of the SiO_2 is its large band gap compared to Si which limits the carrier transport which is very important in device applications. Recently, some studies have concentrated on the search for alternative host matrix having smaller band gap compared to SiO_2 [15,16]. SiC appears to be a good candidate for these purposes as it is wide band gap semiconductor. The wide optical band gap of SiC makes the material suitable as a transparent medium [20]. Because of the high band gap energy (3.0 and 3.3 eV for 4H-SiC and 6H-SiC, respectively), leakage currents in SiC are many orders of magnitude lower than in Si, which has a band gap energy 1.12 eV [21,22]. Also, high thermal stability, high thermal conductivity, high electron mobility are the

key features for attractiveness of SiC for high temperature electronic applications [22,23]. Furthermore, SiC is the only compound semiconductor which can be thermally oxidized to form native oxide SiO_2 at temperature ~1100 °C [24]. This makes it possible to fabricate metal oxide semiconductor (MOS) type devices on SiC.

1.3.1 Physical Properties of SiC

Silicon carbide is a compound of silicon and carbon with a chemical formula SiC, which is called *carborundum*. 6H-SiC is usually fabricated by Lely process in the laboratory. 3C-SiC is usually deposited by chemical vapor deposition (CVD) [20]. Pure silicon carbide can also be prepared by the thermal decomposition of a polymer, poly(methylsilyne), under an inert atmosphere at low temperatures.

1.3.2 Structural Properties of SiC

SiC exists in about 250 polymorphic forms [25,26]. In all these polytypes of SiC, the bonding structure between Si and C is always tetrahedral. The simplest form of SiC is the cubic SiC in the zinc blende structure, which is known as 3C-SiC or β-SiC. The other common polytypes with a hexagonal lattice are called as 4H-SiC, and 6H-SiC or α-SiC [25]. The difference between them is in the stacking planes of the Si–C bi-layers along the *c* axis.

The other polytypes of SiC having rhombohedral structure are labelled as 15R-SiC, 21R-SiC, that is the rare and complex polytypes of SiC, with an increasingly complex stacking sequence along the axial direction [26]. Their lattice parameters and the information about the properties of major polytypes of SiC are summarized in Table 1.1.

Table 1.1 Properties of major SiC polytypes

Polytype	3C (β)	4H	6H (α)
Crystal structure	Zinc blende (cubic)	Hexagonal	Hexagonal
Space group	T^2_d-F43m	C^4_{6v}-$P6_3mc$	C^4_{6v}-$P6_3mc$
***Pearson symbol**	cF8	hP8	hP12
Lattice constants (Å)	4.3596	3.0730; 10.053	3.0730; 15.11
Density (g/cm^3)	3.21	3.21	3.21
Bandgap (eV)	2.36	3.23	3.05
Thermal conductivity (W/(cm·K))	3.6	3.7	4.9

(*Pearson symbol describes crystal structure; 1st letter for the crystal class, 2nd letter for the lattice type, the number for the number of atoms in the unit cell.)

The high sublimation temperature of SiC (approximately 2700 °C) makes it useful for high temperature application. Silicon carbide does not melt at any known pressure. It is also highly inert chemically. SiC also has a very low coefficient of thermal expansion (4.0×10^{-6}/K) and experiences no phase transitions that would cause discontinuities in thermal expansion [23].

1.3.3 Electronic Band Structure of SiC and Energy Band Gap

There have been many experimental and theoretical studies on SiC polytypes [27]. For electronic structure studies, most of the calculations used Density Functional Theory which is a theoretical approach to simulate the behavior of many body systems to investigate the ground state of the system [28]. Figure 1.6 shows the electronic band structure of major polytypes of SiC, which is calculated using the orthogonalized linear combination of atomic orbital method [29]. This is a density functional theory based method that uses the local density approximation (LDA) for the exchange-correlation potential which is described in [30,31].

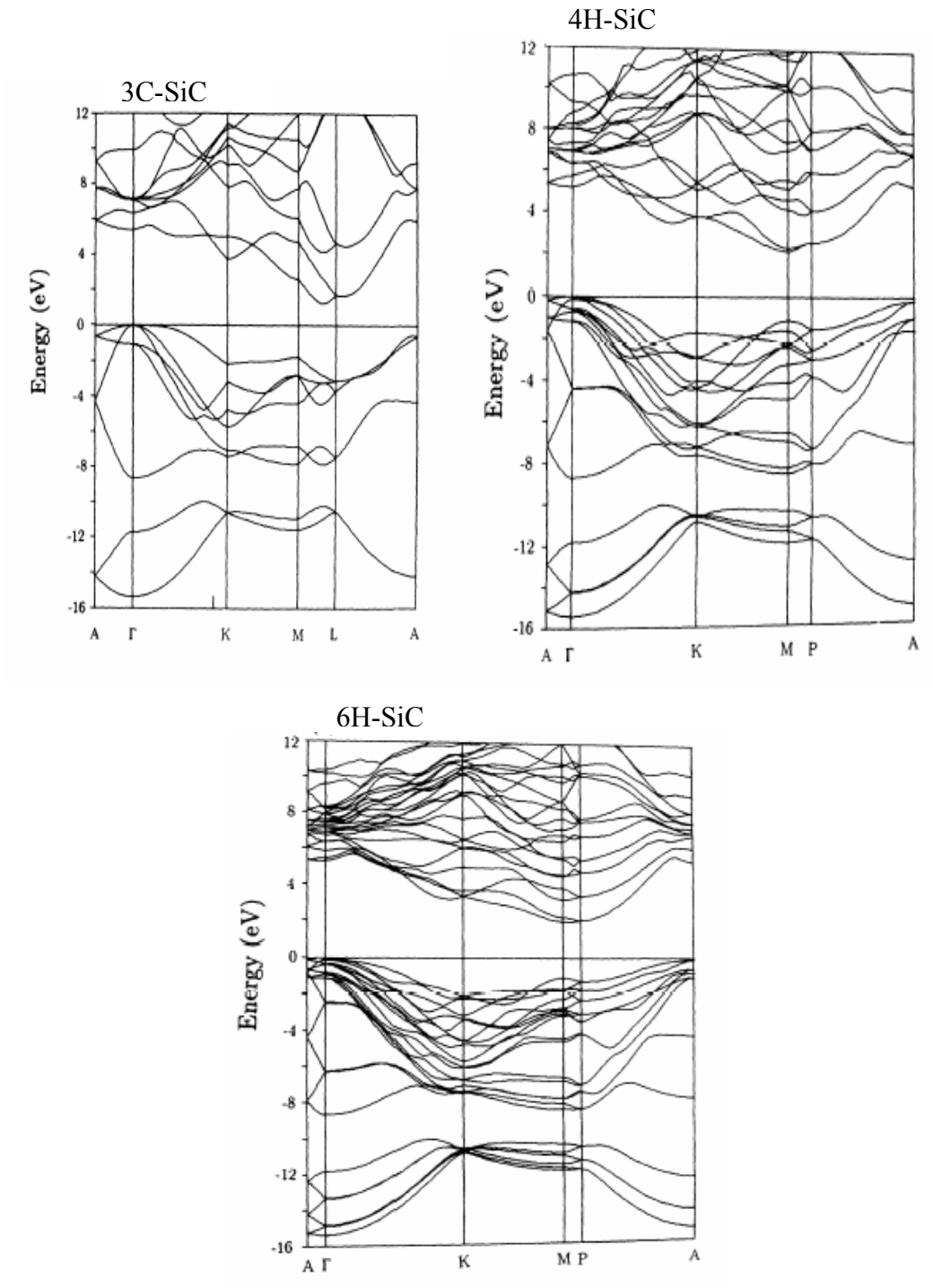

Figure 1.6. Electronic band structure of major polytypes of SiC [27]

As can be seen from Figure 1.6, the electronic band structure is getting more complicated as the crystal complexity increases. All polytypes of SiC can be considered as indirect band gap semiconductors. The magnitudes of band gaps

change significantly with the crystal structures of considered SiC. The energy of the conduction band (CB) minimum also varies from the cubic SiC to hexoganal SiC. The top of the valence band (VB) in each case is always at the Γ point and the bottoms of the CB are at different locations. CB minimum is at the X point for 3C-SiC, having the band gap 1.24 eV, while this is at the M point in 4H-SiC with the band gap 2.14 eV. In 6H-SiC, the CB minimum is not at M, but is slightly shifted towards L point. The calculated indirect LDA gap for 6H-SiC is 1.98 eV.

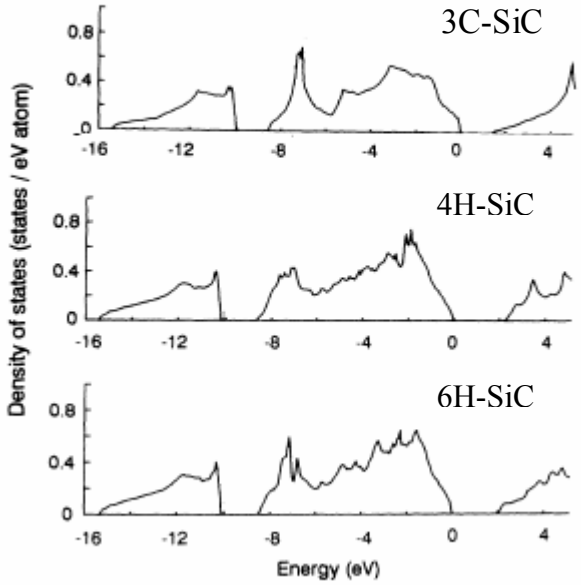

Figure 1.7 Total DOS of major SiC polytypes [27]

The calculated total density of states (DOS) are shown for the major polytypes of SiC in Figure 1.7. From 3C-SiC to 4H-SiC, the -2 eV peak increases, while the the -7 eV peak decreases. The forms of the DOS in the range -16 and -10 eV is considered to be similar for all polytypes of SiC. However, the forms of DOS located near the conduction band edges are changed [29,31]. This is the result of 3C-SiC phase with a cubic symmetry. All of the others have hexagonal symmetry. This difference is also more pronounced in the upper part of the VB.

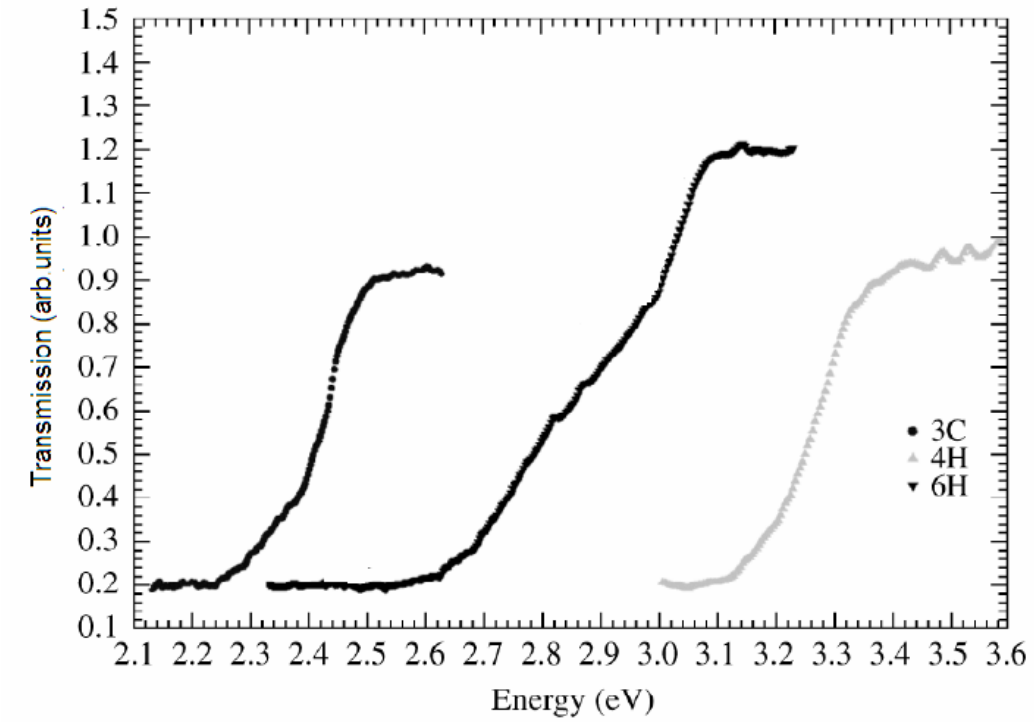

Figure 1.8. Transmission spectra of major polytypes of SiC [31]

Transmission spectra of the SiC polytypes are given in Figure 1.8. From the data shown in this figure, band gap of 3C-SiC was found to be ~2.4 eV, ~3.3 eV , and 3.03 eV for 3C-SiC, 4H-SiC, 6H-SiC respectively. This wide band gap of SiC polytypes make it suitable for solar cell application [32].

1.3.4 Chemical, Structural and Optical Properties of SiC

Raman spectroscopy is a powerful technique for characterization of Si-Si, C-C vibrational bonds in studied films. It is a powerful tool for the identification of the polytypes of SiC and measure the crystallinity [33]. By measuring Raman spectra in the range of 700-1000 cm^{-1}, information on the crystallinity of the SiC can be obtained. Furthermore, the information about the presence graphite formation can be obtained in the Raman spectra in the range of 1300-1600 cm^{-1} [34]. Figure 1.9 illustrates typical Raman spectra obtained for major polytypes of SiC [35]. In addition, Si nanocrystal formation can be detected by observing Raman signal in the range of 150-600 cm^{-1}. Table 1.2 summarizes different bands observed and their assignments in the Raman spectra of SiC [34].

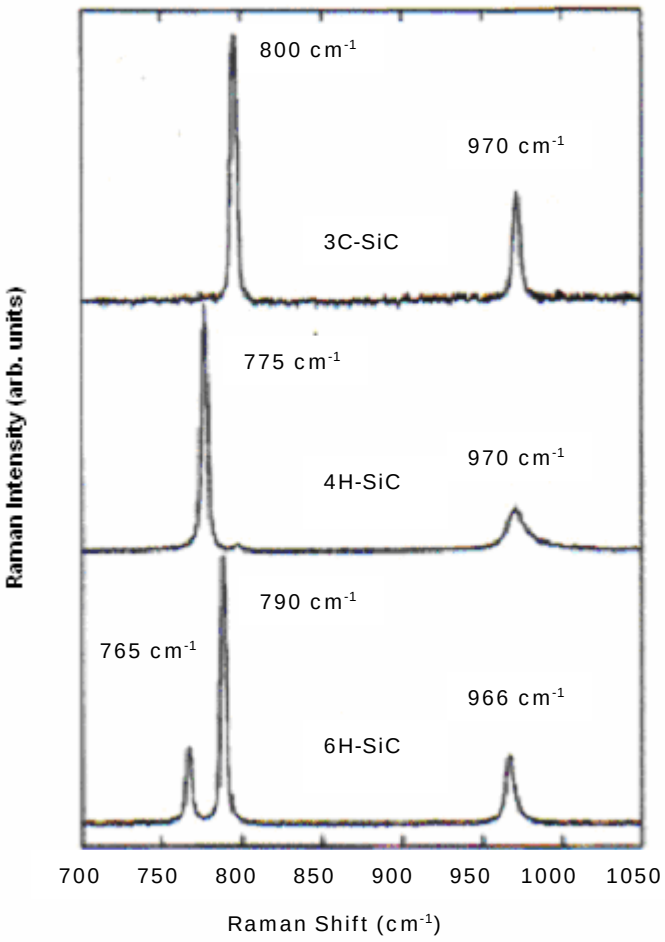

Figure 1.9. Typical Raman spectra for major polytypes of SiC [35]

Table 1.2 Positions (in cm^{-1}) and assignments of bands Si-Si, Si-C and C-C vibrations (crys. for crystalline structure, LA for longitudinal acoustic, TO for Transverse Optic, LO for Longitudinal Optic)

Si-Si vibrations		Si-C vibrations		C-C vibrations	
180-200	Crys. Si TA	580-600, 660	Disordered SiC	1080-1090	C sp^3
260	Crys. Si LA LO	766,789 797	Crys. SiC 1st order	1400-1420	C sp^2 D line
450-500	Amorph Si	767,870	Amorph SiC	1415-1420	Amorph sp^2/sp^3
521	Crys. Si 1st order	967,970	Crys. SiC 2nd order	1560-1600	C sp^2 G line
960	Crys. Si 2nd order	915-920, 935-940	Disordered SiC		

It is known that infrared spectroscopy and Raman spectroscopy are complementary techniques for identification of the vibrational states. Infrared absorption spectroscopy is essentially to extract the information about bonding states of the SiC molecules. Typically, infrared radiation can only be absorbed by bonds within a molecule, when its energy is exactly the same energy to excite vibration in the bond. Table 1.3 shows the generally accepted hydrogen vibrational and assigned peaks for Si:H and SiC:H films [34-36]. These materials form as a by product during the deposition process of PECVD for SiC.

Table 1.3 Hydrogen vibrational and assigned peaks for Si:H and SiC:H films

Vibrational Frequency (cm^{-1})	Attribution
2860-3000	CH,CH_2 and CH_3 stretching
2140	SiH_3 stretching
2070-2100	SiH_2 stretching / C-SiH stretching
2000	SiH stretching
1350-1400	Si-CH_3 degenerate Deformation / $SiCH_2$ bending
1250	Si-CH_3 symmetric bending
1000-1050	Si-CH_2, $SiCH_3$ rocking or wagging
890	SiH_2 scissors bending
845	SiH_2, $(SiH_2)_n$ wagging
780	Si-C stretching / Si-CH_3 rocking or wagging
630	Si-H bending / SiH_2 , SiH_3 rocking or wagging

Figure 1.10 shows the X-ray diffraction (XRD) pattern of SiC prepared by the sublimation method [37]. The peaks are mainly attributed to 3C-SiC with lattice parameter a = 4.3591 Å. There are two weak peak located at 34.2541^o and 36.0989^o which are coming from (101) and (103) plane of 6H-SiC with lattice parameters a=3.078 Å and c = 15.12 Å [37]. The numerical data were given in the Table 1.4 XRD pattern of 3C-SiC shown in Figure 1.10.

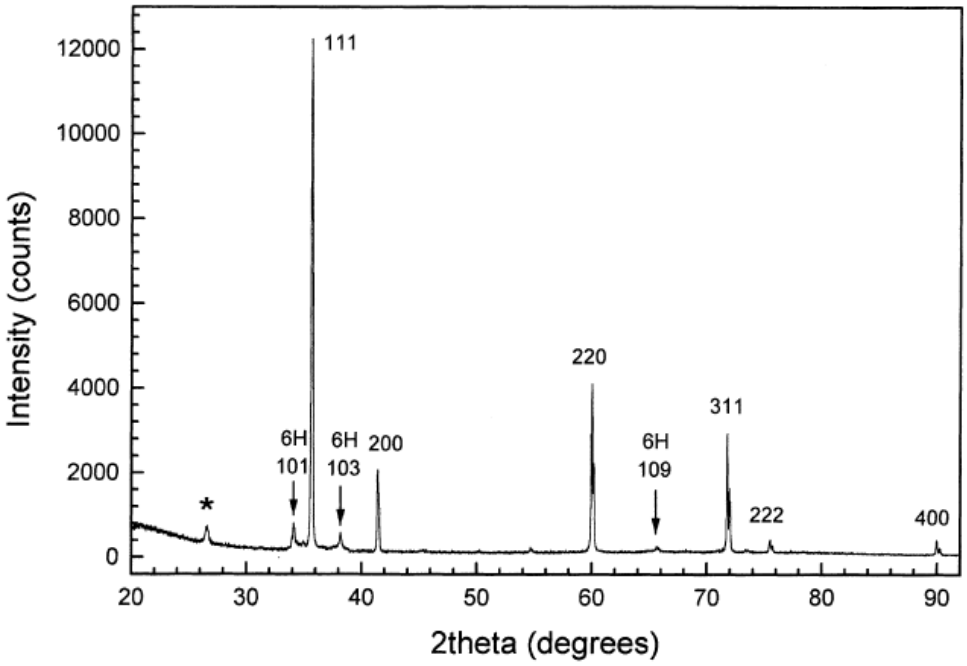

Figure 1.10. XRD pattern of SiC polytype [37]

Table 1.4 X-ray diffraction pattern of SiC observed in Figure 1.10

h k l	D	2θ	I_{ref}
111	2.517	35.645	100
200	2.1795	41.394	20
220	1.5412	59.976	35
311	1.3143	71.759	25
222	1.2584	75.490	5
400	1.0898	89.958	5

Figure 1.11 shows the X-ray photoelectron spectroscopy (XPS) spectra of Si 2*p* and C 1*s* XPS spectra of the SiC film prepared by magnetron sputtering. There are two peaks located at the energy of 99.1 and 101.7 eV for Si 2*p* XPS signal, which corresponds to Si-Si and SiC bond, respectively [37]. It is seen in Figure 1.11 that

there are also two peaks at the binding energy of 281.3 and 283.8 eV, which is associated with Si-C and C-C bond, respectively [37].

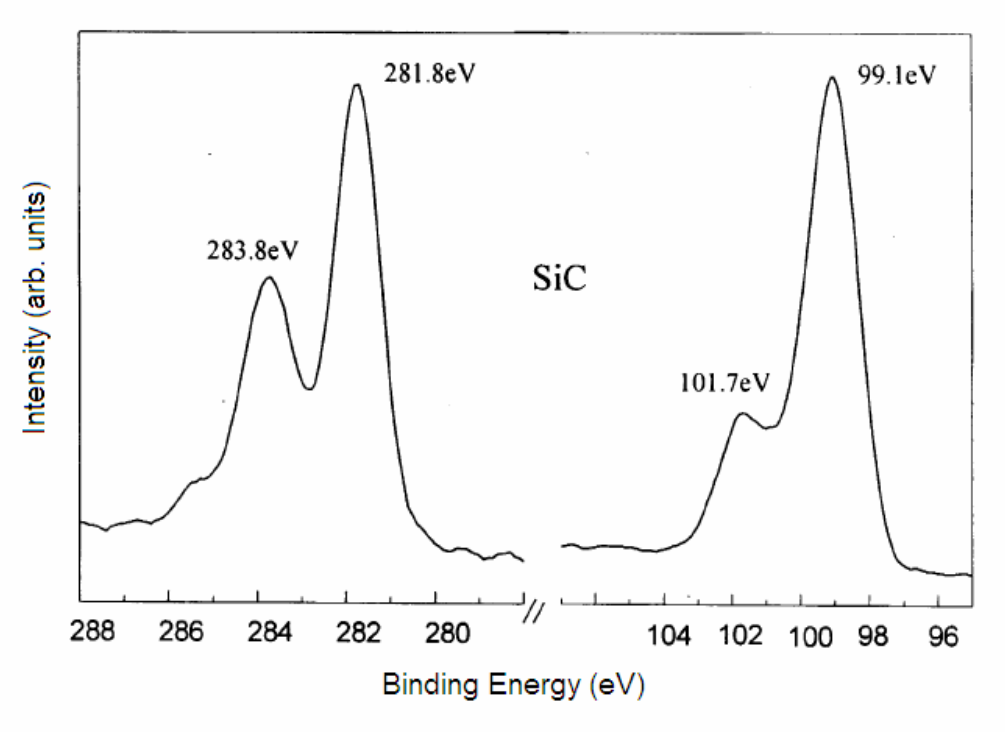

Figure 1.11. Si 2*p* and C1*s* XPS spectra of SiC [38]

1.4 FTIR as a Powerful Diagnostic Tool

Semiconductor nanocrystals in dielectrics have attracted most attention due to promising applications as summarized above [15,16]. Most of the researches have focused on size dependent optical and electrical behaviors of these nanostructures [39,40]. For the chemical and structural characterizations, various spectroscopic techniques such as FTIR spectroscopy, Raman spectroscopy, XRD, Transmission electron microscopy (TEM) have been utilized [17-19]. Among them, FTIR spectroscopy that deals with the absorption of the infrared light in vibrational states of the species is widely used for the characterization of semiconductor materials. Infrared absorption of unknown species basically depends on the net change in the dipole moment. Therefore, FTIR is very sensitive to the structural variations and chemical compositions of the unknown molecules [41,42]. In this

thesis, a new approach was applied to monitor the structural variations of SiO_2 matrix during the formation of Si nanocrystals by FTIR. An indirect method based on deconvolution of SiO_x band during the annealing was developed to show the nanocrystal formation in the oxide matrix. The shift in the peak position and the variation in the integrated area of SiO_x band are found to be well correlated with the change in the stoichiometry of the film and nanocrystal formation [43,44].

1.5 Overview of the Thesis

There are two main research topics in this thesis. In the first part, it is shown that FTIR is a useful diagnostic method to monitor the nanocrystal formation in the SiO_2 matrix. It is shown also that the stoichiometry of SiO_x can be monitored to understand the Si nanocrytal formation indirectly via FTIR.

In the second part of the study, the formation of Si nanocrystal in SiC as an alternative host matrix has extensively been investigated. Under certain conditions of co-sputtering and annealing, formation of Si nanocrystals in the SiC matrix is demonstrated.These two main parts of the thesis have been devided into 8 chapters. These chapters are briefly described below.

Chapter 2 provides a description of the experimental techniques used in the fabrication and characterization of the materials.

In Chapter 3 characterization of Si, Ge and Fe_2O_3 nanocrystals in SiO_2 by using FTIR is discussed. Fe_2O_3 nanocrystal system was added to this work in order to investigate the application of this new approach to a completely different material system. Deconvolution procedure was applied to observe the variation in the stoichiometry of the SiO_2 matrix. The shift in the peak position and the change in the integrated area of the main infrared signal were used to monitor the nanocrystal formation.

Chapter 4 deals with the fabrication and characterization of nanocrystalline SiC:H thin films that were deposited by plasma enhanced chemical vapor deposition (PECVD) process. Effect of the gas flow, hydrogen dilution, and post annealing

on the stoichiometry and crystallinity of the SiC:H thin film were investigated with FTIR spectroscopy, Raman measurement, XRD, and optical transmission techniques.

In Chapter 5, fabrication and characterization of Si nanocrytals in Si:H was demonstrated. Si:H/SiC:H sandwich and multilayer film were deposited by PECVD with the optimum parameters described in Chapter 4. The prepared films were characterized by FTIR spectroscopy, Raman measurement, XRD and TEM.

Chapter 6 presents synthesis of a-SiC thin films prepared by sputtering with different parameters.

In Chapter 7, the synthesis and characterization of Si nanocrystals in SiC matrix single films were discussed. The process parameters were varied to control the amount of the nanocrystals formed in the SiC matrix. FTIR spectroscopy and Raman measurement were applied to characterize the films. XPS depth profile studies were conducted to investigate the chemical structure of the film. The formation of Si nanocrystals in some samples was studied by grazing incidence XRD experiments. The size of the Si nanocrystals was estimated by Scherrer's formula. The fabrication of Si nanocrystals in multilayer SiC matrix with the aim of the producing the different band in the same samples is discussed. The characterization of the multilayer films was performed by TEM, FTIR spectroscopy, Raman measurement, SEM, and XPS.

Finally, in Chapter 8, some final words, conclusions and future directions are given.

CHAPTER 2

EXPERIMENTAL PROCEDURES FOR FABRICATION AND CHARACTERIZATION

2.1 Introduction

In this chapter, basic information of the fabrication and characterization method for studied samples is given. Magnetron sputtering and PECVD technique were used to deposit the films, followed by a post annealing process to enhance the film stoichiometry and to induce nanocrystal formation. Numerous diagnostic techniques were employed to monitor and analyze both film structure and nanocrystal formations. FTIR spectroscopy was applied to study the vibrational bonds in the films. Raman spectroscopy was used to detect the Si-Si bond vibrations to trace the presence of Si nanocrystals. XRD was employed in to see if there exist any crystal formation for SiC and Si nanocrystals. XPS revealed the atomic composition and chemical state of the films as a function of the depth from the surface. In this chapter, brief information about these techniques is given.

2.2 Magnetron Sputtering Technique

Various types of thin films such as carbides, nitrides, oxides can be deposited using physical vapor deposition (PVD) techniques under plasma conditions such as sputter deposition. Recently, PVD has been utilized at industrial level due to expanding applications of these materials on semiconductor-electronic industry.

2.2.1 Features of the Sputter Deposition

Sputtering is a PVD technique for thin film formation, which is realized by the bombardment of a target material with energetic ions, which are generated by an electron beam whose trajectory is determined by electromagnetic field created by an applied voltage and magnets. Their energy and momentum are transferred to target's surface atoms. These sputtered atoms condense on the substrate, which is effective way for thin film deposition [45,46]. Figure 2.1 shows a simple schematic setup of sputtering deposition system [47].

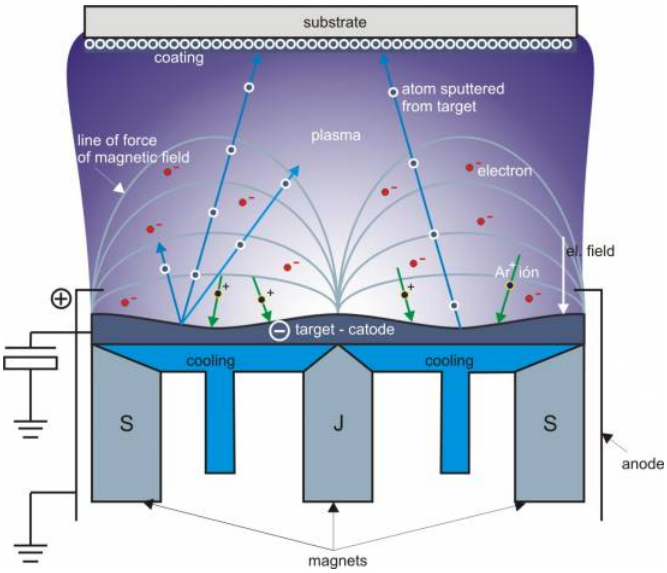

Figure 2.1. Schematic setup of sputtering deposition system [47]. The electrodes on the left side creates high voltage to accelerate the ions towards the target

In the ideal case, the thin film should be deposited in the vacuum (base pressure < 10^{-6} Torr) and in a low-pressure gas ambient (<$5x10^{-3}$ Torr) to increase the sputtering yield of the process and to obtain the best quality in the film. The ratio of the number of ejected target atom to the number of incident sputtering ion is known sputtering yield [48]. The sputtering yield depends on:

- Target material
- Crystal structure of the target
- Sputtering gas
- The oblique angle of the projectile

The kinetic energy of sputtered atoms changes with the bombarding ions, its energy, and the target material. The heavier ions in the sputtering gas resulted in the larger energy transfer to the sputtered atoms. By increasing the energy, sputtering yield increases initially, on the other hand sputtering yield decreases at very high energies due to resputtering from the deposited substrate or implantation of bombarding ions on the substrate surface. Further information on the sputtering technique and the system, we have used in this study can be found in M. Sc. Thesis by Alagöz [48]. Figure 2.2 shows the sputtering rate with respect to Ar gas flow and magnetron power for a SiC target in our system.

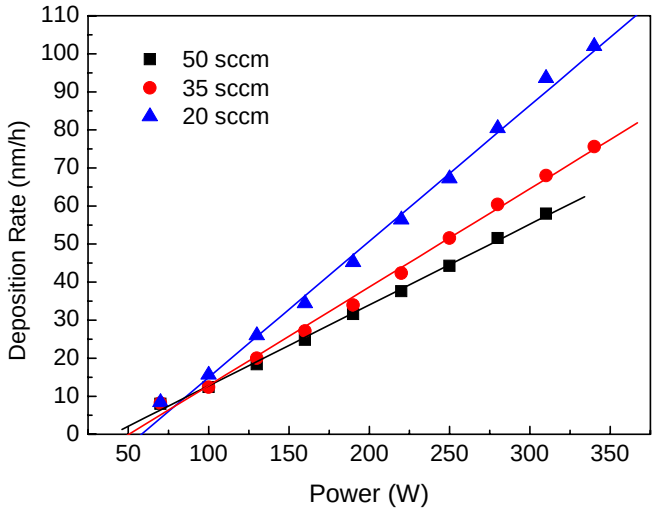

Figure 2.2. The sputtering rate with respect to Ar gas flow and magnetron power for SiC target

2.2.2 RF and DC Sputtering

Using the radio frequency (RF) sputtering, the deposition of insulating materials is possible. The substrates are placed in a low-pressure chamber between two electrodes. When the RF power is applied to the insulating target, self-bias potential is generated on the surface of the target due to the charging, ions are accelerated by this potential toward the target, and the target atoms are sputtered. The most commonly used frequency is 13.56 MHz. When the direct current (DC) power is applied to the target, the electrons that are ejected from the target are

circulated above the surface due to the magnetic field and these circulated electrons generate highly dense plasma above the target surface. The sputter rate in the DC sputter process is highly relative to the RF sputter process; however, the uniformity of the sputtered film is not good with respect to RF sputter process. In order to provide the uniformity of the film, the position of the substrate and magnetrons should be well aligned. Figure 2.3 shows our sputter deposition system Nano D100, produced by Vaksis [49].

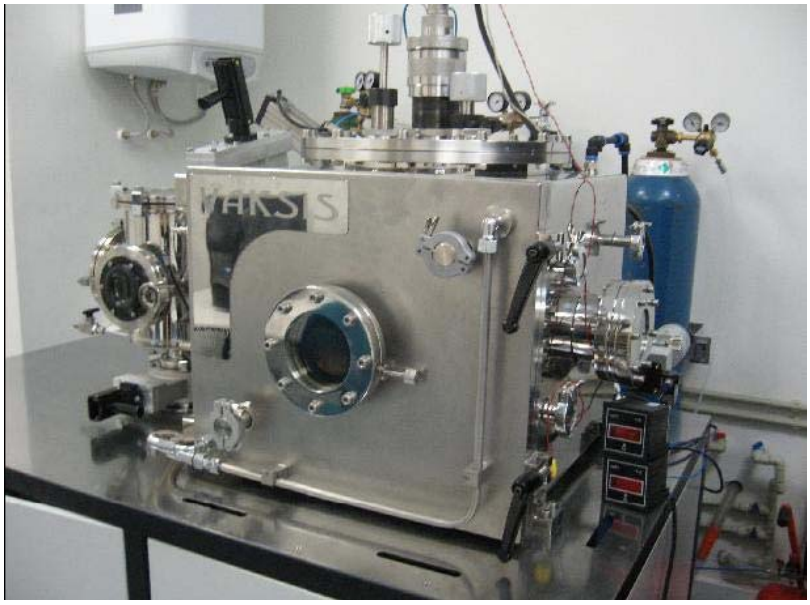

Figure 2.3. The sputter deposition system in semiconductor device and characterization laboratory

2.3 Plasma Enhanced Chemical Vapor Deposition

PECVD is an important deposition technique for the fabrication of Very Large Scale Integration and thin film transistors. It has two advantages compared with the conventional CVD method: low process temperature and flexible film properties.

2.3.1 Features of PECVD

PECVD is also known as glow discharge chemical vapor deposition [50]. Glow discharge is generated by means of a RF or DC voltage between two conductive

electrodes, which are placed in a vacuum chamber. PECVD is used to deposit thin films from the gas phase reactions in the plasma to surface reactions on a substrate at low temperature. Actually, the reaction mechanism in PECVD is not well understood, due to complexity of the reaction system. A significant percentage of gas molecules are ionized or dissociated in the plasma via electron impact. These exited molecules created in the gas state condense on the substrate by diffusion during the deposition process [51]. The pressure range typically changes from a few milliTorr to a few Torr during the processing plasma. The factors that affect the deposition rate in PECVD are,

- The reaction gas type
- The flow rate of the reaction gas
- The power of the RF source
- The substrate temperature
- The background pressure

When the RF power is constant, the deposition rate of the film is limited by the flow rate of the reaction gas. When the gas flow is high, the deposition rate depends upon the RF power. The deposition rate also changes with the substrate temperature [50,51].

2.3.2 System Configuration

Generally, PECVD equipment is composed of the supply system of the reaction gas, reactor, and gas flow-rate control unit. Many types of discharge mechanisms, such as hollow cathode discharge, microwave discharge, a high-pressure discharge a high-frequency discharge have been used in PECVD systems. Among them, a high-frequency discharge with parallel plate electrodes has been commonly used in PECVD system, as shown in Figure 2.4 [52].

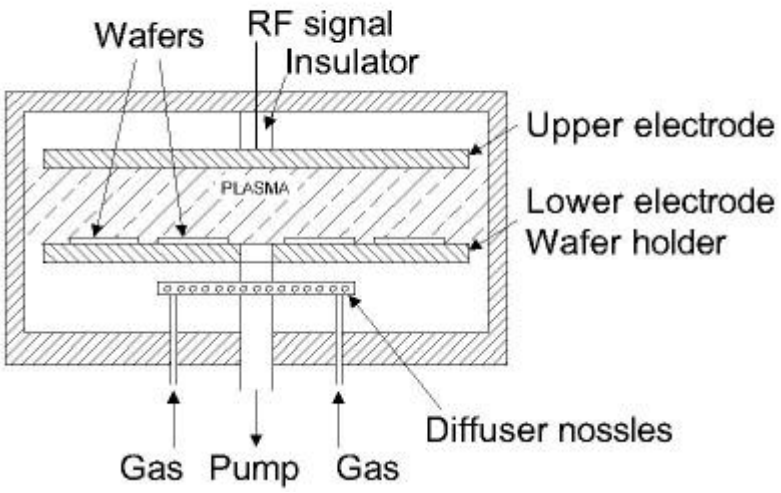

Figure 2.4 Typical parallel plate reactor [52]

In this type reactor, RF signal can be applied between an electrode and the conductive walls of a reactor chamber, or between two cylindrical coaxial conductive electrodes facing one another in order to deposit insulating films. Reaction gases are entered through the small holes located beneath the substrate holder. Gas is passed over the substrates and is evacuated by the turbo pump [51]. Figure 2.5 shows the PECVD system at Department of Photovoltaic, Institute of Energy Research, Research Center Jülich, Germany.

Various precursor gases can be used depending on thermal stability of substrate, for example, Si, SiO_2 and SiC film can be deposited with the following reactions [51],

$$SiH_4 \rightarrow Si + 2\ H_2 \quad (2.1)$$

$$SiH_4 + O_2 \rightarrow SiO_2 + 2\ H_2 \quad (2.2)$$

$$SiH_4 + CH_4 \rightarrow SiC + 4\ H_2 \quad (2.3)$$

In first two equations, silicon film can be deposited using silane, and silicon dioxide can be deposited from silane and oxygen typically at pressures from a few hundred milliTorr to a few Torr. Plasma-deposited silicon carbide formed from

silane and methane is widely used. It is important to note that it is not possible to deposit pure carbide in this process. Plasma deposited silicon carbide always contain a large amount of hydrogen, which can be bonded to silicon (Si-H) or carbon (Si-CH), this hydrogen has an important influence on UV absorption, stability, mechanical stress, and electrical conductivity of the film.

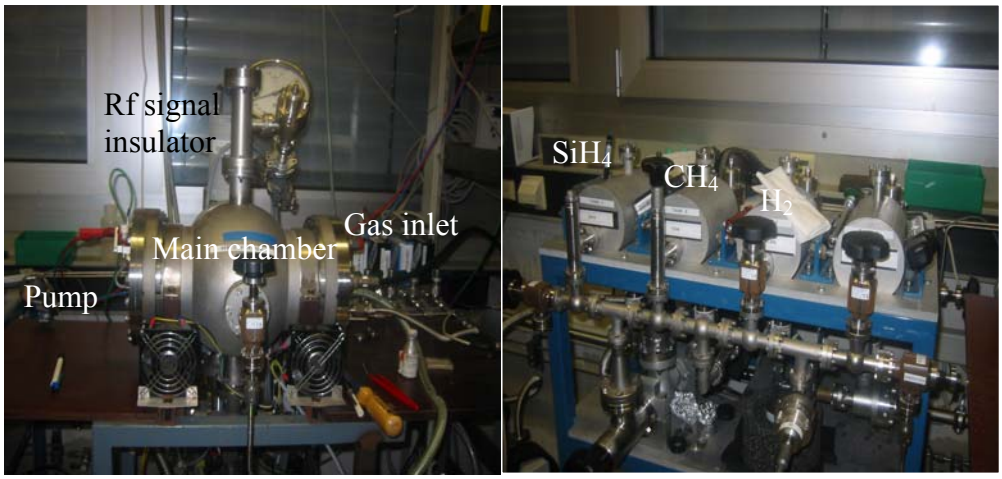

Figure 2.5. Main chamber and gas controller unit of the PECVD system at the Department of Photovoltaic, Institute of Energy Research, Research Center Jülich, Germany

2.4 Fourier Transform Infrared Spectroscopy

FTIR is a powerful and non-destructive tool to extract information about the vibrational states in an unknown molecule. Because the IR spectrum of each molecule is unique, it can serve as fingerprint to identify the unknown molecule [53].

Schematic diagram of typical FTIR setup is shown in Figure 2.6 [54]. In order to produce mid-infrared light, globar source is used. Tungsten filaments and mercury arc lamps are used to produce the light in near and far infrared region, respectively. A laser (632.8 nm) is used for alignment of the optical path. The main difference of FTIR from the dispersive systems is that FTIR setup is

typically based on Michelson interferometer. The Michelson interferometer consists of two mirrors, one of them is the stationary mirror, the other mirror moves with constant velocity. The beam splitter between the mirrors splits the incoming beam into two parts, which are recombined after path difference. The path difference can be converted to frequency by Fourier transform method. The infrared beam passing through the sample reaches the Deuterium Tryglycine Sulphate detector. A plot of intensity versus frequency is a FTIR spectrum.

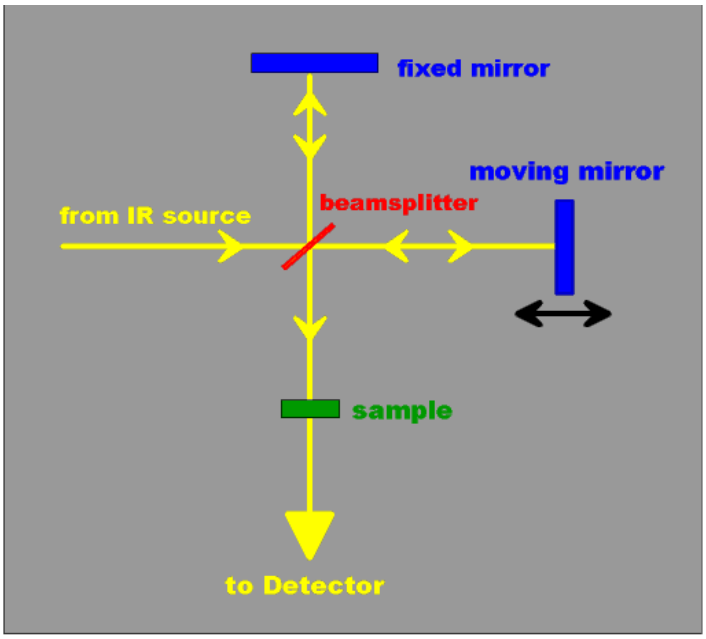

Figure 2.6. Schematic diagram of typical FTIR setup [54]

Depending on the elements and the type of bonds, molecular bonds vibrate at various frequencies. According to laws of quantum mechanics, these frequencies correspond to the ground state (lowest frequency) and several excited states (higher frequencies) of the vibrational spectrum. An external light beam is typically used to excite a molecular vibration. For any given transition between two states, the light energy must exactly equal to the difference in the energy between the two states (usually ground state (E_0) and the first excited state (E_1)).

Molecular vibrations can be classified the two main categories as a stretching and bending vibrations. Bond length of the molecule changes in the stretching vibration. In bending vibrations, the angle between two bonds of the molecule varies during the vibration. The molecules can also vibrate in rocking, twisting, scissoring, and wagging modes, which are four types of bending vibration [54].

The absorption of light depends on the properties of the material through which the light is traveling, as states by Lambert [55]. The Beer-Lambert law is the linear relationship between absorbance and concentration of an absorber of electromagnetic radiation. The general Beer-Lambert law is usually written as;

$$A = \log \frac{I}{I_0} = \alpha \times b \times c \tag{2.4}$$

where A is the measured absorbance, I_0 is the intensity of the incident light, I is the intensity of the transmitted light, α is a absorption coefficient, b is the path length (thickness), and c is the concentration.

As the SiO_2 thin film on Si substrate is the cornerstone of the microelectronic industry, the characterization of Si-SiO_x interface and the structure of SiO_x film have always attracted much attention [56-58]. An empirical relation was developed to find the x value for SiO_x deposited by PECVD by Tsu et al. [59].

$$\nu_{Si-O} = 965 + 50x \tag{2.5}$$

where ν is the peak position of the Si-O-Si asymmetric stretching band for SiO. When the x is equal to 2, the peak position of this band reaches 1065 cm^{-1}.

Dehan et al. suggested another relation, in which is stated that the SiO_x film is a combination of a-Si and SiO_2 [60]. This relation is given in Equation 2.6.

$$n(\gamma) = 4 - 2.53\gamma + 0.63\gamma^2 \tag{2.6}$$

where n is the refractive index and γ is the concentration ratio of the oxygen to silicon.

The concentration of the Si-O bonds can be estimated using FTIR given as follows,

$$c_{(Si-O)} = A\int \frac{\alpha(\nu)}{\nu} d\nu \tag{2.7}$$

where α is the absorption coefficient, ν is the peak position and A is the calibration constant that can be taken as 1.5×10^{19} cm^{-2} [61].

In addition to these empirical calculations using FTIR spectroscopy, deconvolution process that provides us a qualitative result will be discussed in detail in the chapter 3.

In this dissertation, FTIR measurements were performed with a 4 cm^{-1} resolution between the wave number 400-4000 cm^{-1} by using a Bruker Ekinox 55 spectrometer. An unprocessed Si substrate was used to obtain the back round signal, which was subtracted from the FTIR signal of the studied sample.

2.5 Raman Spectroscopy

Raman spectroscopy is a nondestructive vibrational spectroscopic technique that can detect high-frequency phonons and electronic excitations in interested species and measure the crystallinity of the materials [62]. The physical principle of the technique is that incident light interacts with phonons or other excitations in the system, resulting in the energy of the incident photons being shifted up or down. The shift in energy is equal to the vibration of the scattering molecule, which is a fingerprint for interested molecules [63]. A plot of intensity versus energy difference between the incident and scattered photons is a Raman spectrum. The Raman shift can be estimated by the equation 2.8 [63].

$$\frac{1}{\lambda} = \frac{1}{\lambda_{incident}} - \frac{1}{\lambda_{scattered}} \tag{2.8}$$

where $\frac{1}{\lambda_{incident}}$ and $\frac{1}{\lambda_{scattered}}$ are wave numbers (in cm $^{-1}$) of the incoming and the scattered photon, respectively.

If there is no energy difference between the incoming and scattered photon, this is called Rayleigh scattering. There are two types of Raman scattering, Stokes scattering and anti-Stokes scattering. An energy band diagram is seen in Figure 2.7 [64].

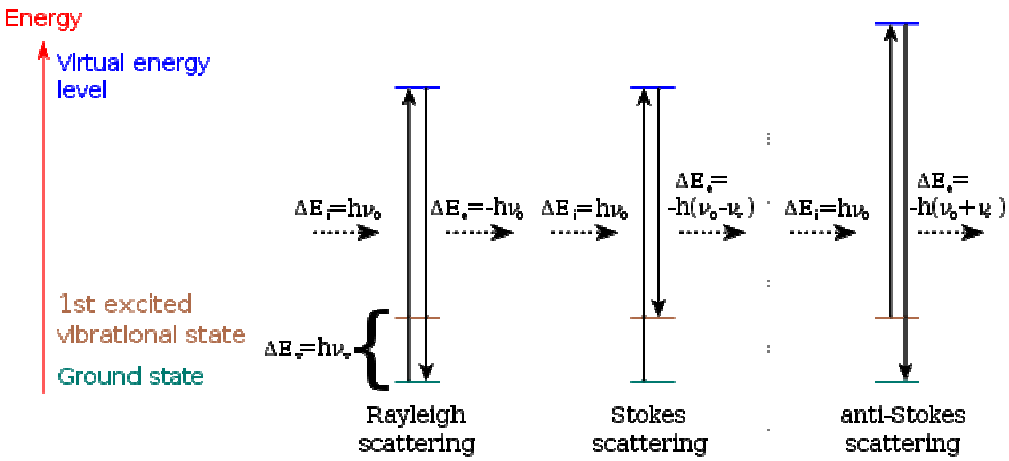

Figure 2.7. The energy level diagram for Raman scattering [64]

The incoming photon excites the studied molecule into a virtual state. When the molecule absorbs some energy, the resulting photon of lower energy generates a Stokes line on the red side of the incident spectrum. When the molecule loses the energy, incoming photon shifts to the blue side of the spectrum, so it generates anti-Stokes line.

The peak position and peak shape of the measured Raman signal can provide us with the information about the properties of the nanocrystals. The peak position and the shape of the Stokes line shifts exhibit different properties for Si with the grain sizes below 100 Å [65]. Thus, estimation of the size of the nanocrystals and

that of the phase changes is possible by Raman spectroscopy [66]. Furthermore, the frequency of the Raman signal shifts also by the stress in the film [67]. Therefore, the stress on the nanocrystals can be estimated [68].

In this thesis, back scattering Raman spectroscopy measurements were carried out by with a Jobin Yvon Horiba HR800 micro-Raman system situated in the Department of Chemistry at METU. A He-Ne laser with 632.8 nm, a single monocromotor and peltier cooled charge coupled device camera with a resolution of 1 cm^{-1} were used to detect Raman shift. All measurements were performed at room temperature.

2.6 X-Ray Diffraction

X-Ray Diffraction (XRD) is a non-destructive analytical technique, and it is used for determining of the crystallographic structure, crystallite size, and preferred orientation. The principle of the technique is based on the observation of the scattered of X-ray beam striking a sample as a function of scattered angle, polarization and energy [69].

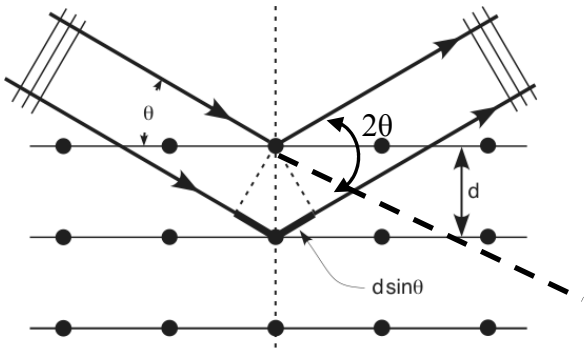

Figure 2.8. The schematic diagram of the basic principle of the XRD experiment [70]

Figure 2.8 depicts the basic principle of the XRD experiment [70]. Here 2θ is the diffraction angle between the incident and diffracted X-ray beam. Bragg's law of diffraction states the relation between the angle and plane spacing, d [71],

$$n\lambda = 2d_{hkl}\sin\theta \tag{2.9}$$

where n is the integer representing the order of diffraction in the formula and λ is the wavelength of the X-ray beam (the X-ray source is Cu K_α (1.54 Å) in our system). Using the Equation 2.9, the crystal plane spacing can be found. The lattice constant of the material can be determined from the equation,

$$d_{hkl} = \frac{a_0}{\sqrt{h^2 + k^2 + l^2}} \tag{2.10}$$

in which h ,k, l are the Miller indices.

Figure 2.9 shows the schematics of the Bragg-Brentano diffractometer [71]. In the diffraction measurement, a sample is placed on the goniometer, and gradually rotated while being bombarded with X-rays. Reflected X-rays produce a diffraction pattern with the information about the planes of an infinite size crystal.

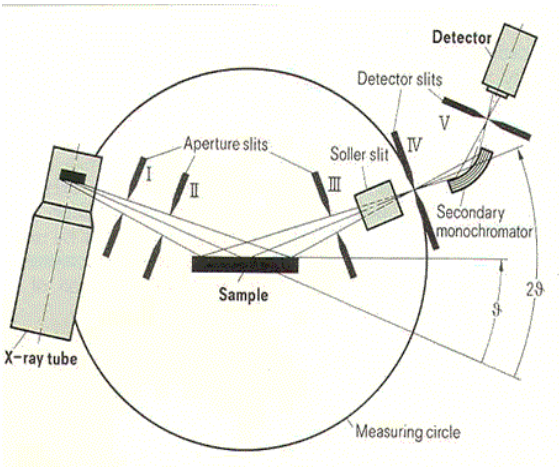

Figure 2.9 Schematic diagram of the Bragg-Brentano diffractometer [71]

For the finite size crystal, the number of Bragg planes becomes less. An influence of the finite crystallite sizes is seen as broadening of the diffraction peak at the Bragg angle. If the size of the crystal is less than 200 nm, X-ray diffraction is explained by the Scherrer equation [72].

$$D = \frac{\kappa\lambda}{\beta \cos\theta} \tag{2.11}$$

Scherrer's equation is used for the calculation of crystal sizes [72,73]. In this equation, λ is the wavelength of the incoming X-ray beam, β is the full width half maxima of the diffraction peak, κ is the Scherrer's constant and D is the size of the crystal grain. κ value is dependent on the size and shape of the nanocrystal if the size is less than 3 nm.

In this study, XRD measurements were performed with standard X-Ray diffractometer (Rigaku Miniflex) with the excitation source Cu Kα (0.154 nm) for the studied samples. Grazing incidence XRD (GIXRD) measurements were done by Rigaku Ultimate-IV grazing angle XRD system located at Central Laboratory METU with Cu Kα X-Ray source.

2.7 X-Ray Photoelectron Spectroscopy

X-Ray Photoelectron Spectroscopy (XPS) is a surface analytical technique, which is used to determine the elemental composition, chemical state of the elements within the measured material [74]. The basic physical principle of XPS is based on the ejection of electron from the core levels by X-ray photons of energy, $h\upsilon$. The emitted photoelectrons are analyzed by electron spectrometer and then the obtained data depicted as a spectra of intensity versus binding energy of the electron [75]. XPS analysis must be carried out in ultra high vacuum (UHV) condition to increase the mean free path of the ejected electrons. Dual beam X-ray source can use either Al or Mg target material in order to generate X-ray beam with the following energies 1486.6 eV or 1253 eV, respectively.

The electron that is ejected from the core shell of an atom has a unique binding energy, which seems like a fingerprint. Thus, almost all atoms except for hydrogen and helium can be identified via measuring the binding energy of its core electron. The binding energy of the core electron can be found by using the equation 2.12 [76].

$$E_K = E_{ph} - E_B - \Phi \qquad (2.12)$$

where, Φ is the work function, E_{ph} is the photon energy of X-ray source, E_K is the kinetic energy of the detected photoelectron. Since E_{ph} and Φ, are known quantities, E_B, the binding energy can be calculated from this equation by measuring the kinetic energy of the emitted photoelectron. When an incident X-ray beam strikes the material surface, the core electron of an atom absorbs the energy of the X-ray photon completely. If the photon energy, E_{ph}, is large enough ($E_{ph}>E_B$), the core electron will then leave the atom and reach the vacuum level. The process of photoemission is shown schematically in Figure 2.10 [76].

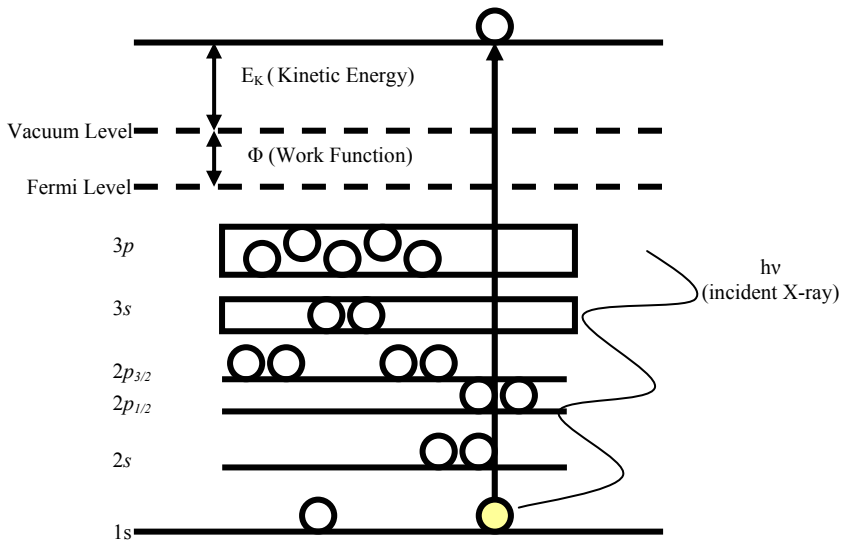

Figure 2.10. The schematic diagram of the photoemission process of an atom in XPS

XPS is not only used to identify the elements but also quantify the chemical composition because the number of photoelectron of an element depends on the atomic concentration of that element in the sample [68]. After the background subtraction, the peak area can be used (with appropriate sensitivity factors) to determine the chemical composition of the materials. The most commonly used background subtraction techniques are developed by Shirley [77] and Tougaard [78].

Furthermore, XPS is also used for depth profiling of the element and determining of its binding state. The depth profiling is a destructive method due to sputtering with Ar ions accelerated towards the sample using an ion gun. Atomic mixing, knock on implantation, bond breaking, charging and preferential sputtering might occur during this process. Ions with high mass and low energy should be used to dispose of the undesired effects during depth profiling [79].

Moreover, XPS is also useful to obtain the information about the chemical environment of the element because the binding energy of the core electron is very sensitive to the chemical environment of the element. If the same atom is bonded to different chemical specimen, it causes variations in the binding energy of its core electron. This may result in an observable shift in the corresponded XPS peak [76].

XPS analysis in this thesis was performed by using a SPECS EA 200 XPS system at Central Laboratory of METU. In this system, a Al Kα line is used for photoelectron generation. Ar^+ ions (2000 eV) are used to sputter the surface of the sample during the depth profiling.

CHAPTER 3

CHARACTERIZATION OF NANOCRYSTAL BY FTIR

3.1 Introduction

Semiconductor nanocrystals embedded in dielectrics are expected to play an important role in the development of next generation photonic and microelectronic devices in the near future [38]. Recently, there have been extensive studies on size dependent light emission characteristics and charge storage capabilities of these nanostructures [39]. Fabrication of light emitting devices tunable with the nanocrystal size, and fabrication of non-volatile flash memory cells have been the main motivation in these studies.

Si and Ge nanocrystals have attracted much attention because of the compatibility with the existing Si technology. Optical and electrical behavior of nanocrystals of this type has already been investigated extensively [40,80]. However, it is still a challenging task to form well-controlled, uniform and reproducible nanostructures with desired electrical and optical properties due to the difficulties in the fabrication, manipulation, and characterization of materials at the atomic scale. Different approaches and measurements along with comparative studies are needed for better understanding and controlling the nanocrystal formation [41].

The aim of this work was to study and understand the structural and chemical variations in the hosting SiO_2 matrix before, during and after the nanocrystal formation by using ion implantation and sputtering followed by a high temperature treatment. It is well known that the electronic vibrational states of

SiO_2 are strongly dependent on its oxidation state, that is, stoichiometry of the film [42,81]. Thus, addition of any excess elements to the matrix to form nanocrystals (Si, Ge) results in modification of the vibrational spectra of the matrix. As this modification is related to nanocrystal inclusion, a study of the vibrational states of the matrix should provide information not only on the structure and chemistry of the matrix, but also on the kinetics of the nanocrystal formation [43]. In a study reported by our group, it was shown that a FTIR provides complementary information on the nanocrystal formation in SiO_2 matrix [44]. In this chapter, we extend and elaborate this approach with a more detailed study including the analysis of the samples fabricated by sputtering in addition to the previous data on ion implanted samples.

Formation of Ge and Si nanocrystals in the samples has been studied by several diagnostic techniques including TEM and Raman spectroscopy methods as a function of annealing temperature [17-19]. The photoluminescence band at 700-850 nm which is commonly attributed to the Si nanocrystal was previously reported for the implanted samples [82,83]. Moreover, FTIR spectroscopy was partly reported for the samples implanted with Si and Ge to show the evolution of the matrix with the formation of the nanocrystals [43,44].

In this chapter, LO and TO vibrational modes of nanocrystal/dielectric system are monitored and analyzed to study the structural evolution of the matrix material at oblique angles. FTIR signals of the SiO_x matrix containing Ge and Si nanostructures prepared by ion implantation and sputtering are compared. The evolution of the matrix during the annealing process is monitored and correlated with the formation of the nanocrystals. We try to apply the same procedures other nanocrystal/dielectric composite system. In the last section of this chapter, we presented and discussed the structural variations of the silica matrix and formation of Fe_2O_3 nanocrystal during the calcinations process. The aim of including Fe_2O_3 nanocrystals was to understand whether we can apply the same approach to another composite system. We have seen that FTIR technique can be used for Fe_2O_3 nanocrystals embedded in silica matrix.

3.2 Experimental Procedure

The samples containing excess Si (or Ge) ions were prepared by using ion implantation, and magnetron co-sputtering. Before the fabrication of the samples by both techniques, the substrates were subjected to a standard Si wafer cleaning procedure. ^{74}Ge or ^{28}Si ions were implanted into 500 nm thick SiO_2 films grown thermally on Si substrate. The implantation dose of Si and Ge ions was $1.5x10^{17}$ ions/cm^2, while the implantation energy was kept constant at 100 keV. In the case of samples prepared by co-sputtering, Si (or Ge) (99.999 % pure) and SiO_2 (99.995 % pure) targets were sputtered on Si substrate at room temperature in Argon ambient using Vaksis nano-D 100 system. RF power (350 Watt) were applied to SiO_2 target, and DC power were applied to Si (or Ge) targets. The base pressure of the chamber before the deposition was $1x10^{-6}$ Torr. Argon gas pressure was fixed at $3x10^{-3}$ Torr during the deposition. The samples were rotated during the deposition and a high degree of uniformity was confirmed by thickness measurements of different locations of the sample surface. The implanted Si ions have a Gaussian distribution whose peak position is found to be at 140 nm from the surface by the Stopping and Range of Ions in Matter program. The samples were cut into small pieces, and annealed at different temperatures in quartz furnace. The details of the sample preparation conditions were given in Table 3.1, for clarity.

Table 3.1 Preparation condition of the samples

Technique	Ion Implantation		Magnetron Sputtering	
Element	^{28}Si	^{74}Ge	^{28}Si	^{74}Ge
Dose (ions/cm^2)	$1.5x10^{17}$	$1.5x10^{17}$		
DC Power (Watt)			70	70
Annealing Temperature (^oC)	800-1200	800-1000	600-1100	600-1000
Annealing Time (h)	2	1	1	0.5
Annealing Atmosphere	N_2	N_2	N_2	Vacuum

FTIR spectroscopy was used in absorbance mode to obtain the information about the vibrational states of the SiO_2 at an angle of incidence of 40^o. The samples were measured under the same experimental conditions for comparison. The samples were also examined using an analytical JEOL 2000 FX TEM system operating at 200 kV.

The FTIR measurements were performed with a resolution of 3-4 cm^{-1}. This corresponds to negligable amount of uncertainty in the wavenumber values we used. For the absorbance signals we studied, the intensity is usually very strong as we looked at relatively thick samples. We tried to figure out the amount of uncertainty in the absorbance data by repeated measurements of a typical sample used in this study. From the 10 repeated measurements, we found that the statistical variation in the absorbance data is less than %1. We used a peak fitting procedure for the deconvolution of the peaks with different origin. Assuming that the number of peaks and the reference point (peak position of SiO_2) we used are correctly determined, the fitting procedure that we applied is almost exact. The uncertainty in the deconvoluted peak, which is given by the fit program, is usually less than 1%. The overall uncertainty in the data generated from FTIR measurements is then small enough to neglect. For this reason they are not shown in the graphical representation throughout this thesis.

3.3 Results and Discussion

3.3.1 FTIR spectroscopy of SiO_2 matrix with excess Si and Ge before annealing

Thermally grown SiO_2 sample was first studied as a reference sample. Three main well-known bands were observed at around 459 cm^{-1} (TO_1), 815 cm^{-1} (TO_2), 1080 cm^{-1} (TO_3) corresponding to the rocking, bending and asymmetric stretching (AS) modes of Si-O-Si, respectively [42,83]. In addition to these peaks, vibrational modes at 1254 (LO_3), 1161 (LO_4) and 1209 (TO_4) cm^{-1} were recorded by using the oblique incidence of the light in Figure 3.1 [43,84]. The oblique angle, α, between the normal of the sample surface and the incident beam was set up to make these additional peaks more observable [85,86]. The polarization of the light is

commonly defined as s or p polarized when the electric field of the incident light is parallel or perpendicular to the plane of the sample surface, respectively. When the oblique angle is zero (α=0), the sample can interact with s polarized light only; on the other hand, when the oblique angle is greater than zero ($\alpha \neq 0$), the sample interacts both s and p polarized light [85]. In the latter case, LO peaks become more visible in the spectrum due to the direction of the incident beam [40,86]. We performed angle dependence measurement and found that an angle of incidence of 40^o gives the best signal strength and resolution for LO peaks. The deconvolution of the FTIR spectrum of the AS band of thermally grown SiO_2 measured at an oblique angle of 40^o is shown in Figure 3.1.

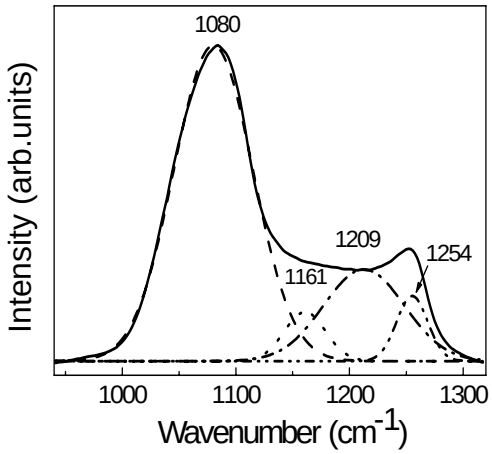

Figure 3.1. The deconvolution of Si-O-Si AS mode for thermally grown 500 nm SiO_2 (TO3-LO3 1080-1254 cm^{-1}; TO4-LO4 1209-1161 cm^{-1})

3.3.2 Evolution of the SiO_2 matrix during the annealing of the ion implanted samples

Figure 3.2 (a and b) show the variation of the FTIR spectra with annealing temperature for Ge and Si implanted SiO_2 respectively. Cross sectional TEM view of the samples are shown in Figure 3.2 (c and d) for Si and Ge nanocrystals, respectively. These images show that Si nanocrystals with a mean size of 3.5 nm and Ge nanocrystals with sizes less than 10 nm are formed after the annealing

process at given temperatures. Nanocrystal size varies with atomic concentration of species, annealing time and duration. It was previously reported Raman spectroscopy results showing formation of Ge nanocrystals in identically processed samples [17-19]. It is known that AS vibration of SiO_2 located at ~1081 cm^{-1} in the IR spectrum is very sensitive to structural variation of silicon dioxide matrix [41,81,85]. The intensity, peak position and the form of this absorption band are dependent on the stoichiometry of the silicon dioxide matrix [41].

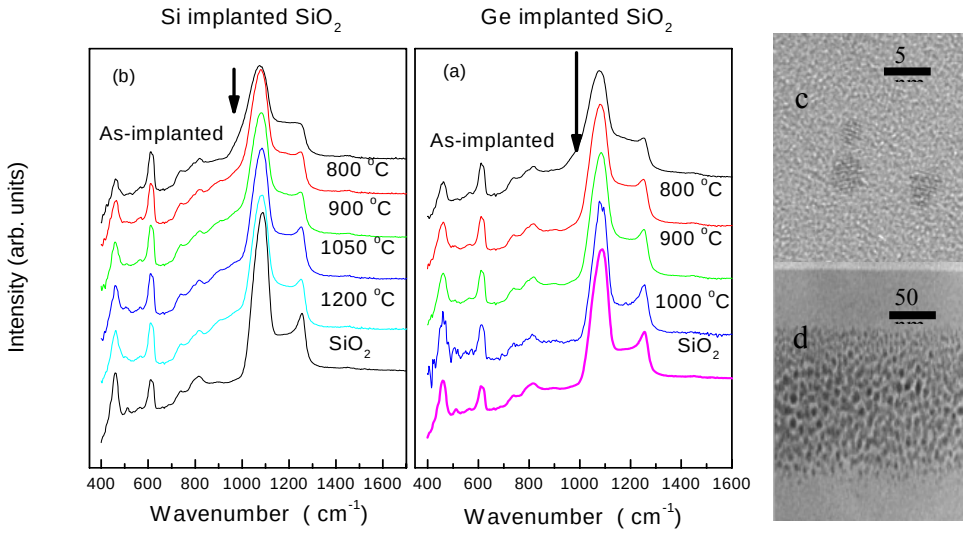

Figure 3.2. FTIR spectra of a) Ge implanted b) Si implanted SiO_2 grown on Si substrate as a function of annealing temperature. c) TEM image of Si nanocrystals formed by ion implantation followed by an annealing process at 1050 ^oC for 2 h. d) TEM image of Ge nanocrystals formed by ion implantation followed by an annealing process at 800 ^oC for 30 min

It is seen from Figure 3.2 that, a shoulder appears at the lower wave number side of the peak at 1081 cm^{-1} in the as-implanted sample. This shoulder is commonly attributed to the presence of nonstoichiometric silicon dioxide, i.e., SiO_x ($x<2$) [59,86,87]. Its intensity decreases with the annealing process, which clearly indicates formation of more stoichiometric SiO_2. The peak shape and the position

AS vibration of the SiO_2 film approach those of pure SiO_2 gradually with the annealing temperature and duration. This is obviously related to the coalescence of the additional atoms to form nanocrystals within the silicon dioxide matrix [41,81]. The effect of annealing differs in Ge and Si implanted cases. Nanocrystal formation can be observed at as low as 700 ^oC in the case of Ge, while heat treatments above 900 ^oC are needed to induce Si nanocrystal formation in the same matrix [44]. This is mainly due to the high mobility and less solubility of Ge atoms in the SiO_2 film [88]. This difference can be seen from the evolution of SiO_x shoulder in Figure 3.2 (a and b). It disappears almost completely at relatively low temperatures for Ge implanted sample, while its presence is still observable in the Si implanted sample even after very high temperature annealing.

In order to verify this qualitative observation, a deconvolution procedure was applied to the samples in the wave number range of 900 and 1400 cm^{-1}. In this process, the position of Si-O-Si AS band of stoichiometric SiO_2 was fixed to 1081 cm^{-1} assuming that this band should be present in all temperatures of annealing due to the presence of unimplanted SiO_2. Thus, one can observe the variation in the Si-O-Si AS band of SiO_x with $x<2$ with respect to the fixed stoichiometric oxide peak. The peak position of stoichiometric SiO_2 (~1081 cm^{-1}) is well-known from many studies reported previously [85-87]. It is also verified from the reference sample with thermally grown stoichiometric SiO_2 used in this work. Other peaks obtained from the deconvolution process were allowed to vary as the samples represent a dynamical system varying with the annealing process.

FTIR spectra and deconvoluted peaks for the samples implanted with Ge at a dose of $1.5x10^{17}$ ions/cm^2 and annealed at 900 ^oC are shown in Figure 3.3 (a and b), respectively. The peak causing the shoulder formation in the main peak is distinguishable at 1033 cm^{-1}. This is apparently related to the presence of non-stoichiometric oxide SiO_x ($x<2$) [59,85,87]. The formation of the SiO_x with $x<2$ is expected as a result of excess Si implanted and the recoil of Si and O atoms during the implantation process. The presence of the excess Ge in the oxide may also generate new chemical bonds like Si-Ge-O, Ge-Ge, Ge-O, Si-Ge and some

individual dangling bonds [89]. It should be noted at this point that although the FTIR spectroscopy is a powerful technique to understand the overall stoichiometry of the SiO_x film with and without excess material, it is hardly possible to obtain more details about the individual oxidation states Si since the peaks are very broad to resolve. The FTIR signal associated with GeO_x, which is usually seen between 830-940 cm^{-1} in the FTIR spectrum is hardly observable in this work [90]. We were unable to fit a peak at this point of the spectra due to the absence of the signal.

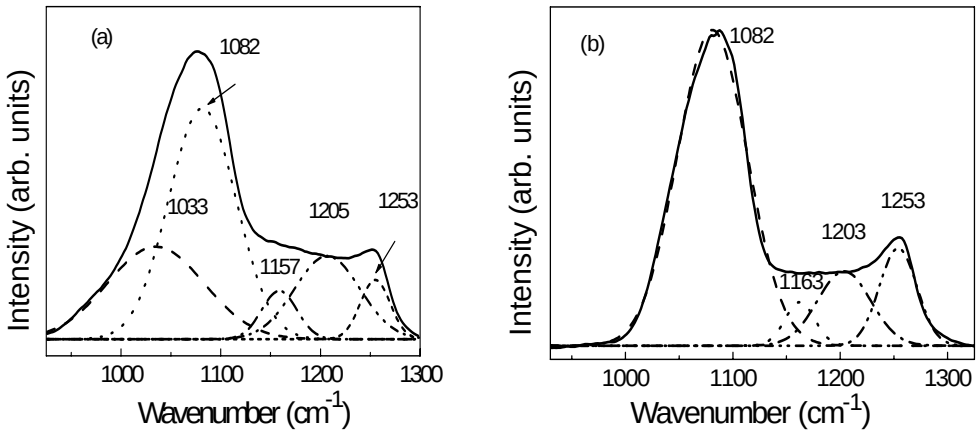

Figure 3.3. The deconvolution of Si-O-Si AS mode of Ge implanted SiO_2 matrix with the dose of $1.5x10^{17}$ atoms/cm^2 a) before annealing b) after annealing at 900 ^oC

During the annealing, Ge atoms coalesce to form nanoclusters in the matrix leading to more stoichiometric SiO_2 formation. This process can easily be revealed in the FTIR spectrum shown in Figure 3.3 (b). The shoulder peak corresponding to the non-stoichiometric oxide in the as-implanted sample disappears completely after the annealing at 900 ^oC. The position of the TO_3 peak becomes almost the same with the Si-O-Si AS mode of thermally grown SiO_2, indicating that the formation stoichiometric SiO_2 with Ge nanocrystals is almost completed at this temperature [38].

For the samples implanted with Si at a dose of $1.5x10^{17}$ ions/cm^2, the deformed oxide bonds recover as excess Si atoms precipitate and form nanostructures in the same way as Ge nanocrystals. However, this process takes place at higher temperatures and with slower rate compared to Ge case. This is in very good agreement with the reported formation kinetics of Si nanocrystals in SiO_2 [44,88].

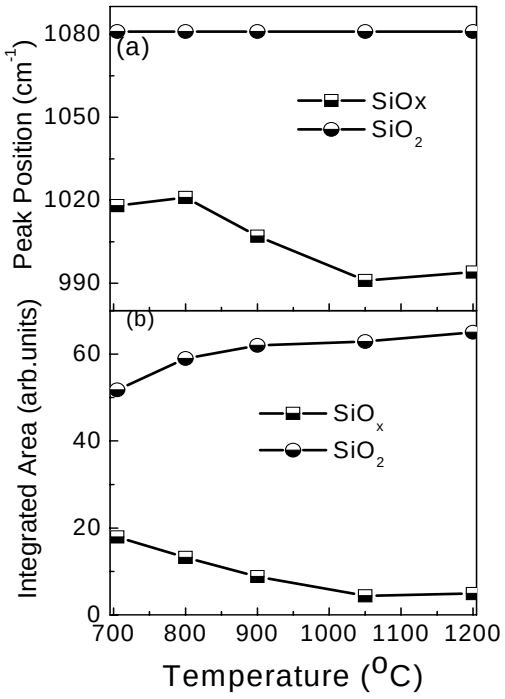

Figure 3.4. a) The shift in the peak position and b) variation of integrated area of Si-O-Si AS band of SiO_2 and SiO_x (x<2) with annealing in SiO_2 sample implanted with $1.5x10^{17}$ Si/cm^2

The variation of the SiO_x peak resolved from the deconvolution process can be better seen by looking at its peak position and integrated area. As shown in Figure 3.4, the peak corresponding to the nonstoichiometric SiO_x (x<2) shifts to lower wave numbers while its integrated area decreases. This is accompanied by the increase in the integrated area of the Si-O-Si AS mode of SiO_2 (Figure 3.4(b)). It is known that the peak position of TO_3 band of SiO_x shifts to lower wavenumbers, with increasing excess Si atoms, and reaches 965 cm^{-1} for x = 1 (SiO) [43,59,87].

Therefore the shift in the peak position of the Si-O-Si AS mode of SiO_x towards lower values is directly related to the increase in the Si content of the SiO_x matrix [57,91]. The decrease in the integrated area of the Si-O-Si AS mode of SiO_x is then related to the formation of a composite system having stoichiometric SiO_2 and Si nanocrystals. Therefore, it is clear that Si rich regions get more Si rich while oxide matrix becomes more stoichiometric during the nanocrystal formation [92]. However, contrary to the Ge nanocrystal formation, the SiO_x signal does not disappear completely even after long annealing durations in the case of Si nanocrystals. This is in agreement with our earlier groups report on photoluminescence properties [83], where it was reported that the PL intensity does not saturate even after high temperature annealing for a long time.

3.3.3 Evolution of the SiO_2 matrix with excess Si and Ge prepared by co-sputtering

As an alternative technique, we used magnetron co-sputtering to prepare Si and Ge nanocrystals in SiO_2. First, a reference sample without any excess element was fabricated by sputtering followed by the annealing at 1100 ^oC for 1 h under N_2 environment for comparison. As it can be seen from the FTIR spectrum shown in Figure 3.5, this sample has an identical spectrum to the thermally grown SiO_2. This shows that the deposited oxide layer is fully stoichiometric.

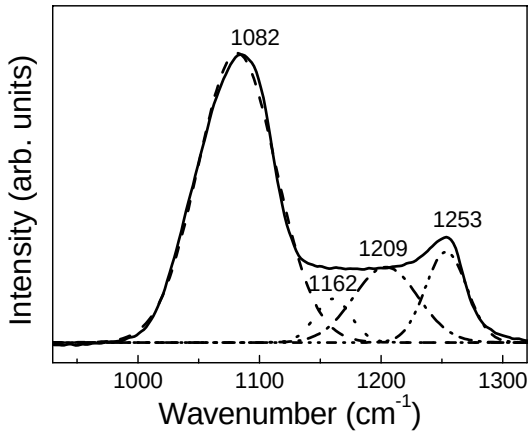

Figure 3.5. The deconvolution of Si-O-Si AS mode of sputtered SiO_2. This sample was annealed at 1100 ^oC in N_2 ambient.

FTIR spectra of the sample with additional Ge and Si atoms are shown in Figure 3.6 (a and b). TEM images of the samples are shown in Figure 3.6 (c and d) for Si and Ge nanocrystals, respectively. Si and Ge nanocrystal formation are clearly seen in both samples. The average nanocrystal size is found to be about 3 nm for Si nanocrytals. In the case of Ge nanocrystals, the nanocrystal size is less than 10 nm. The formation of Ge nanocrystals in these samples was confirmed by the TEM pictures as shown in Figure 3.6 (c) [48]. It is well known that Ge nanocrystals form dark contrast in such systems. The shoulder formation in the FTIR peak of stoichiometric SiO_2 (1081 cm^{-1}) is related to the presence of SiO_x [42,43]. As in the case of the implanted samples, FTIR spectrum approaches that of stoichiometric SiO_2 with the annealing temperature. The deposited oxide turns into a stoichiometric SiO_2 layer as the Ge atoms coalescence and forms nanoparticles within the matrix during the annealing.

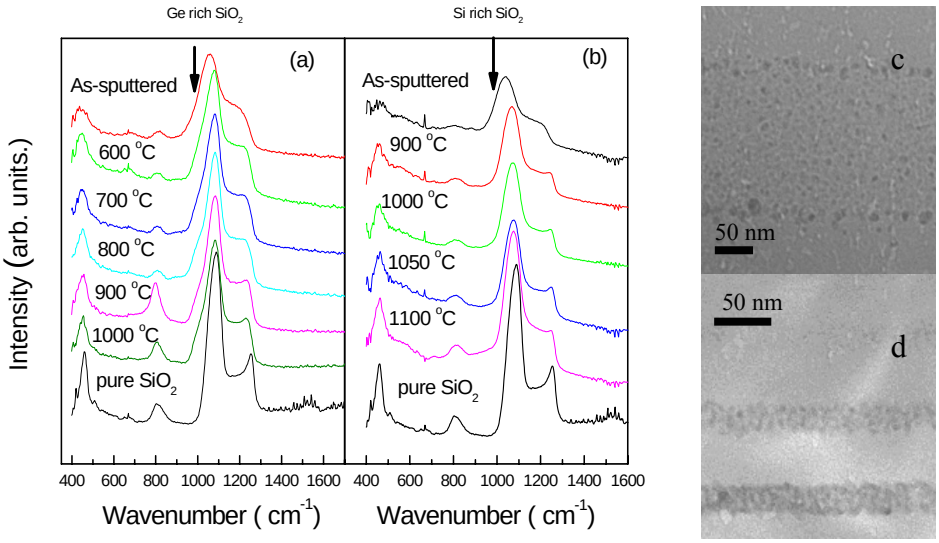

Figure 3.6. FTIR spectra of a) Ge rich b) Si rich SiO_2 grown on Si substrate as a function of annealing temperature c) TEM image of Si nanocrystals formed by sputtering followed by an annealing process at 1050 ^oC for 2 h. d) TEM image of Ge nanocrystals formed by sputtering followed by an annealing process at 600 ^oC for 30 min. Dark band shows nanocrystal regions with different Ge content with annealing temperature

In order to resolve the shoulder of the main peak corresponding to nonstoichiometric SiO_x, we applied the same deconvolution process to these spectra. Again, the peak position of the stoichiometric SiO_2 is fixed at 1081 cm^{-1} and SiO_x peak is allowed to vary during this fitting process. The peak position and the integrated area of the SiO_x are then extracted and plotted as a function of the annealing temperature in Figure 3.7.

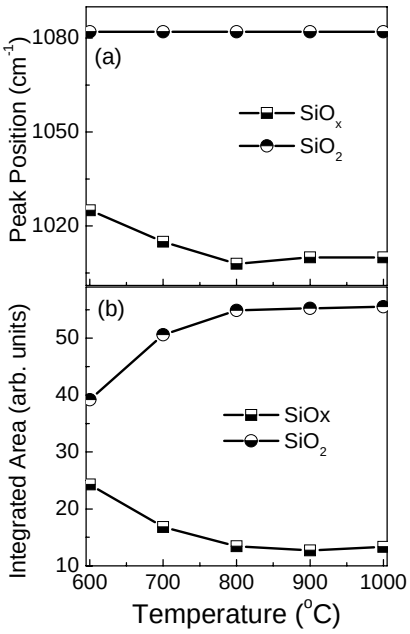

Figure 3.7. a) The shift in the peak position and b) the change in the integrated area of Si-O-Si AS band of SiO_2 and SiO_x ($x<2$) with annealing in Ge rich SiO_2 produced by sputtering

It is seen in Figure 3.7 that the SiO_x peak shifts to lower wave numbers while its integrated area decreases. This is obviously related to the formation Ge nanocrystal within stoichiometric SiO_2 matrix [88]. The peak position and the integrated area saturates at a constant values after 800 ^oC annealing. This indicates that Ge segregation is completed and a stable structure has been formed after this annealing temperature. However, contrary to the ion implantation case, the SiO_x signal does not reach zero value even after the annealing at highest temperature,

showing that there are still some (stable) suboxides after the Ge segregation is completed. This is probably due to the relatively high concentration of Ge nanocrystals in these samples. Significant number of oxygen atoms is shared between Si atoms of the matrix and Ge atoms on the surface of the nanocrystals, giving rise to the observation of non-stoichiometric oxide SiO_x in the FTIR measurements.

In the case of Si nanocrystals formed by co-sputtering, the sputtered oxide layer has a larger concentration of SiO_x with $x<2$ due to the larger amount of excess Si. Figure 3.8 shows the variation of the SiO_x peak extracted from the deconvolution procedure explained above. Upon annealing, excess Si atoms join each other by a diffusion process and form nanocrystals [92].

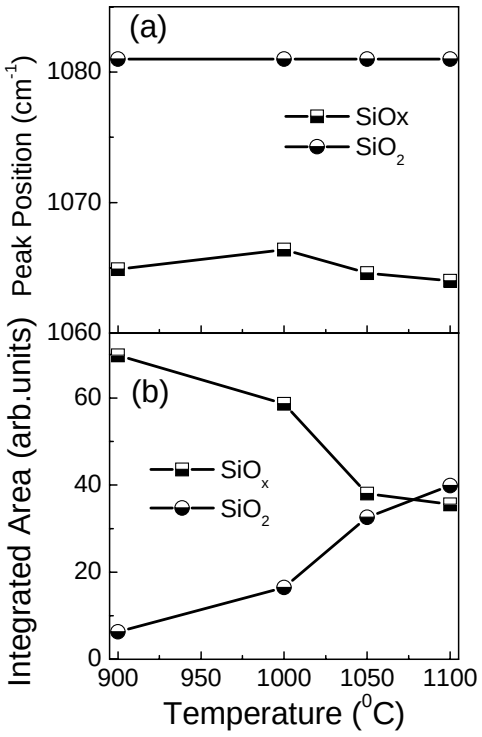

Figure 3.8. a) The shift in the peak position and b) the change in the integrated area of Si-O-Si AS band of SiO_2 and SiO_x ($x<2$) with annealing in Si rich SiO_2 produced by sputtering

We see in general that SiO_x peak position shifts to lower wave number, while the integrated area decreases with annealing temperature [41,81]. However, in this case, the peak position shifts initially to slightly higher wave number at relatively low annealing temperature (i.e., 1000 ^oC) after which it follows the same tendency as the other samples. This reverse shift is probably a result of repositioning of Si and O atoms at the beginning of the annealing process. Si atoms which are initially at interstitial positions come to contact with oxygen atoms and form a non-stoichiometric SiO_x layer in the initial phases of the annealing process.

It is well-known that formation of Si nanocrystals in the SiO_2 matrix requires higher annealing temperature than Ge nanocrystals. This is seen when the spectra given in Figure 3.7 and Figure 3.8 are compared. The integrated area of the SiO_x peak is significantly higher in the samples with excess Si than that measured in the sample with Ge nanocrystals. It decreases with the annealing temperature as the Si nanocrystals develop in the matrix. However, the amount of non-stoichiometric SiO_x is still more in the sample with excess Si than the sample with Ge even after very high temperature annealing. Another important difference between two cases is that both the integrated area and the peak position of the samples with Ge reach a constant, saturated value after an annealing at around 900 ^oC while, for samples with excess Si, their variation continues even at 1100 ^oC. Ge nanocrystal formation is a rapidly developing process which takes place at relatively low temperatures.

3.4. Infrared spectroscopic analysis of AS vibration of SiO_2 during the formation of Fe_2O_3 nanoparticles in the silica matrix

In this part of the chapter, we demonstrate that the FTIR technique can be applied to other composite systems. The study of iron oxide nanoparticles embedded in silica matrix has attracted most attention due to their numerous applications such as magnetic storage media, printing inks, magnetic resonance imaging, drug delivery, biomedicine, biosensors, and magnetic refrigeration due to its extraordinary magnetic and optical properties [93,94]. Iron oxide particles have

been incorporated into silicon dioxide matrix through sol-gel method and silica matrices can be resulted in the limit of the size of iron oxide nanoparticles [95,96].

3.4.1 Experimental

The starting sol was obtained by mixing Tetra Ethyl Ortho Silicate (TEOS) (Aldrich, 98%) and an ethanolic solution (Ethanol, Carlo Erba, 99%) of iron nitrate nonahydrate [$Fe(NO_3)_3.9H_2O$, Aldrich, 98%] with a TEOS : Et-OH : water : HNO_3 molar ratio of 0.057 : 1 : 0.143 : 0.004. The hydrolysis reaction was promoted only by the hydration water of the salt. The sol was stirred for 1 h and then poured into identical vessels. The surface/volume (S/V) ratio which is defined as the ratio of the evaporation surface (the cross sectional area of vessel) by the volume of the sol. In order to obtain S/V ratios 0.04, 2.375 mL volume of sol are used. The vessels were closed using a seal with a small punched hole and then heated in an oven at 60^{o}C up to the gel point. The fresh monolithic gels were directly calcined at 400 ^{o}C in static air for 4 h and then powdered.

3.4.2 FTIR Analysis

FTIR absorption measurements were done with unpolarized light at a normal incidence between 400-4000 cm^{-1} range with a resolution of 4 cm^{-1}. Pure KBr pellet was used as a reference. The deconvolution procedure was applied. There are three main FTIR absorption bands located at around 459 (TO1), 810 (TO2), 1075 cm^{-1} (TO_3) corresponding with rocking, bending and AS vibration of SiO_2 respectively [41,81,86]. Among them the AS vibration of Si-O-Si was the most prominent, representative, and sensitive to structural variations of the silica matrix. The intensity, peak position and the form of this band are dependent on the stoichiometry of the silica matrix [41]. Therefore, deconvolution procedure was applied peaks located in the range of 900-1400 cm^{-1}. Figure 3.9 (a) shows the of Si-O-Si AS band of silica matrix, which is gelated at room temperature (RT). The peak located at ~1073 cm^{-1} was assigned as third transverse optical mode (TO_3) of Si-O-Si asymmetric vibration in which adjacent oxygen atoms move in phase, whereas the peak at 1259 cm^{-1} was assigned to the longitudinal part of TO_3 mode of Si-O-Si AS band in the silica matrix, LO3 [59,85,86]. The peak at ~1208

cm^{-1} was described as the fourth transverse optical mode (TO4) in which adjacent oxygen atoms move out of phase. The longitudinal optical resonant mode (LO4) of the same peak was located at ~1165 cm^{-1} [85]. The presence of Fe_2O_3 precursors in the sol-gel structure may disturb the stoichiometry of the silica matrix and consequently change the absorption spectrum of the SiO_2 structure. The presence of Fe_2O_3 precursors in the matrix results in a shoulder at the lower wavenumber side of the IR spectrum of the SiO_2 structure [81]. In order to investigate this feature, the deconvolution procedure was applied to the same peak (1075 cm^{-1}) of the FTIR spectrum of fresh monolith containing Fe_2O_3 precursors and gelated at room temperature.

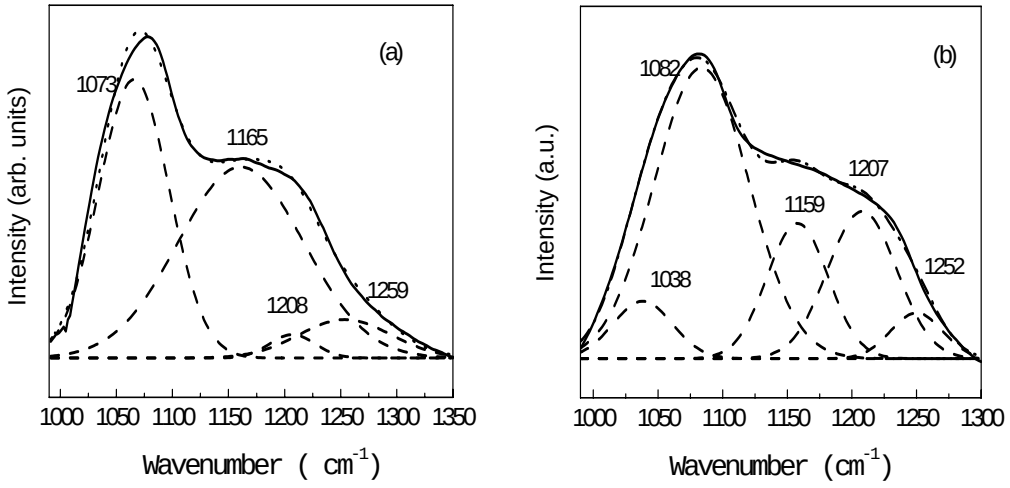

Figure 3.9. The deconvolution of Si-O-Si AS mode of a) silica pellets b) iron oxide-silica nanocomposites pellets at RT

As can be seen from Figure 3.9(b), although there were only slight changes at the peak positions of the vibrational modes mentioned (TO_3, TO_4, LO_3, LO_4), the FWHM of the peak at 1165 cm^{-1} decrease, meanwhile the FWHM of the peak at 1208 cm^{-1} increased. It is well-known in the literature that, if the silicon dioxide matrix is non-stoichiometric due to several reasons (such as oxygen deficiency, impurity etc.), a SiO_x related mode should appear at the lower wavenumber side

of the FTIR spectrum [17]. Since SiO_x (x<2) structure gives an AS Si-O-Si vibration mode at the wave number (1038 cm^{-1}) [59,81], this emerging peak is generally accepted as the "disorder indicator" of the silica structure, and depending on the increase in the calcination temperature applied to the iron oxide, the changes in its properties were demonstrated to be good indication for the formation of γ- Fe_2O_3 nanocrystals [81].

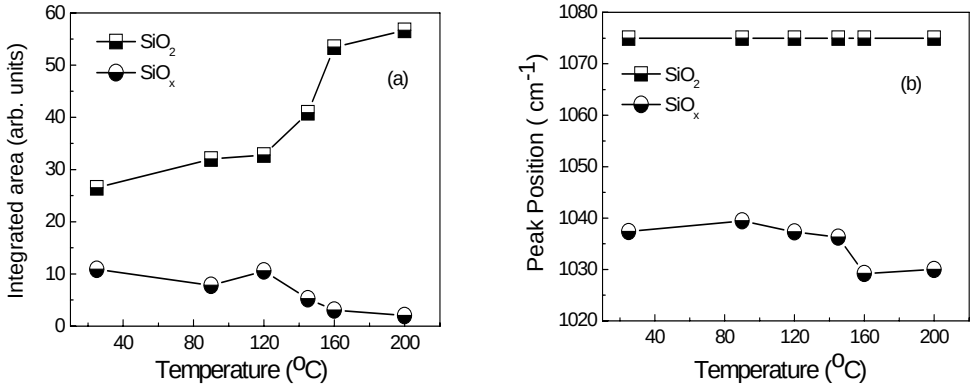

Figure 3.10 a) The variation in the integrated area and b) the shift in the peak position of the Si-O-Si AS mode of SiO_2 and SiO_x (x<2) with calcination temperature for γ-Fe_2O_3-silica nanocomposites

A detailed study of the integrated area of Si-O-Si the asymmetric stretching mode of SiO_2 and SiO_x for the iron oxide-silica nanocomposite is presented in Figure 3.10. It is shown in this figure that with an increase in calcination temperature the integrated area of the Si-O-Si AS mode of SiO_2 increases from 26 to 57 arb.units, while that of SiO_x related peak decreases from 11 to 2 arb.units with the calcination temperature and it disappears at 400 ºC. This fact is well correlated to the restoration of the SiO_2 structure after maghemite nanocrystal formation [44,81].

The peak position of Si-O-Si the AS mode of SiO_2 and SiO_x for the iron oxide-silica nanocomposite is demonstrated in Figure 3.10(b). In the deconvolution process, the position of Si-O-Si asymmetric stretching band of stoichiometric

SiO_2 was fixed to 1075 cm^{-1} assuming that this band should be present in all temperatures of calcination due to the presence of silica matrix. Thus, one can observe the variation in the Si-O-Si AS band of SiO_x with $x<2$ with respect to the fixed stoichiometric oxide peak. The peak position of the Si-O-Si the AS mode of SiO_x shifts from 1037 cm^{-1} to 1030 cm^{-1}. This shift can be related to the precipitation of the Fe_2O_3 atoms to form the nanocrystals and consequently to the recovery of the silica matrix [18,19,82]. This fact is possibly also correlated to the recovery of the SiO_2 structure after maghemite nanocrystal formation [41,81,84]. These results indicated that the recovery of the silica matrix and the formation of the Fe_2O_3 nanoparticles start at low calcination temperature and completes before 400 ^oC [41,81,84]. These observations of maghemite nanocrystals were also confirmed by XRD and TEM measurements [97] and the literature values. Therefore we conclude that FTIR measurements can also be used for monitoring the Fe_2O_3 nanocrystal formation in silica matrix.

3.5. Summary and Conclusion

In this chapter, we employed FTIR spectroscopy to study the structural variations in oxide matrix during the Ge and Si nanocrystal formation prepared by ion implantation and sputtering techniques. It is shown that FTIR spectra of the matrix correlate well with nanocrystal formation which can be observed and quantified by monitoring the FTIR signal resulted from the formation of nonstoichiometric suboxide SiO_x with $x<2$. The excess Si or Ge atoms coalescence to form nanocrystals the matrix becomes more stoichiometric as tracked from the decrease in the integrated area and the shift in the peak position of the suboxide peak. The variation of AS mode of SiO_x bond in the FTIR spectrum can thus be used to monitor the nanocrystal formation within the oxide matrix. A comparison between SiO_2 doped with Si and Ge show that the transformation of the matrix and the nanocrystal formation starts at lower temperatures in Ge case and gets rapidly completed. The process of Si nanocrystal formation in the Si rich SiO_x matrix takes place at relatively higher temperatures and with a slower rate.

Moreover, the same technique was also employed to understand of Fe_2O_3 nanoparticle formation in the silica matrix as a function of calcination temperatures. The recovery of the Si-O bonds was monitored to study the correlation between the structural variation of the silica matrix and Fe_2O_3 nanoparticles formation. Formation of the stoichiometric SiO_2 starts at low temperature in the γ-Fe_2O_3-silica nanoparticles, and almost completed for the γ-Fe_2O_3-silica nanoparticles calcinated at 200 ^oC. The integrated area of the Si-O-Si AS mode of stoichiometric SiO_2 reaches to that of bulk SiO_2 for the samples calcined at 400 ^oC. The peak position of the Si-O-Si AS mode of non-stoichiometric SiO_x shifts to the lower wavenumber, while that of stoichiometric SiO_2 is constant. These results are well correlated with the recovery of the silica matrix, and they also indicate the formation of the Fe_2O_3 nanoparticles indirectly.

CHAPTER 4

FABRICATION AND CHARACTERIZATION OF NANOCRYSTALLINE SiC:H BY PECVD

4.1. Introduction

Thin films of amorphous and polycrystalline SiC have attracted much attention in the last decade due to its potential applications for microelectronic and optoelectronics devices. The most important characteristic of SiC is its wide optical band gap, which can be varied by increasing the methane flow in the precursor gas mixture during the fabrication. The optical band gap of pure amorphous SiC vary in the region of 1.8-2.2 eV, while that of crystalline SiC is in between 2.0-2.7 eV [98]. For high methane concentration, the quality of the material is reduced, causing the formation of graphitic phase in the film. Recently, it has been shown that SiC can be deposited by the PECVD from precursor gases diluted with hydrogen. In this growth process, it is assumed that amorphous and polycrystalline phases of SiC can be grown simultaneously [99,100]. However, only a few studies have investigated the influence of different methane and hydrogen dilution ratios on fabrication of SiC film at low substrate temperature. Therefore understanding the effect of methane fraction and hydrogen dilution on

growth process is still needed for improving and optimizing of the SiC film for various applications.

In fact, at low substrate temperature it is not possible to grow crystalline SiC on Si due to lattice mismatch of about 20%. The crystalline growth is possible only at substrate temperature higher than 1200 ^{o}C with the CVD technique [100]. However, this high substrate temperature causes unintentional impurity doping. Moreover this high temperature value is very close to melting point of Si substrate, causing significant Si diffusion into the growing film. In order to get rid of these undesirable effects, the thermal annealing of amorphous film deposited on Si can be used to form polycrystalline SiC as an alternative and simple method. So, a detailed and comprehensive study focusing on crystallization process is a great of interest.

In this chapter, the effect of methane fraction and hydrogen dilution ratio on the properties of the film growth film, and the transition from amorphous to crystalline SiC film have been investigated by various diagnostic techniques such as FTIR spectroscopy, Raman spectroscopy, XRD, and optical transmission measurement in a systematic way.

4.2. Experimental Details

4.2.1 Film growth

SiC films were deposited by the RF PECVD technique with a frequency of 13.56 MHz. Electrodes with diameter of 14 cm were kept at a distance of 2 cm. Prior to deposition, the substrates were exposed to the in-situ Argon plasma for 5 min at 350 ^{o}C with the power of 10 W and the pressure 0.5 mbar to eliminate the unwanted contamination. The films were simultaneously deposited on p-type Si (100) wafers and quartz substrates to facilitate use of different diagnostic techniques.

4.2.2 Deposition parameters of the a-SiC:H

CH_4 (99.9999 %), SiH_4 (99.9999 %), and H_2 (99.9999 %) were used as the precursor gases to deposit the SiC films. Two set of samples were prepared to study the deposition condition of the PECVD system. The substrate temperature was kept constant at 350 ^oC, which is low with respect to conventional PECVD method. In all depositions, RF power, gas pressure, and the total gas flow (SiH_4 +CH_4) were fixed at the value of 40 W, 2 mbar, and 10 sccm, respectively. In the first set of samples, the methane fraction, X_C, $[CH_4]$ / ($[SiH_4]$ + $[CH_4]$) was varied to understand the effect of methane fraction on the film properties. In the second set of the samples, the methane fraction was kept constant, while the hydrogen dilution ratio, R_H, $[H_2]$ / ($[SiH_4]$ +$[CH_4]$) was varied from 20 to 5 to examine the effect of hydrogen dilution on the transition from the amorphous to crystalline phase of the films. The deposition parameters are summarized in Table 4.1.

Table 4.1 Deposition parameters of prepared samples

Sample no	Depos. Time (min)	Thickness (μm)	Depos. Rate (Å/s)	CH_4 Fraction X_c	H_2 Dilution Ratio, R_h	Gas Flow CH_4:SiH_4 (sccm)	H_2 Flow (sccm)
14	90	1.09	2.0	0.90	5	1.0 : 9.0	50
15	96	1.45	2.5	0.87	5	1.3 : 8.7	50
16	105	1.24	2.0	0.93	5	0.7 : 9.3	50
17	60	1.00	2.8	0.85	5	1.5 : 8.5	50
24	70	0.96	2.3	0.87	10	1.3 : 8.7	100
26	75	0.94	2.3	0.87	15	1.3 : 8.7	150
28	90	0.83	1.5	0.87	20	0.65 :4.35	100

The as-deposited samples were cut into small pieces for thermal treatment. In order to diffuse slowly out the hydrogen from the film, the samples were annealed at 450 ^oC for 30 min under vacuum. After that, samples were annealed between 900-1100 ^oC for 1 h under the vacuum.

4.2.3 Analysis Techniques

The thickness of the as deposited films was measured by Dektak profilometer. The chemical bond structure of the grown films was investigated by FTIR spectroscopy. Raman measurements were performed using a Jobin Jvon Raman Spectrometer equipped with an Argon laser (488 nm) for excitation in the wave number range of 200-2000 cm^{-1}. The optical transmittance measurement was performed by means of a Perkin-Elmer Lambda 35 spectrophotometer in the wavelength range of 200-800 nm. Absorption coefficient, α, for $\alpha>10^4$ was calculated from the optical transmission spectra by using the Tauc equation $\alpha h\nu = (h\nu - Eg)^2$ [4]. The optical energy gap, E_g, was determined using Tauc's formula [4]. The crystallinity of the deposited and annealed films was investigated using XRD analysis with 2θ values between 25 and 50° at 0.02° steps.

4.3. Results and Discussion

4.3.1. Effect of SiH_4 and CH_4 Gas Flow on the Stoichiometry and Crystallinity Deposited SiC Film

As shown in the Table 4.1, a set of sample (no:14-17) were produced with varying gas flow at fixed hydrogen dilution ratio.

4.3.1.1 FTIR Spectroscopy

Figure 4.1 shows the FTIR spectra of SiC:H film as a function of methane fraction, X_c for the samples a) as deposited and b) annealed at 900 ^oC under vacuum. For as deposited samples, the dominant vibration located at 780 cm^{-1} is corresponded to Si-C stretching vibration [101,102]. The small shoulder located at around 1000 cm^{-1} is typically attributed to SiC-H_n vibrations [103,104]. The small peaks at around 1250 and 1350 cm^{-1} are assigned to the SiC-H_3 bending vibration. Si-H_2 and CH_n stretching vibrations are located at around 2100 cm^{-1} and 2890 cm^{-1}, respectively [103].

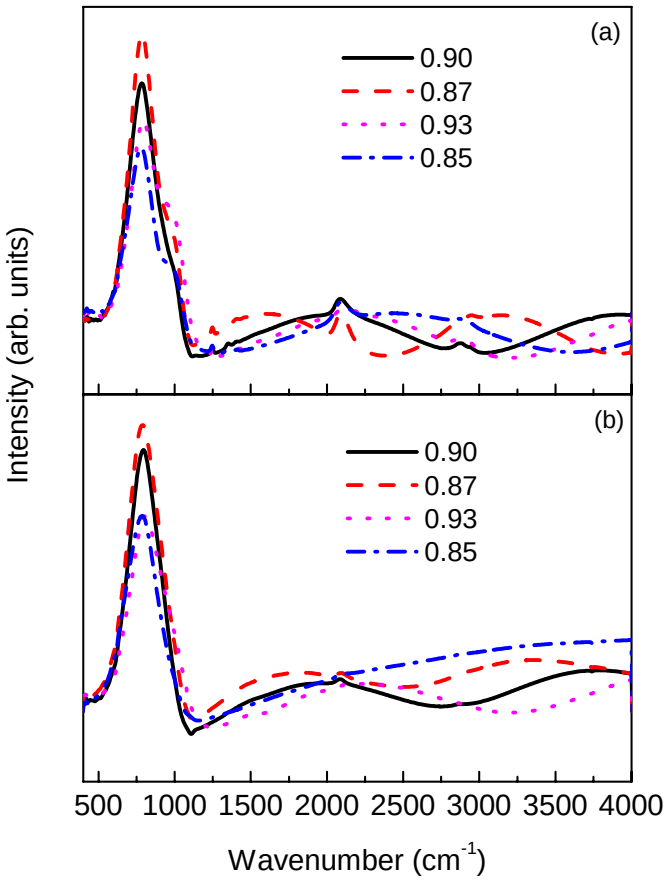

Figure 4.1. FTIR spectra of SiC:H film as a function of methane fraction X_c for the samples a) as deposited b) annealed at 900 ^oC

Upon annealing, the shoulder of the main peak, which is attributed to SiC-H_n vibration, disappears as seen in Figure 4.1 (b) as a result of hydrogen diffusion out of the film. Similarly, other hydrogen bonded vibrations (Si-H_2, CH_n stretching, SiC-H_3 bending) disappear in the spectrum after the annealing. FTIR spectra indicate that the deposited and annealed films are stoichiometric SiC [104,105].

4.3.1.2 Raman Spectroscopy

Raman spectroscopy is used for chemical-structural characterization of the SiC film and identification of polytype of SiC. Figure 4.2 represents Raman spectra of the SiC film as a function methane fraction before and after an annealing treatment.

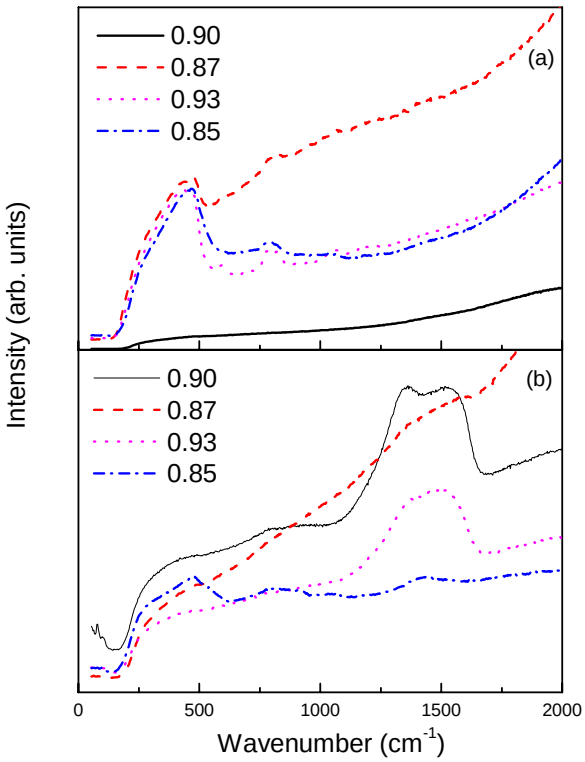

Figure 4.2. Raman spectra of SiC:H film as a function of methane fraction X_c for the samples a) as deposited and b) annealed at 900 ^{o}C

For as deposited sample (no: 14) no specific vibrations could be detected. Other samples exhibit spectral features of hydrogenated amorphous SiC. There are three vibration modes recognized in these spectra. All samples show the prominent band at about 470 cm^{-1} associated with LA mode of Si-C. This scattering is usually observed in amorphous SiC with or without very small size crystalline regions in the film [106,107]. The weak peak seen at ~595 cm^{-1} is attributed to disordered SiC, which is almost the same for all different methane fractions [108]. The peak at ~798 cm^{-1} is ascribed to the TO mode of Si-C vibration [109,110]. The intensity of TO mode of Si-C increases with increasing methane fraction. Before the annealing, no graphite related vibrations were observed in the spectrum.

The Raman spectra of the annealed samples are displayed in Figure 4.2 (b). In this case, the intensity of the LA and TO modes of SiC vibration located at 470 and 798 cm^{-1} remains the same. The new weak peak which is observed at 960 cm^{-1} can be assigned to LO mode of Si-C vibration [108,109]. The new Raman bands are located at the higher wavenumber side of the spectrum are associated with the formation of diamond structure (i.e. C-C bonds) in the film. For X_c= 0.85, the diamond precursor is seen between 1300-1600 cm^{-1} [98]. For X_c= 0.90 and 0.93, the presence of graphite is clearly visible in the spectrum after annealing. It consists of a broad D and G band around 1350 and 1560 cm^{-1}, respectively [98]. The intensity of D band results from sp^3 sites in the diamond structure, but that of G band come up from all sp^2 sites in the graphite formations [108]. For X_c= 0.87, neither Si crystallite formation nor the presence of graphite phases was detected in the Raman spectrum (Figure 4.3(b)). Together with FTIR data represented above, these results are indicating that the methane fraction of X_c= 0.87, yields the best stoichiometr [98].

4.3.1.3 Optical Transmission Spectroscopy

Optical transmission spectroscopy is used to study the optical properties of the SiC film and determine the band gap of the SiC films deposited by PECVD. The maximum transmittance at 555 nm is 95% for X_c= 0.87. The high optical transmittance is a result of almost transparent stoichiometric and amorphous SiC structure [109]. The transmittance for other methane fractions is about 80%, and form of the transmittance spectra introducing amorphous-based structure (not shown in Figure). For high methane fraction, the maximum transmittance at ~750 nm is about 20%. The excess carbon concentration in the film resulted in clusterization in the graphitic phase, as revealed by the decrease in the transmittance [110].

Figure 4.3 represents the Tauc plot of SiC film as a function of methane fraction before and after the annealing. Before the heat treatment, the wide band gap is obtained at the methane fraction, X_c= 0.87. After the annealing process, band gap

of the deposited films decreases due to formation of graphitic phase in the film [111].

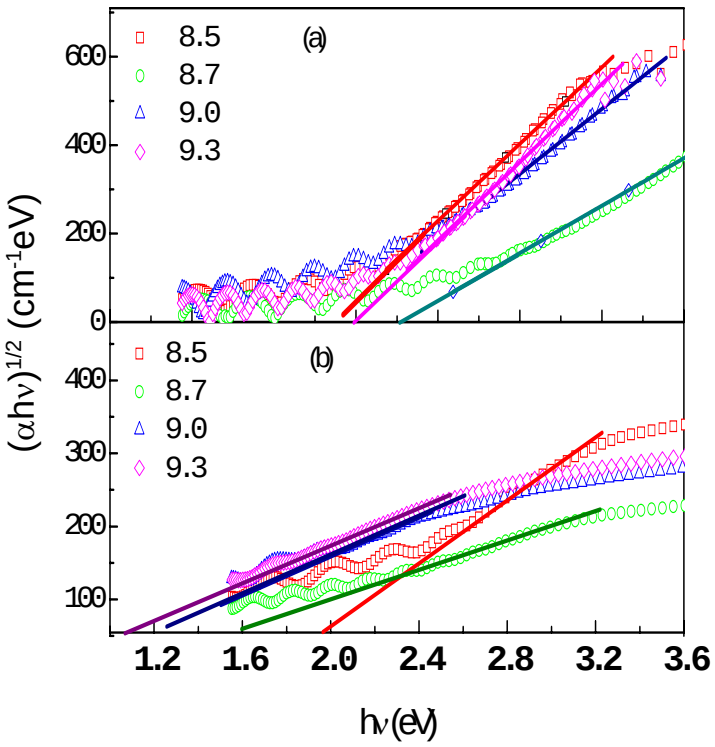

Figure 4.3 The Tauc plot of SiC film as a function of methane fraction X_c a) before and b) after annealing

Figure 4.4 shows the deposition rate and optical band gap of SiC film as a function of methane fraction X_c. The deposition rate was determined by dividing the film thickness with deposition time. The optical band gap energy of SiC film was estimated by using the Tauc plot. With increase of methane fraction X_c, R_d decreases from 2.78 Å/s at X_c = 0.85 to 1.97 Å/s at X_c = 0.93 due to larger dissociation energy of the CH_4 molecule (413 kJ/mol) than that of SiH_4 molecule (299.2 kJ/mol) [102,112]. Whereas, the E_g increases from 2.29 eV at X_c = 0.85 to 2.62 eV at X_c = 0.87 with increase of methane fraction, indicating the optimum methane fraction to get wide band gap material [102]. E_g decreases at above X_c = 0.87, because of passing over the stoichiometric composition of the film

[109]. However, it is hard to interpret the variation of E_g with increase X_C, due to inhomogeneity of the film surface.

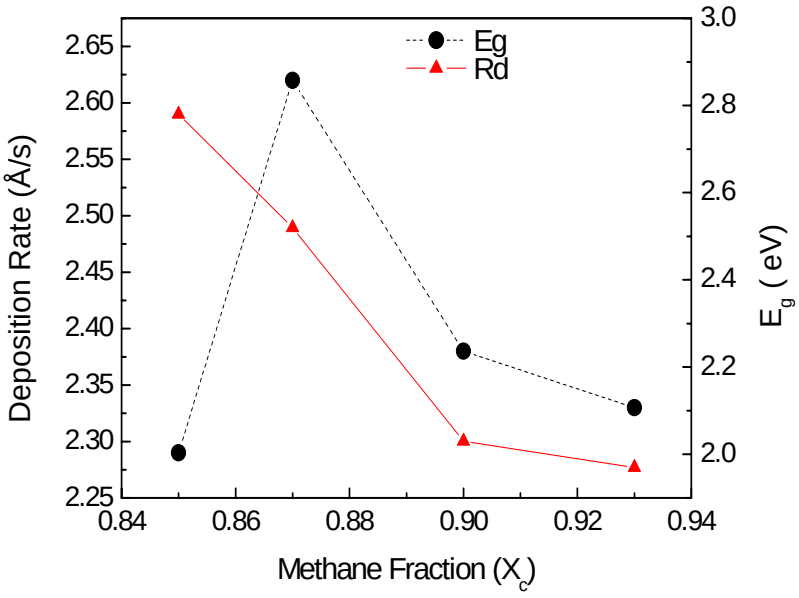

Figure 4.4. The variation of the deposition rate and the optical band gap of the SiC film as a function of methane fraction

4.3.2 Effect of Hydrogen Dilution Ratio on the Stoichiometry and Crystallinity Deposited SiC Film

As seen in the Table 4.1, a set of sample (no: 24, 26, 28) were produced with varying hydrogen dilution ratio at fixed methane fraction. These samples were characterized with main diagnostic techniques.

4.3.2.1 FTIR Spectroscopy

Figure 4.5 shows FTIR spectra of SiC:H with hydrogen dilution ratio before and after annealing. The intensity of Si-C stretching vibration at 780 cm^{-1} enhanced with hydrogen dilution ratio [99,102]. Si-H stretching peak is clearly visible at 2100 cm^{-1} for as deposited samples. We see also that the intensity of the CH_n stretching vibration at ~2890 cm^{-1} decrease with the increasing hydrogen dilution ratio, R_H [102]. Similarly, the intensity of Si-CH_n (in 1250 cm^{-1}) and CH_n (in 2890 cm^{-1}) vibrations decrease with the R_H [102]. The shoulder of the Si-C stretching

vibration also disappears with increasing hydrogen dilution R_H for as deposited sample [99,102]. These results indicate the H_2 etching effect during the deposition in which H_2 attacks the carbon related bonds preferentially. It is revealed in the Figure 4.5 that the intensity of Si-H stretching vibration (2100 cm^{-1}) decreases, but does not totally disappear for higher R_H value. However, the CH_n related vibrations almost disappear for the R_H value higher than 10, which is consistent with the preferential carbon etching of hydrogen [99].

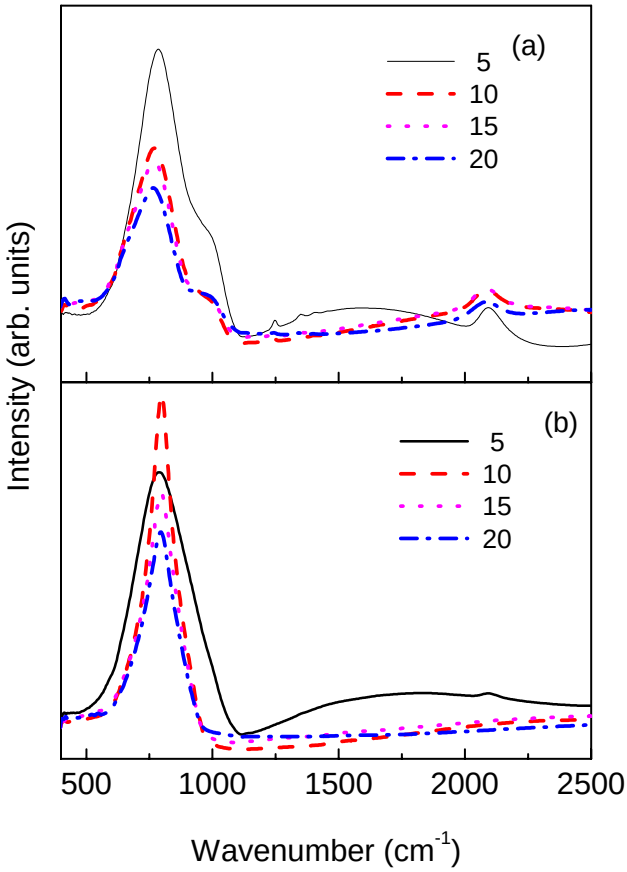

Figure 4.5. FTIR spectra of SiC:H film as a function of hydrogen dilution ratio, R_H for the sample a) as-deposited b) annealed at 900 ^oC for 1 h under vacuum

After the annealing process, hydrogen related bonds disappear in spectra shown in the Figure 4.5(b) due to the H_2 diffusion out of the film. The prominent decline in the hydrogen content of the annealed sample is obtained from the FTIR spectra

(Figure 4.5 (b)) with increasing of R_H. This variation is accompanied by the decrease in the CH_n and $SiC-H_n$ [99]. The FWHM of the Si-C vibration decreases with the hydrogen dilution after the annealing treatment [99,113]. This implies that the film becomes more stoichiometric after the annealing [113,114].

4.3.2.2 Raman Spectroscopy

Figure 4.6 shows the Raman spectra of the samples with varying hydrogen dilution ratio, R_H, before and after annealing. For as-grown samples, the intensity of the LA mode of Si-C vibration at 470 cm^{-1} decreased with increasing R_H, indicating that structural evolution of the SiC film is enhanced, due to formation of polycrystalline SiC film [104,106]. In addition, the intensity of TO mode of Si-C vibration at ~798 cm^{-1} decreased with the increasing R_H, because of hydrogen etching effect of C-C and Si-Si bonds. This result agrees well with the FTIR spectra presented above. We can then conclude that the composition of the film is becoming more stoichiometric with increasing the hydrogen dilution ratio.

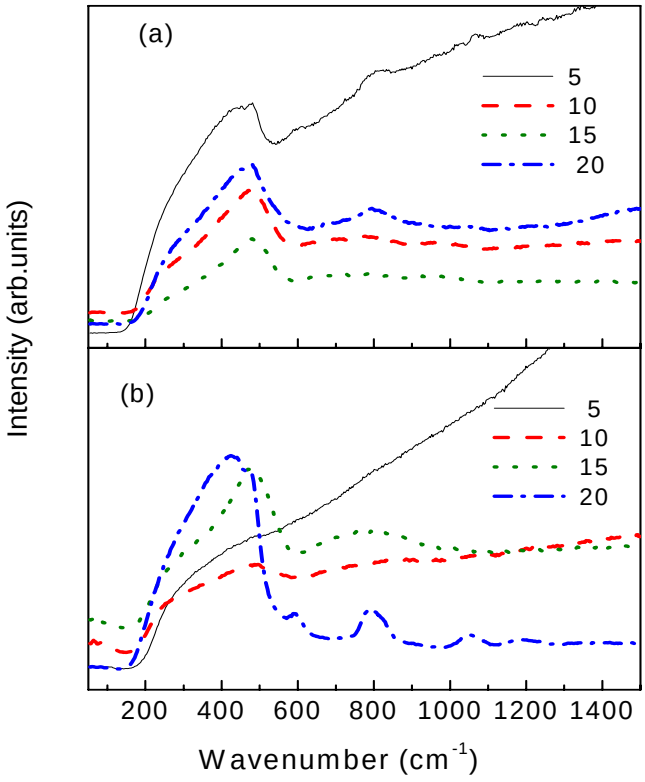

Figure 4.6 Raman spectra of SiC:H film as a function of hydrogen dilution ratio R_H for the samples a) as deposited and b) annealed at 900 ^oC

For Raman spectra of the annealed samples in Figure 4.6(b), the LA mode of Si-C vibration at 470 cm^{-1} can be seen in all samples except for the one with R_H=5 where this peak is hardly identifiable. For R_H = 10 and 15; the broad and weak TO mode of SiC vibration at 798 cm^{-1} indicates the presence of amorphous SiC film [108,109]. For hydrogen dilution ration of 20, this peak has a more pronounced and sharper feature indicating that the crytallinity of the film is improved with the increasing R_H [108]. This observation is interpreted that the SiC film for R_H = 20 consists of nanocrystalline SiC islands surrounded by amorphous network [106]. The influence of the annealing temperature on the crystallinity of the SiC film is discussed for the sample prepared with R_H = 20 in section 4.3.3.

4.3.2.3 Optical Transmission Analysis

Figure 4.7 represents Tauc plot of the transmission spectra of SiC:H films with varying R_H value before and after the annealing treatment. Before the heat treatment, a relatively wide band gap is obtained at R_H = 20. After the annealing process the band gap of the films increased in correlation with the crystallinity of the film.

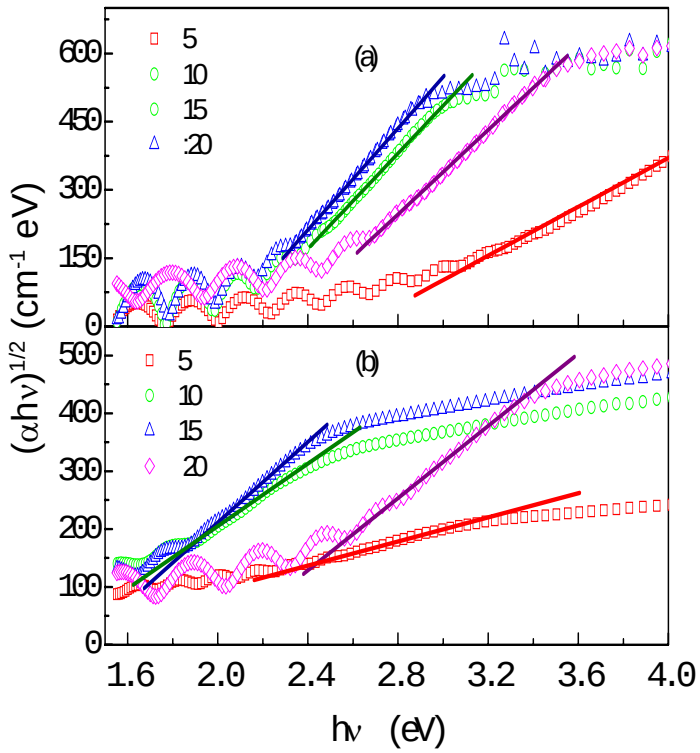

Figure 4.7. The Tauc plot of SiC films as a function of hydrogen dilution ratio a) before and b) after annealing

Figure 4.8 displays the variation of deposition rate, R_d and optical band gap of SiC film as a function of hydrogen dilution ratio, R_H. R_d decreases monotonically from 2.52 Å/s at $R_H = 5$ to 1.54 Å/s at $R_H = 20$. The variation of R_d can be associated with hydrogen etching effect [103,109]. Also, the decrease of precursor gas (CH_4 and SiH_4) flow is obtained with increasing R_H at a constant X_c= 0.87. The low flow rates of these gases resulted in reduced the amount of deposited Si or C based structures. So, the deposition rate of the film reduces with increasing the hydrogen dilution ratio [102]. However, the optical band gap of the film increased with the increasing the hydrogen dilution ratio. The band gap E_g is varied from 1.12 eV at $R_H = 5$ to 2.01 eV at $R_H = 20$ for the samples after the annealing in Figure 4.8. This indicates that the formation of the required wide band material

can be obtained with increasing hydrogen dilution ratio, via selectively etching effect of hydrogen.

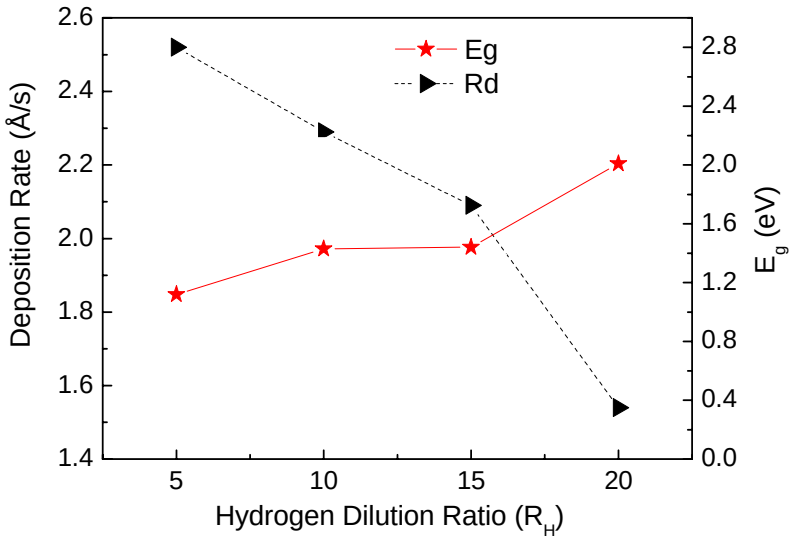

Figure 4.8. The variation of deposition rate, R_d and optical band gap of SiC film as a function of hydrogen dilution ratio, R_H

In order to inspect the effect of annealing on the crystallization of the SiC film in section 4.3.3, a reference sample was prepared at X_c = 0.87 and R_H = 20 and analyzed. Results of this study are given in section 4.3.3.

4.3.3 Effect of Thermal Treatment on the Stoichiometry and Crystallinity Deposited SiC Film

In order to examine the effect of different annealing temperature from 900 ^oC to 1100 ^oC on the crystallization process of SiC:H, samples (sample no: 28) were prepared at a fixed methane fraction and hydrogen dilution ratio X_c = 0.87 and R_H = 20, respectively. The samples were cut into small pieces for annealing. Each part of the sample was annealed at different temperature under vacuum for 1 h. Other deposition parameters of the sample can be seen in the Table 4.1. Major diagnostic techniques were performed to characterize the annealed samples.

4.3.3 1 FTIR Spectroscopy

FTIR was performed to further analyze of crystallization of the SiC film as a function of annealing temperature. The corresponding FTIR spectra are shown in Figure 4.9 for the samples annealed at different temperatures. It is worth pointing that, Si-H and CH_n stretching, Si-CH_n rocking vibrations are not observed in the FTIR spectra (Figure 4.9), indicating the very low hydrogen content in the film [102,103].

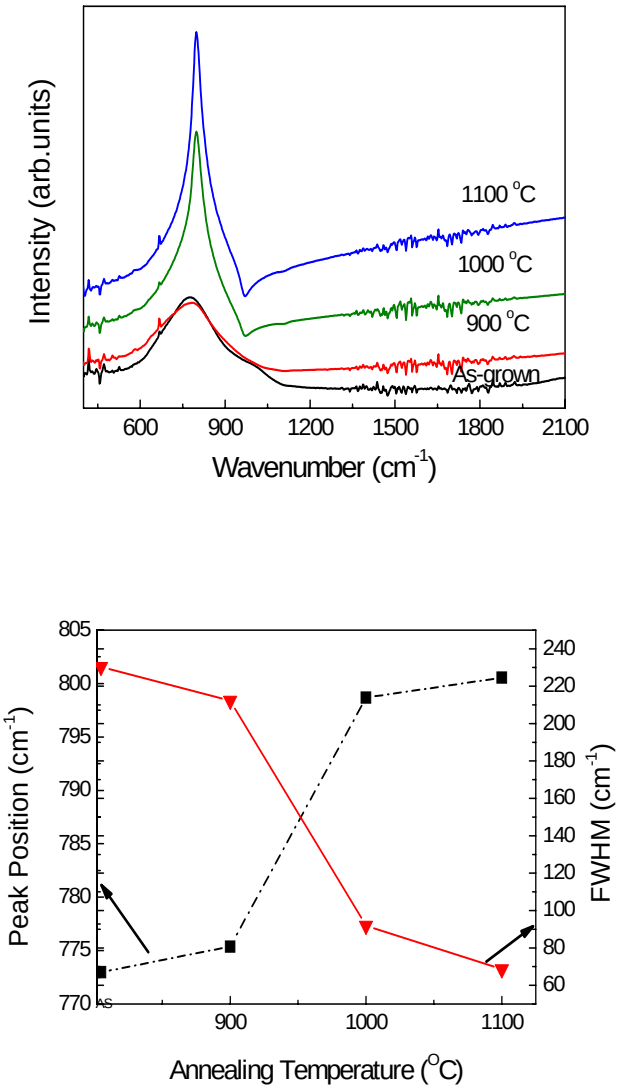

Figure 4.9. a) FTIR spectra of the film as a function of annealing temperature b) the variation of FWHM and peak position of Si-C stretching vibration as a function of annealing temperature

All the spectra show Si-C stretching vibration at ~790 cm^{-1} [115,116]. The shape of that peak changes from Gaussian like to Gaussian- Lorentzian shape which corresponds to the crystallization of the film as a function of annealing temperature. Furthermore, the peak position shifts to the higher wavenumbers (Figure 4.9 (b)) with increasing temperature. The peak shift in the Si-C stretching mode is related to the variation in the Si-C bond composition (such as decrease in the bond length, bond angle). A decrease in the bond length of the Si-C stretching indicates a compressive strain in the film. This result suggests the formation of nanocrystalline structures in the amorphous SiC matrix [117,118].

The FWHM of Si-C stretching vibration decreases as seen in the Figure 4.9 (b). M. Wang et al. [119] studied the changes in the FWHM of Si-C stretching vibration in the film with different annealing temperatures from 400 ^{o}C to 700 ^{o}C, and attributed the decrease in the FWHM to the formation of crystalline SiC film [119,120]. We can then conclude that the structure of the Si-C film changes from amorphous to crystalline phase at high annealing temperatures. This is inferred from the reduction in FWHM value in Figure 4.9 (b) [117].

4.3.3.2 X-Ray Diffraction

The XRD measurement is used to investigate the evolution of the crystalline phase of SiC film with the annealing temperature. XRD scans were carried out at a scan speed of 0.2 ^{o}/min with scan steps 0.02 ^{o}. As seen in Figure 4.10, β-SiC phase related peaks become visible after high temperature annealing. The (111) and (200) planes of β-SiC are detected at $2\theta = 35.77^{o}$ and $2\theta = 41.58^{o}$ in the samples annealed above 1000 ^{o}C, respectively [102,117]. Among them the (200) appears to be stronger than the others. However XRD peaks related to the hexagonal SiC (α-SiC) formation have not appeared in the measured spectra. Below 1000 ^{o}C, the SiC film was found to be amorphous. These results indicate that the SiC film has a polycrystalline structure [105], and is consistent with the FWHM values in the FTIR spectra. This can be explained by the improvement in the crystallinity of the film with better stoichiometry with increasing annealing temperatures [105].

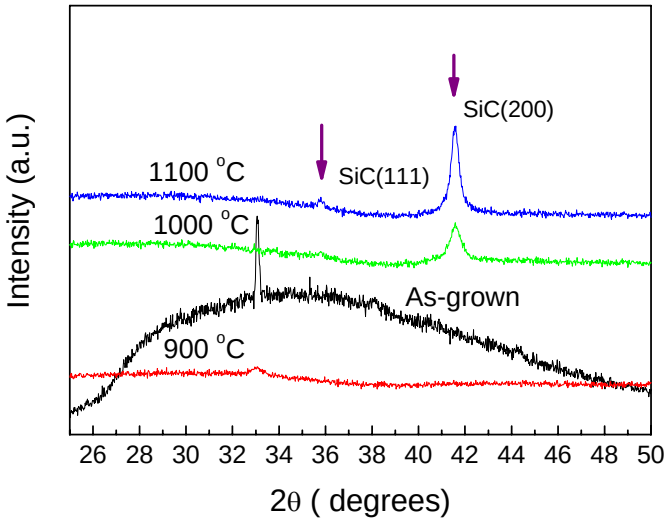

Figure 4.10. XRD spectra of SiC the film as a function of annealing temperature

Furthermore, as it is represented in the Figure 4.10, the FWHM of (200) peak becomes narrower as the temperature is increasing. The crystalline size of the grains is calculated by Scherrer formula. The grain size for the annealed sample at 900 °C and 1000 °C is found to be ~17 and 20 nm, respectively. The strongest peak related to (200) plane is used in grain size calculation. The details of calculations are given in the Table 4. 2.

Table 4.2 Details of the calculated grain size of the SiC nanocrystals

Temperature	Theta (θ)	FWHM	β	cos(θ)	Thickness (nm)
900 °C	20.79	0.48	0.0085	0.935	17
1000 °C	20.79	0.43	0.0075	0.935	20

4.4 Summary and Conclusions

The effects of methane fraction, hydrogen dilution ratio and thermal annealing on the growth of the nanocrystalline SiC films have been investigated by using various diagnostic tools such as FTIR, Raman Spectroscopy, XRD, and optical transmission measurement. The stoichiometric SiC film can be synthesized at methane fraction of $X_c = 0.87$ at substrate temperature of 350 ^oC. Heavy dilution of precursor gases with hydrogen play a crucial role in the transformation from amorphous to polycrystalline phase for $R_H = 20$. The crystallization of amorphous SiC film deposited on Si substrate takes place in the range 900-1100 ^oC. The transition of SiC film from amorphous to polycrystalline phase was monitored by XRD and FTIR measurements. The crystallization of SiC film deposited on Si substrate at low temperature starts at 1000 ^oC. The size of the nanocrystalline SiC is ~ 17 and 19 nm at 1000 ^oC and 1100 ^oC, respectively.

CHAPTER 5

FABRICATION AND CHARACTERIZATION SiC/Si MULTILAYER STRUCTURE BY PECVD

5.1 Introduction

Microcrystalline (μc-Si:H) and amorphous hydrogenated Si (a-Si:H) is a low cost material for photovoltaic devices [121,122]. Most of researches have been focused on the improvement of the optical properties of this material [122,123]. Recently, tandem solar cells based on μc-Si:H and a-Si:H is of great interest for providing cost-effective and efficient photovoltaic devices [124]. It is known that, the solar spectrum can effectively be absorbed by Si nanocrystals with different sizes and band gaps in the same solar cell device, due to quantum confinement effect [16,20]. Moreover, SiC is a good material for solar cell window due to its wide optical band gap [125]. Solar cells based on several layers of amorphous Si:C and nanocrystaline Si surrounded by a-Si:H have different optical properties. Only a few experimental studies of multilayers formed by a-SiC and Si nanocrystals surrounded by a-Si:H have been reported so far [126].

In this chapter, we prepared multilayer films by the PECVD technique, and characterized with major analytical techniques. The results is represented and discussed as a function of process parameters to reach comprehensive understanding of optical, structural and chemical properties of multilayer films.

5.2 Experimental Details

5.2.1 Film Growth

a-SiC:H and a-Si-H films were deposited by the RF PECVD technique with an RF frequency of 13.56 MHz. Electrodes with diameter of 14 cm were kept at a distance of 2 cm. Prior to deposition, the substrates were exposed to the in-situ Argon plasma for 5 min. at 350 ^{o}C with the power 10 W and the pressure 0.5 mbar to get rid of the unwanted contamination. The films were simultaneously deposited on p-type Si (100) wafers and quartz substrate placed on grounded electrode with heater. Films grown on quartz samples were used for transmission and Raman measurements.

5.2.2 Deposition parameters of the in SiC/Si/SiC films

CH_4, SiH_4, and H_2 were used as the precursors to deposit the SiC films. Two set of samples were grown as a sandwich and multilayer structure by the PECVD system. The substrate temperature was kept at 350 ^{o}C, which is low with respect to conventional PECVD method. In all SiC depositions, RF power, gas pressure, and the total gas flow (SiH_4 +CH_4+ H_2) were fixed at the value of 40 W, 2 mbar and 105 sccm, respectively. Also, in all Si layer deposition RF power, gas pressure, and the total gas flow of SiH_4 were kept constant at the value of 10 W, 0.5 mbar and 3 sccm, respectively.

Table 5.1 The deposition parameters of sandwich SiC/Si/SiC structure

	SiC layer				Si layer		Total
Sample ID	Gas SiH_4 (sccm)	Gas CH_4 (sccm)	Gas H_2 (sccm)	Time (s)	Gas SiH_4 (sccm)	Time (s)	Thickness (nm)
29	0.65	4.35	100	360	3	120	150
30	0.65	4.35	100	360	3	30	135
31	0.65	4.35	100	360	3	15	110

In the first set of the sample, thin Si layer between two SiC layers were deposited by PECVD, labeled as a sandwich structure. The only difference of the prepared films is the thickness of the thin Si layer in the sandwich structure. The other deposition parameters are given in Table 5. 1.

For multilayer structures, the layer was deposited on the Si (100) and quartz substrate, followed by Si layer deposition on the a-SiC layer. This process was repeated 10 times to obtain multilayer structures. In the second set of sample, three multilayer structures were deposited by PECVD. The only difference between them is thickness of the Si layer. The details of the deposition parameters are given in Table 5.2.

Table 5.2 The deposition parameters of multilayer SiC/Si/SiC structures

	SiC layer				Si layer		Total
Sample no	Gas SiH_4 (sccm)	Gas CH_4 (sccm)	Gas H_2 (sccm)	Time (s) SiC	Gas SiH_4 (sccm)	Time (s) Si	Thickness (nm)
33	1.3	8.7	150	240	3	120	1320
34	0.65	4.35	100	240	3	20	620
35	0.65	4.35	100	240	3	15	510

Both as-deposited sandwich and multilayer structures were cut into small pieces for thermal treatment. In order to diffuse out the hydrogen from the film, the samples were annealed at 450 ^{o}C for 30 min under vacuum. After that, samples were annealed between 900-1100 ^{o}C for 1 h under vacuum.

5.2.3 Analysis Techniques

The thickness of the as deposited films was measured by Dektak profilometer. FTIR was performed to obtain the information about the chemical structure of the deposited films in the wavenumber range of 400-4000 cm^{-1} with a resolution of 4 cm^{-1}. Raman measurements were performed using a Jobin Jvon Raman Spectrometer equipped with an Argon laser (488 nm) for excitation in the wave number range of 200-2000 cm^{-1}. The crystallinity of the deposited and annealed films was investigated using XRD measurement. 2θ values were maintained between 25° and 50° at 0.02° steps. In order to obtain high-quality TEM images, cross-sectional samples were prepared by the conventional ion-beam thinning method. The presence of nanocrystalline Si in amorhous matrix were observed by TEM in a JEOL 3010 microscope operating in the voltage range of 115-200 kV for different sample.

5.3.1 Characterization of the Si Nanocrystals in SiC/Si/SiC Sandwich Structures

5.3.1.1 FTIR Spectroscopy

FTIR spectra of SiC/Si/SiC sandwich film are shown in Figure 5.1 before and after annealing process. The peak which is commonly attributed to Si-C stretching vibration is located at wave number 762 cm^{-1} for all as-deposited sandwich films (Figure 5.1) [102]. The small shoulder located at around 1000 cm^{-1} is assigned to $SiC-H_n$ vibrations [103]. The peak shape of Si-C band in the as-deposited samples is Gaussian type which indicates the amorphous nature of the as-deposited films [104,113]. It is also seen that the peak corresponded to $Si-H_2$ stretching vibration is located at 2100 cm^{-1} for all as-deposited samples in Figure 5.1. The FTIR intensity of this peak for the as-deposited sample (no: 29) having the highest Si amount is higher than for the sample 30 and 31, while that of Si-C band is almost same for all the as-deposited sandwich film. The decrease in the $Si-H_2$ stretching vibration can be attributed to Si content of the film changing with the thickness of the Si layer of the sandwich film. Thus, the most pronounced SiH_2 vibration is seen in Figure 5.1a) for the sample 29 having the highest Si amount in the film than the sample 30, and 31. Moreover, it couldn't be observed the peaks at around

1250, 1350 and 2890 cm^{-1}, which are related to the $SiC-H_3$ bending and CH_n stretching vibration, respectively [104].

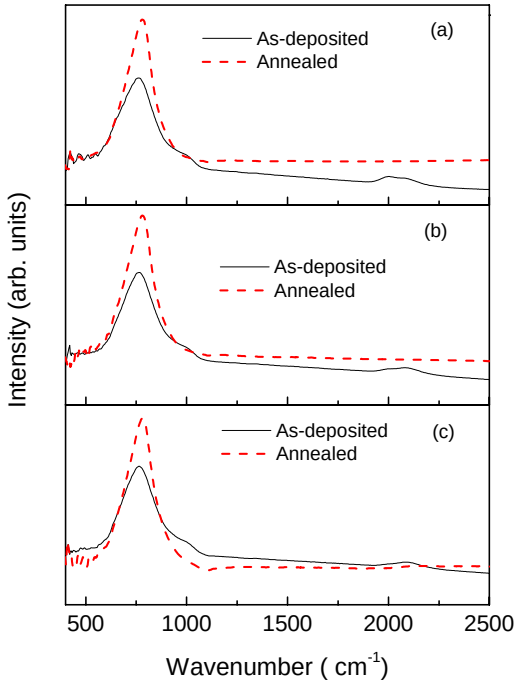

Figure 5.1 FTIR spectra of sandwich structures for the sample numbers of a) 29 b) 30 and c) 31 before and after annealing

Upon annealing, the main SiC peak shifts to 783 cm^{-1} which is the expected value for the SiC film. The intensity of that peak increases significantly at higher annealing temperature as result of increase in the SiC formation. In addition to that the peak width of the FTIR signal gets narrower with the annealing temperature. After the annealing, FWHM of the main infrared vibration mode of annealed samples decreased and peak shape of that is changed from Gaussian type to Gaussian-Lorentzian type which is confirmed by the peak procedure we routinely apply to these results. Gaussian-Lorentzian type indicates more uniform Si-C bond environments. The shift in the peak position indicates that stoichiometry of the film improves, while the decrease in the FWHM of the FTIR

signal is an indication of better uniformity of the film. It is clear that more stoichiometric and uniform SiC layer in the sandwich film were obtained with the annealing process [113]. We see also that the shoulder of the main peak, which is attributed to SiC-H_n vibration, disappears as seen in Figure 5.1 as a result of hydrogen diffusion out of the film.

5.3.1.2 Raman Spectroscopy

Raman spectroscopy is used for assessing the Si-Si and C-C bonds, which are infrared inactive due to absence of the dipole moment. Figure 5.2 shows the Raman spectra of the sample 29, 30 and 31 with annealing temperature. Raman spectra obtained from the samples show no indication of the presence of C-C bonds associate with either G line (sp^2) or D line (sp^3) at 1300 - 1600 cm^{-1}. The absence of these peaks even after very high annealing temperatures ensures that, any of the samples fabricated in this study does not contain any type of C cluster formation [113].

All the as-deposited samples exhibit same spectral features in the Raman spectra (Figure 5.2). SiC in the amorphous phase is known to contribute to the prominent band seen between 400 - 550 cm^{-1} which related to LA mode of Si-C bonds [113,120].

Upon annealing at 900 ^oC, the pronounced peak related with Si-Si bonds in crystalline silicon at ~520 cm^{-1} were observed in the Raman spectra of the sample 29 (Figure 5.2 (a)) [107,127]. The strong asymmetry seen in the Raman peak is an indication of the formation of the nanocrystal with varying size [19]. This result is good evidence for Si nanocrystal formation occurred after the annealing treatment. As expected, the intensity of this signal depends on the amount of Si in the film as shown in Figure 5.2.

As seen in Figure 5.2(b), sample 30 with the least amount of Si exhibits a weak Si-Si signal after the annealing. Sample 31 shows the amorphous characteristic

with the band at ~470 cm^{-1} even at high temperature annealing in Figure 5.2(c). These are in agreement with FTIR results.

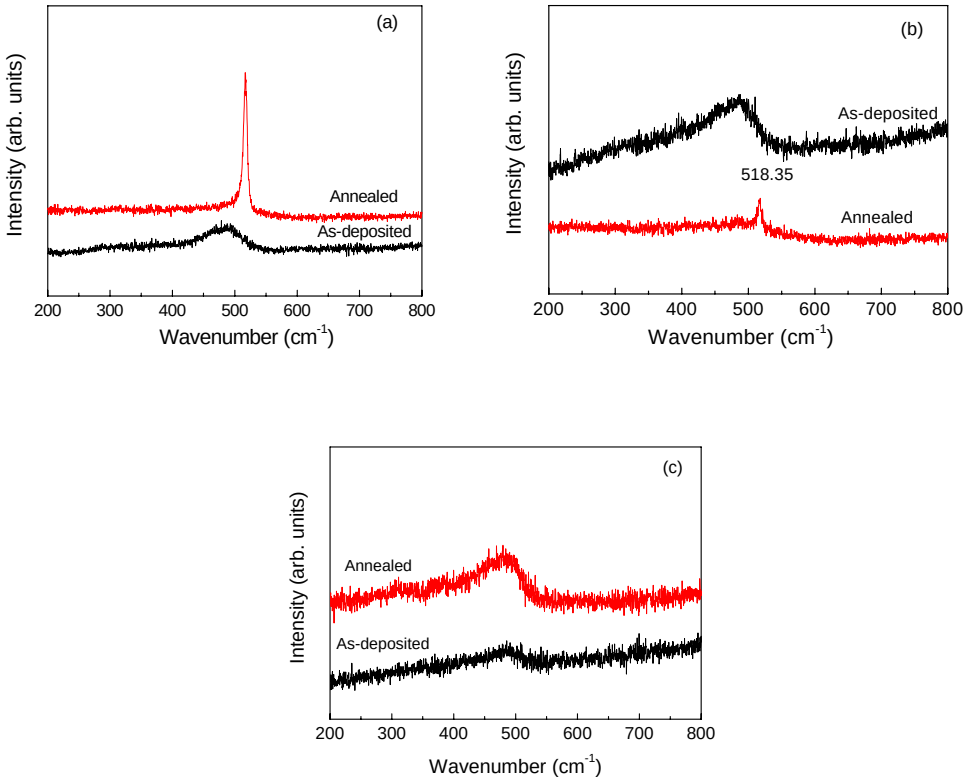

Figure 5.2 Raman spectra of sandwich structures for the sample numbers of a) 29 b) 30 and c) 31 before and after annealing

5.3.1.3 X-Ray Diffraction

XRD measurements are used to investigate the evolution of the crystalline phase of Si in the studied sandwich film. We observed no XRD signal which can be related to the crystalline phase of SiC (α-SiC and β-SiC) before and after the annealing process. This shows that SiC film is amorphous, and the annealing temperature is too low for the crystallization of the film. In agreement with the FTIR and Raman data, this implies that the SiC film has an amorphous structure with or without Si nanocrystalline structure. Moreover, the scattering related with (111) plane of Si is not observed in the as-deposited sample.

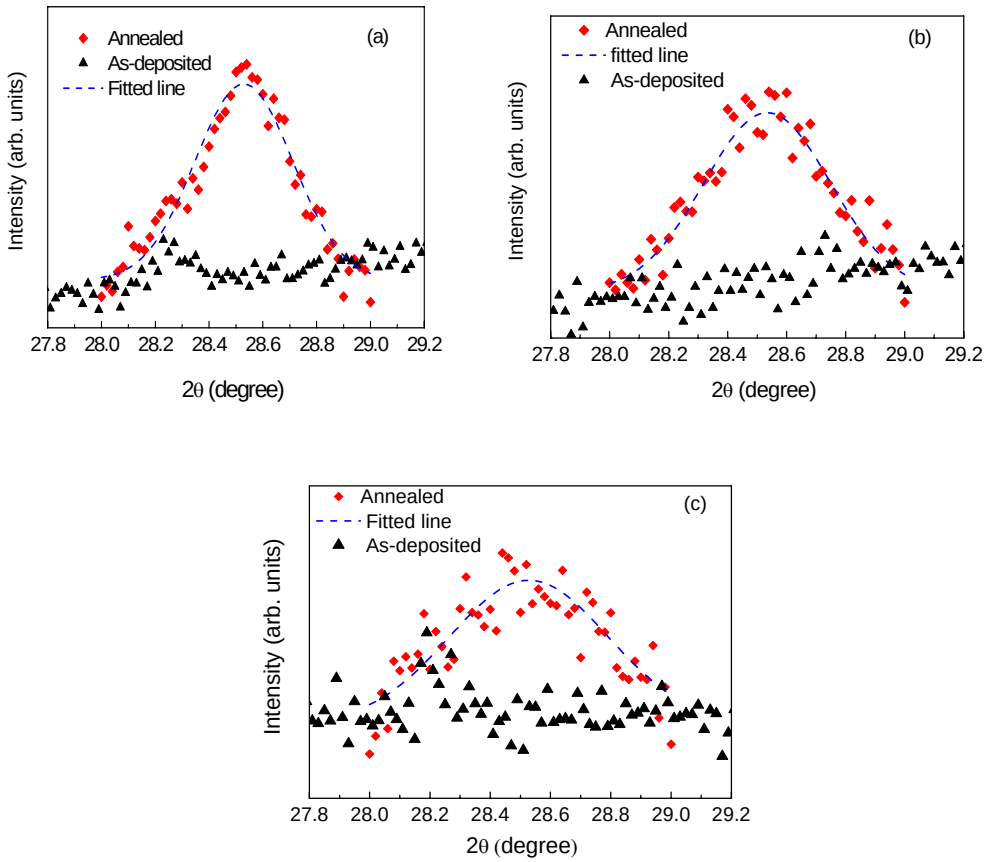

Figure 5.3 XRD peak fits around 2θ=28.5° for the sample numbers of a) 29 b) 30 and c) 31 before and after annealing

After the annealing process, Si (111) related peaks are emerged in the XRD spectra of the all samples (Figure 5.3). The scattering related with (111) plane of Si is detected at 2θ=28.53° [128] in the annealed samples. This indicates that the Si atoms have formed nanocrystals after the annealing treatment. The FWHM of the XRD scattering peak related with (111) plane of Si increased with decreasing Si amount in the sandwich structure, this depends on the thickness of the Si layer in the film as well as size distribution of the Si nanocrystals.

A fitting process was employed to calculate size of the nanocrystals for the samples containing different Si amount. The crystalline size of the grains was calculated by Scherrer's formula [129]. The results of the grain size in annealed

sample at 900 ^{o}C is found to be about 16, 14, and 11 nm for the sample numbers 29, 30, and 31, respectively. As we can anticipate, the size of the nanocrystals depended on the amount of the Si in the multilayer structure. The details of calculations are given in the Table 5.3.

Table 5.3. The details of the grain size calculations using Scherrer's formula

Sample no	Theta (θ)	FWHM	β	cos(θ)	Thickness (nm)
29	14.27	0.48	0.0084	0.9691	16
30	14.27	0.58	0.0100	0.9691	14
31	14.27	0.73	0.0126	0.9691	11

5.3.1.4 TEM

The structure of the SiC/Si/SiC sandwich films on silicon substrate was investigated by cross-sectional TEM observation in order to image the nanocrystals directly. It is seen in Figure 5.4 that some crystal phases formed in the Si layer of the sandwich structure. It is understood from the dark field TEM image of the sample 30 that SiC layer is amorphous, while the Si layer is polycrystalline.

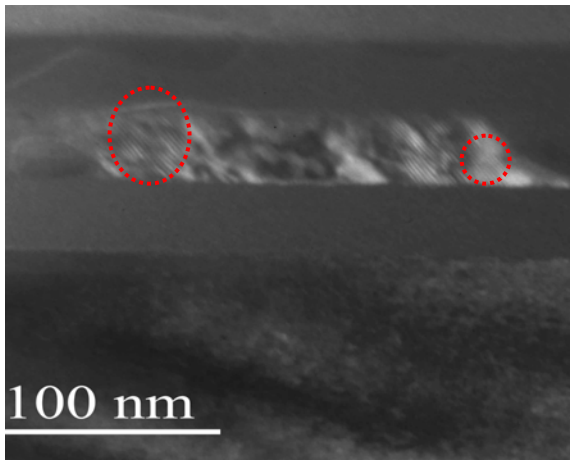

Figure 5.4 TEM cross-sectional image of SiC/Si/SiC layer of the sample 30 after annealing

While a large grain of the polycrystalline Si film is bright, as well as the Si substrate, there are no bright spots in the amorphous SiC layer. Therefore, there are no Si or SiC crystals or any crystalline phases in this a-SiC layer. Si nanocrystals only exist in the Si layer of the sandwich structure. The size of the Si nanocrystals was limited by the amorphous SiC layer. The thickness of the each amorphous SiC layer is about 40 nm.

5.3.2 Characterization of the Si Nanocrystals in SiC/Si/SiC Multilayer Structures

5.3.2.1 FTIR Spectroscopy

Figure 5.5 shows the FTIR spectra of the multilayer structure for the sample numbers of 33, 34 and 35 before and after annealing. The same spectral features were detected by FTIR in all samples fabricated in this study (Figure 5.5 (a,b and c)). Three infrared vibrations were observed for the as-deposited multilayer sample 33 at 753, 975 and 2100 cm^{-1} corresponded to Si-C, SiC-H_n and Si-H_2 stretching vibrations [99,119], respectively (Figure 5.5).

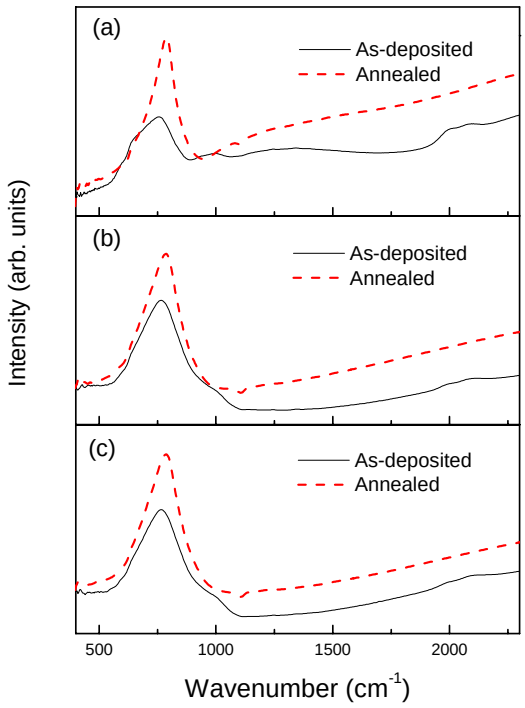

Figure 5.5 FTIR spectra of multilayer structures for the sample numbers of a) 33 b) 34 and c) 35 before and after annealing

After the annealing process, Si-C stretching vibration is shifted to 785 cm^{-1}, and FWHM of this vibration is decreased. The peak shape of this vibration is changed from the Gaussian type (confirmed by peak fitting), which is consistent with the amorphous nature of the as-deposited films, to Gaussian-Lorentzian type. These results clearly indicate that the annealed multilayer films have better uniformity and stoichiometry. Moreover, SiC-H_n and Si-H_2 stretching vibrations disappeared in the spectra after the annealing, due to hydrogen diffusion out from the multilayer film.

5.3.2.2 Raman Spectroscopy

Figure 5.6 represents the Raman spectra of the multilayer film for the sample numbers of 33, 34 and 35 before and after the annealing. All samples exhibit the same spectral features. Before the annealing, they show the prominent band at about 470 cm^{-1} associated with LA mode of Si-C. This scattering is usually observed in amorphous SiC with or without very small size crystalline regions in the film [120]. It is hard to see any graphite related vibrations, which could be observed by Raman peaks at 1330 and 1600 cm^{-1} related with the G line and D line in all spectra of any of the samples.

After the annealing, there are two vibration modes recognized in these spectra (Figure 5.6). The pronounced peak seen at 506 cm^{-1} is attributed to Si vibration in crystalline phase, which is almost the same for all the samples with different amount of Si in the multilayer film [19]. The strong asymmetry seen in the main Raman signal is a result of the size distribution of nanocrystals [16]. We see also that the intensity of the peak depends on the amount of Si atoms in the multilayer films.

As seen from Figure 5.6(c), sample 35 with the least amount of Si in the multilayer film exhibits a lower intensity in the Si-Si signal after annealing. For sample number of 33 with maximum Si content, the Si-Si Raman signal strength is high. Sample 34 exhibits an intermediate signal strength as expected. In addition to that the new weak peak which is observed at 960 cm^{-1} can be assigned to second order Si phonons [105,127]. Moreover, we have not detected the peak

related with C-C bonds G line (sp^2) and D line (sp^3) at 1335 and 1600 cm^{-1}, indicating no evidence of carbon cluster formation with the annealing.

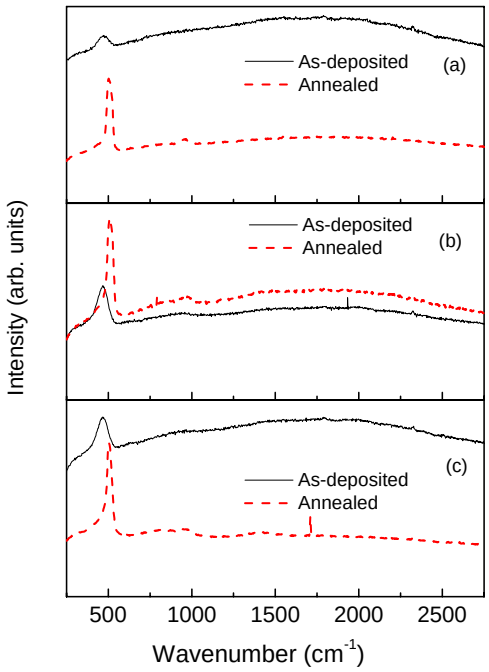

Figure 5.6 Raman spectra of multilayer structures for the sample numbers of a) 33 b) 34 and c) 35 before and after annealing

5.3.2.3 X-Ray Diffraction

Figure 5.7 displays the XRD spectra of multilayer structures for the sample numbers of 33, 34 and 35 before and after annealing. As explained above, absence of crystalline phase implies that SiC layer of the multilayer structures is amorphous as expected at low annealing temperatures used in this study. Moreover, the scattering related with (111) plane of Si was not observed in the as-deposited sample.

After the annealing process, Si (111) related peaks are clearly observable in the XRD spectra of the all sample (Figure 5.7 a, b and c). The scattering related with (111) plane of Si is detected at $2\theta = 28.53^{o}$ [126] in the samples annealed at 900 ^{o}C, for 1h under the vacuum. This indicates the formation of the nanocrystals after

the annealing process. The FWHM of the XRD scattering peak related with (111) plane of Si increased with decreasing Si amount in the multilayer film.

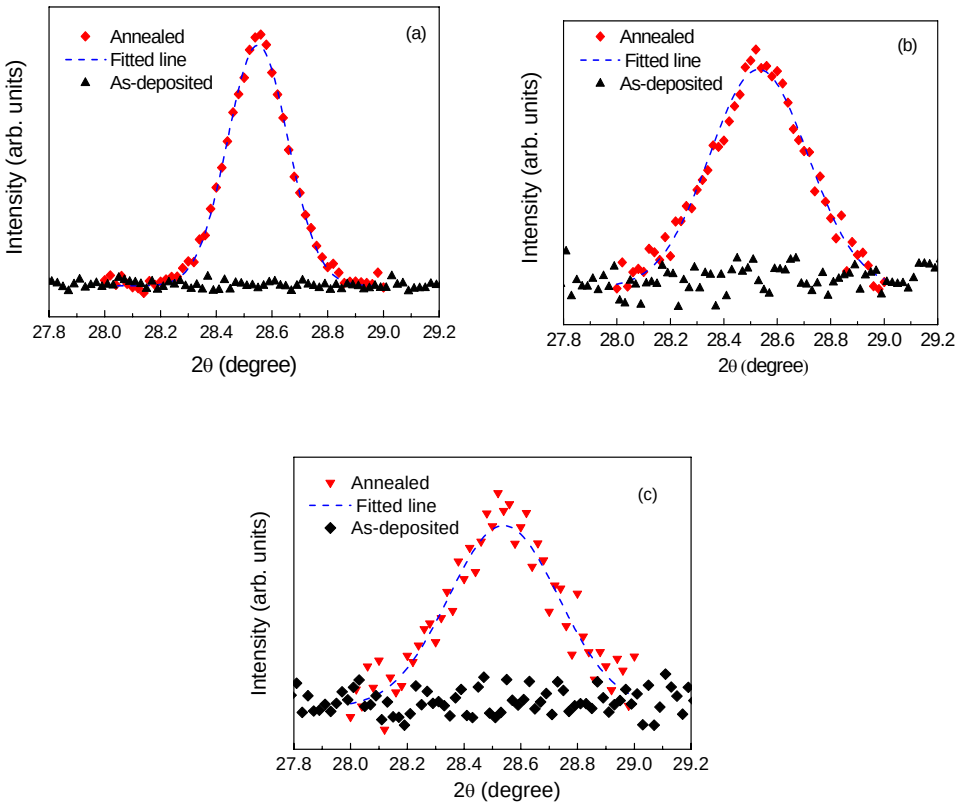

Figure 5.7 XRD peak fits around 2θ=28.5 ^{o} multilayer structures for the sample numbers of a) 29 b) 30 and c) 31 before and after annealing

5.3.2.4 TEM

Finally, we performed the TEM analysis of the multilayer sample numbers of 33, 34 and 35 annealed at 900 ^{o}C in order to observe the presence of Si nanocrystals directly. Figure 5.8 shows a typical cross-sectional TEM image of the multilayer 33 as an overview at low magnification after the annealing. It is seen only first few layer of the multilayer film, because the multilayer film is cracked during the sample preparation. It is seen in Figure 5.8 that some crystal phases formed in the Si layer. It is understood from the TEM image of the multilayer sample number of

33 that SiC layer is amorphous, and homogenous. There are no crystalline grains in SiC layer, while the Si layer is polycrystalline.

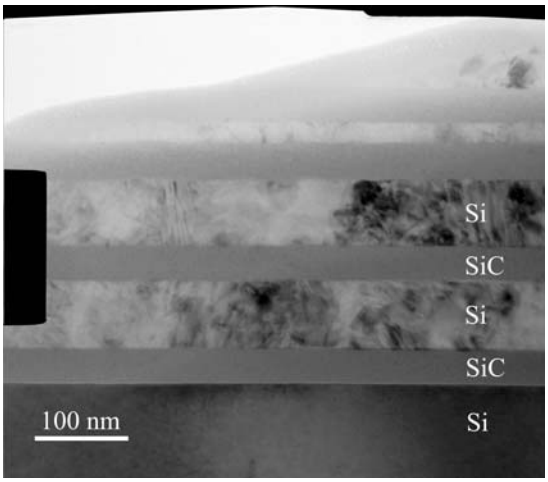

Figure 5.8 TEM cross-sectional image of multilayer film for the sample number 33 after annealing

Figure 5.9 displays the TEM cross-sectional images of multilayer film 34 with two different magnifications after annealing. We see all SiC /Si layers of the film 34 in Figure 5.9(a). The successive SiC and Si layer of the multilayer sample 34 is clearly seen in the Figure 5.9. The thickness of the one cycle (SiC+Si layer) is approximately 50 nm. Nanocrystalline Si structures can be seen the in the Si layer of the multilayer film. We observe no crystalline structure in the SiC layer of the multilayer film (Figure 5.9). Therefore, Si layer has the polycrystalline structure, while the SiC has a homogenous amorphous structure in the multilayer film.

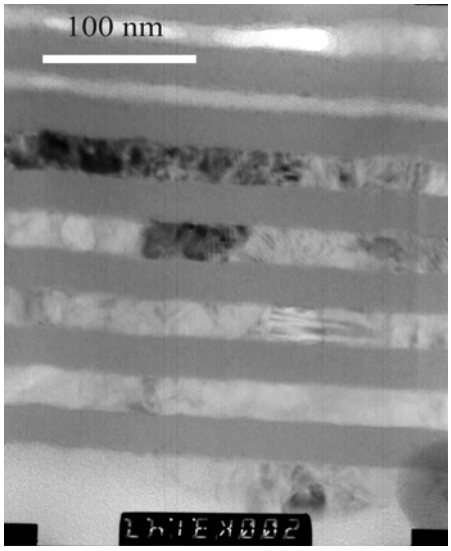

Figure 5.9 TEM cross-sectional image of the multilayer structure for the sample number of 34 after annealing

Figure 5.10 shows the TEM cross-sectional images of multilayer film 35 with two different magnifications after annealing. The sample exhibits the same features as the sample 34 except that the thickness of the multilayer film is different. It is also seen the successive 10 cycle SiC /Si layer of the film 35 in Figure 5.10(a). The thickness of one layer period (SiC+Si layer) is approximately 45 nm.

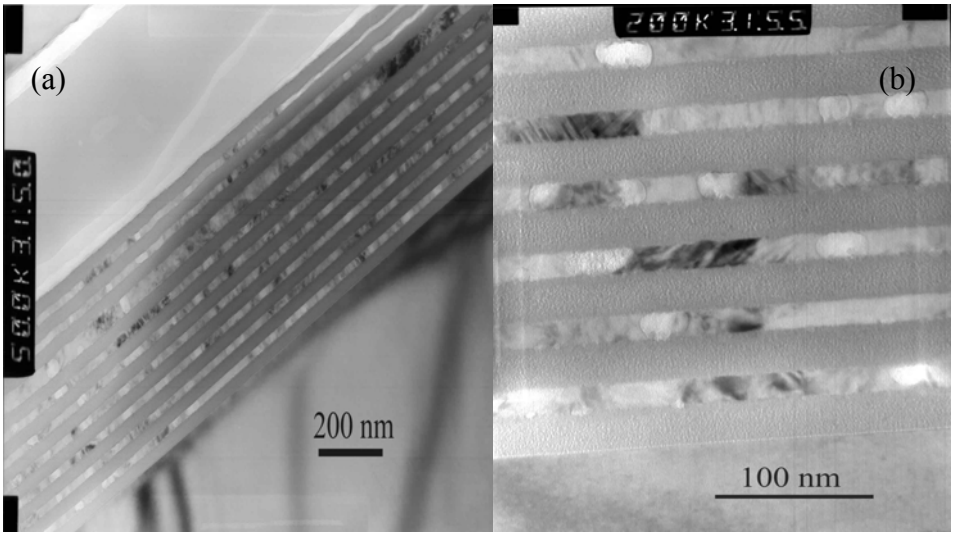

Figure 5.10. TEM cross-sectional images with the magnification of a) 500 kV b) 200 kV for multilayer sample 35 after annealing

5.4. Summary and Conclusion

The amorphous silicon carbide and silicon films were deposited on silicon and quartz substrate. Structural and optical properties of the films were studied before and after annealing. The aim of this part of this work was to fabricate multilayers of Si:SiC structure for device applications.

We have employed various characterization techniques to understand the structural and chemical properties of the fabricated films. The stretching vibration of Si-C bond monitored to see if stoichiometric and uniform structures are formed all fabricated films. As expected after the annealing, the intensity of this signal increased, while its FWHM decreased as a result of better uniformity and stoichiometry. The annealing has also induced Si crystallization as evidenced from Raman measurements. The intensity of the Si Raman signal increased with the increasing the Si content of both types the film. Si crystallization was also evidenced by XRD measurements which were performed to detect the diffraction peak from the Si (111) plane. XRD signal resulted from the (111) plane of Si nanocrystal was clearly seen in the spectra both sandwiched and multilayer films. The presence of the Si nanocrystal is also observed with the TEM techniques.

As a conclusion, it is shown in this study that amorphous SiC/crystalline Si films can be fabricated with good structural and chemical uniformity by the PECVD technique.

CHAPTER 6

SYNTHESIZING OF AMORPHOUS SiC MATRIX PREPARED BY MAGNETRON SPUTTERING

6.1 Introduction

SiC is an important semiconductor material both in crystalline and in amorphous form for various electro-optical devices such as high power transistors and solar cells [23,130]. Crystalline silicon carbide has high thermal conductivity (~3.9 W/cm per ^{o}C), high electric breakdown field (~4x10^{6} V/cm), high thermal stability (melting point 2730 ^{o}C) and a saturation drift velocity (~2x10^{7} cm/s) due to its large optical band gap (>2 eV) [16,131-134].

SiC thin films are commonly prepared by several methods such as plasma enhanced chemical vapor deposition [135], ion implantation [83,136], thermal evaporation [137] and magnetron sputtering [138-140]. It is known that chemical composition, optical and structural properties of the film depend on the deposition parameters [101].

Mahmood et al. reported that native oxide of the SiC film, which is prepared by reactive magnetron sputtering, is suitable the insulating gate material in MOS devices [101]. Li and coworkers have deposited ultra thin SiC films on Si by rapid thermal chemical vapor deposition [141]. The FTIR spectroscopy of the SiC films shows the characteristic Si-C absorption peak ~800 cm^{-1}. X-ray and electron diffraction measurements indicate monocrystalline structure in these SiC films. Prado et al. investigated the improvements on chemical and structural order of amorphous hydroganeted silicon carbide thin films deposited by PECVD. The RF

power and hydrogen dilution of the gas mixture were optimized to obtain better stoichiometry of the film [114].

In this chapter, fabrication and characterization of Si nanocrystals (Si-nc) in an amorphous SiC matrix using magnetron co-sputtering are presented.

6.2 Experimental Details

6.2.1 Film growth

SiC thin films were deposited on Si (100) and quartz substrate by sputtering single SiC target in Argon ambient at room temperature. Si rich SiC (Si:SiC) thin films were deposited by co-sputtering high purity Si and SiC targets by using DC and RF sources, respectively.

6.2.2 Deposition Parameters of SiC film

Prior to deposition of the films, quartz and n-type silicon substrate with (100) orientation were cleaned by using a standard cleaning procedure in clean room conditions. In order to remove residual contamination and water molecules, samples were heated in the sputtering chamber at 500^{o}C for 20 minutes just after loading into the vacuum chamber. The RF power of SiC target was fixed at 350W and Si concentration of film was controlled with DC power (100W) during the deposition. Argon pressure was fixed at 3 mTorr during the deposition. The details of the deposition parameters are given in Table 6.1.

Table 6.1 Deposition parameters of the films

	Gas Flow (sccm)	RF Power (Watt)	DC Power (Watt)	Deposition Time (min)	Deposition Rate (nm/h)	Thickness (nm)
SiC	50	350	---	150	69	192
Si:SiC	50	350	100	150	125	312

SiC and Si:SiC films deposited on silicon and quartz substrate were cut into small pieces and annealed in a fused quartz furnace at 1100 ^{o}C temperature under nitrogen atmosphere for 60 and 180 min, respectively.

6.2.3 Analysis Techniques

The thickness of the film was measured by scanning electron microscopy (SEM). FTIR measurements were performed with resolution 3 cm^{-1} to observe vibrational modes of SiC at a normal incidence. XRD measurements were done with a standard X-ray powder diffractometer. 2θ values were taken between 30° and 70° at 0.02° steps. Backscattering Raman measurements were performed to detect Si-Si vibrational bonds. XPS was used for examining the chemical bonding state and the composition of the films. Qualitative energy dispersive X-ray (EDX) measurements were performed to investigate the chemical composition of the SiC and Si:SiC films. Images were obtained using a Fei-Quanta 400 SEM system. Optical absorption measurements were done between the ranges of 200-800 nm using in Perkin-Elmer (λ35) double-beamed spectrometer to estimate the optical band gap of the films.

6.3. Results and Discussions

6.3.1. FTIR Spectroscopy

The FTIR absorption spectra were performed to obtain the information about the chemical bonding in the sputtering films. Figure 6.1 shows FTIR spectra of SiC and Si rich SiC thin film with annealing temperature. The peak related with the Si-C stretching vibration is located at wave number ~765 and 745 cm^{-1} for as-deposited samples of SiC and Si rich SiC film, respectively [114,118,141]. After the annealing process, they shift to the higher wave number at ~798 cm^{-1}, which indicates the formation of more stoichiometric SiC [113,142]. Intensity of these peaks significantly increases with annealing temperature. We see also that an additional peak located at ~1080 cm^{-1} which corresponds to stretching vibration of Si-O-Si bonds. The intensity of this peak gradually increases with the annealing temperature, indicating that the samples are slightly oxidized during the annealing process due to lack of purity of the nitrogen gas.

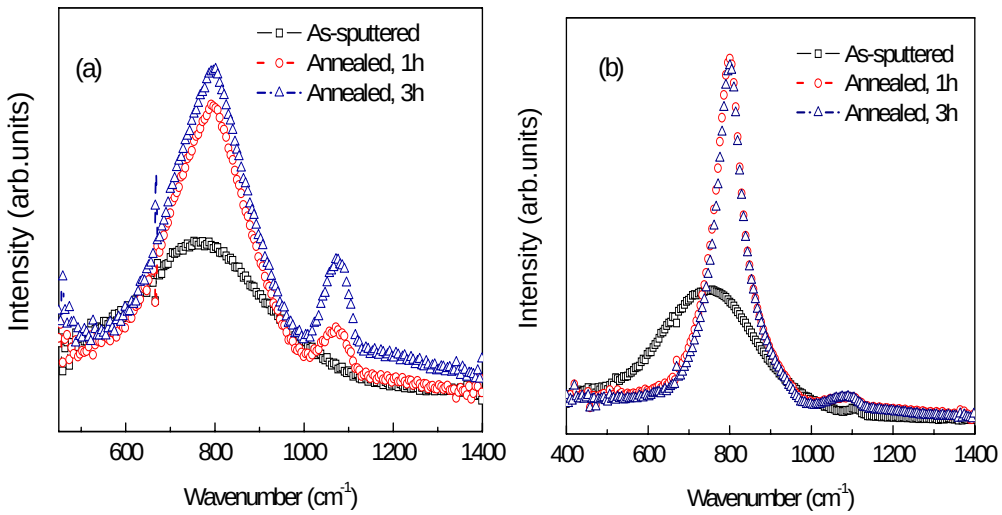

Figure 6.1. FTIR spectra of a) SiC films b) Si rich SiC film before and after the annealing

The line shape of the as-deposited samples is Gaussian type which points to the amorphous nature of the films, even tough that of annealed ones is Gaussian-Lorentzian type which is consistent with more uniform Si-C bond environments [113]. We see also that the peak width of the samples having excess Si is narrower than the sample having no excess Si. In order to see evolution of the film clearly, the peak position and the FWHM of the Si-C absorption bands are plotted as a function of annealing temperature in Figure 6.2(a) and (b).

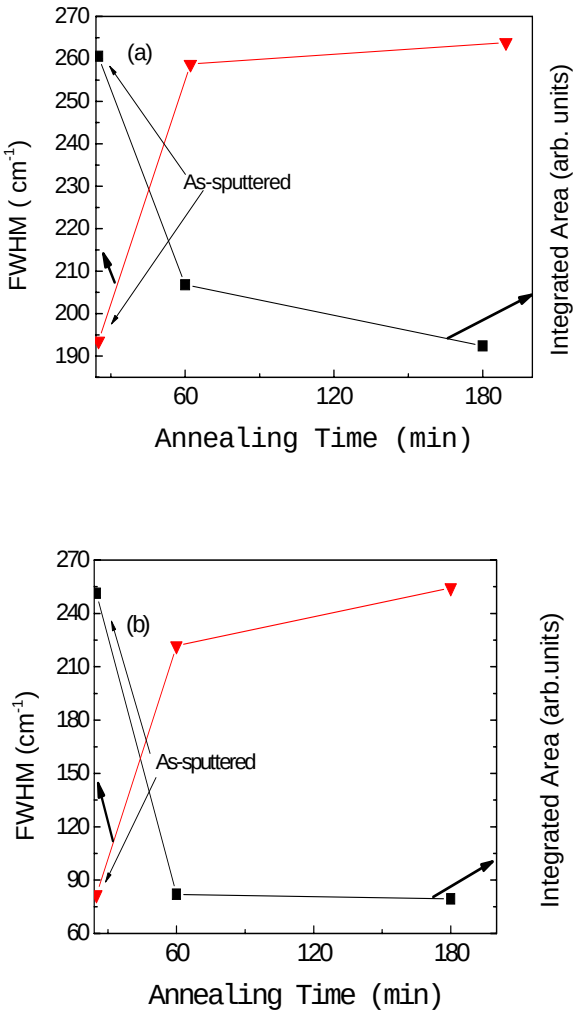

Figure 6.2. The variation of the FWHM and integrated area of SiC peak for a) SiC b) Si rich SiC film with annealing time

As shown in the Figure 6.2, FWHM of Si-C peak decreases from 260 to 192 cm^{-1}, whereas the integrated area of that peak increases from 20 to 39 arb. units with the annealing temperature for SiC film. The sample having the intentional excess Si exhibits drastic difference in the variation of FWHM whose value dropped from 251 to 79 cm^{-1}, whereas the integrated area of that peak increased from 60 to 77 arb. units with the annealing temperature for Si rich SiC film. These changes in the FWHM of the FTIR signal indicate a variation towards better uniformity in the film [113,143,144]. The uniformity of the Si rich SiC film appears to be better

than the sample having no excess Si. It can be stated that we obtained more stoichiometric and uniform SiC films after the annealing [144].

6.3.2. Raman Spectroscopy

Figure 6.3 shows the Raman spectra of the SiC films before and after the annealing. Raman spectra obtained from the sample show no indication of the presence of the Si-Si bond which is typically observed at ~521 cm^{-1} [113,142]. The absence of this peak indicates that, this sample does not contain any Si cluster formation. The broad band seen between 350 and 500 cm^{-1} is attributed to amorphous SiC phase [120].

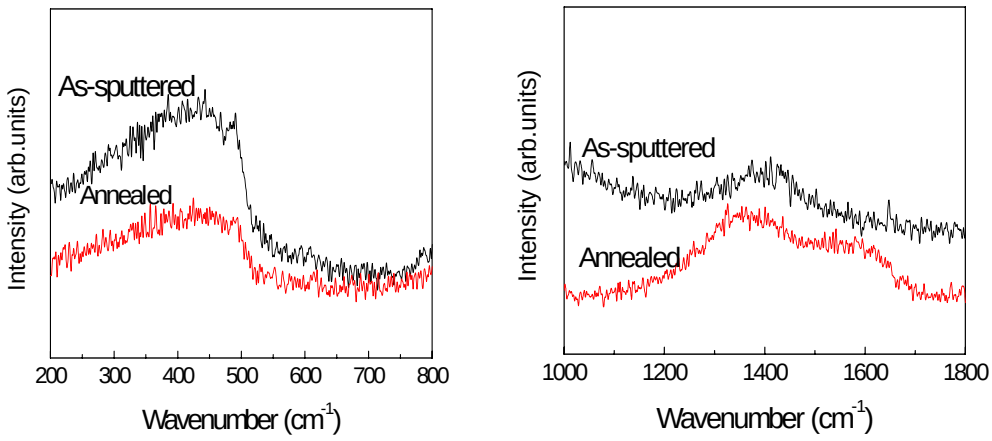

Figure 6.3. The Raman spectra of SiC film before and after the annealing

We also observe another peak between 1300-1600 cm^{-1} which is commonly assigned to C-C bonds in the amorphous carbon [112,113] . Upon annealing at 1100 ^{o}C, this peak clearly splits into two subbands at 1335 and 1600 cm^{-1} associated with C-C bonds G line (sp^2) and D line (sp^3). This indicates that the carbon cluster is formed at higher annealing temperatures.

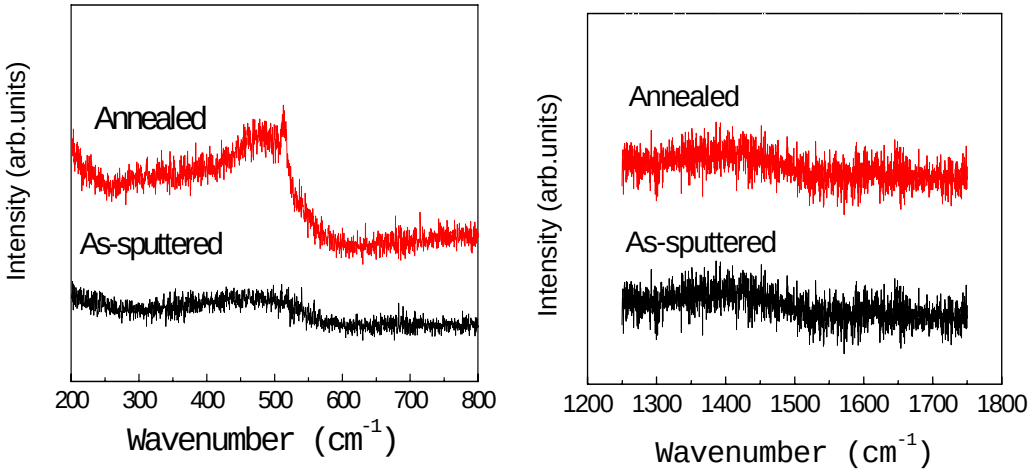

Figure 6.4. The Raman spectra of Si rich SiC film before and after the annealing

Figure 6.4 shows the Raman spectra of the Si rich SiC films before and after the annealing. The Raman spectra obtained from the as-deposited sample of SiC film with and without excess Si show the same spectral feature. The broad band is seen between 350 and 600 cm^{-1}, which is attributed to SiC bond in the amorphous phase. However, the main contribution to the Raman signal in this range is from amorphous Si especially for the sample having excess Si. It is well-known that amorphous Si generates an asymmetric Raman peak resulting from transverse optical modes of oscillations [145,146]. We have not observed the peak which is assigned to C-C bonds D line (sp^2) and G line (sp^3) at ~1300-1600 cm^{-1} in the Raman spectra of the Si rich SiC film even after high temperature annealing. This is good evidence that the sample having the intentional excess Si does not contain C cluster formation. We also see a very small peak at 517 cm^{-1} associated with Si-Si bonds in crystalline silicon at 517 cm^{-1} in Raman spectrum of the Si rich SiC film after the annealing [127]. The asymmetry seen in this Raman signal is attributed to size distribution of the nanocrystals [19].

6.3.3. X-Ray Photoelectron Spectroscopy

XPS analysis of the samples was performed to examine the chemical structure of the deposited films. Before the analysis, the surface layer of the films was sputtered with Ar^+ beam having the acceleration voltage 2000 V in order to

remove the undesired surface contamination caused by the direct contact with air prior to loading the samples into UHV chamber. The peaks of O 1*s*, C 1*s*, and Si 2*p* states were observed in the XPS spectra of all studied samples. The presence of the O 1*s* peak can be attributed to the surface oxidation of the film during the annealing process. Figure 6.5 shows the XPS spectra for SiC and Si rich SiC films before and after the annealing. For as-deposited SiC and Si:SiC films, O 1*s* binding energy peak was measured to be at 532.6 and 532.3 eV, respectively [101]. After the annealing treatment, the intensity of the O 1*s* peak increased, and the peak position shifted to 533.3 and 534.9 eV for SiC and Si:SiC, respectively. These results indicate that some oxygen atoms have diffused into the film and Si-O-C bonds have formed, resulting in the shift of the O 1*s* in XPS spectra. This would support the interpretation of the AS vibration of Si-O bonds located at 1080 cm^{-1} in FTIR measurements.

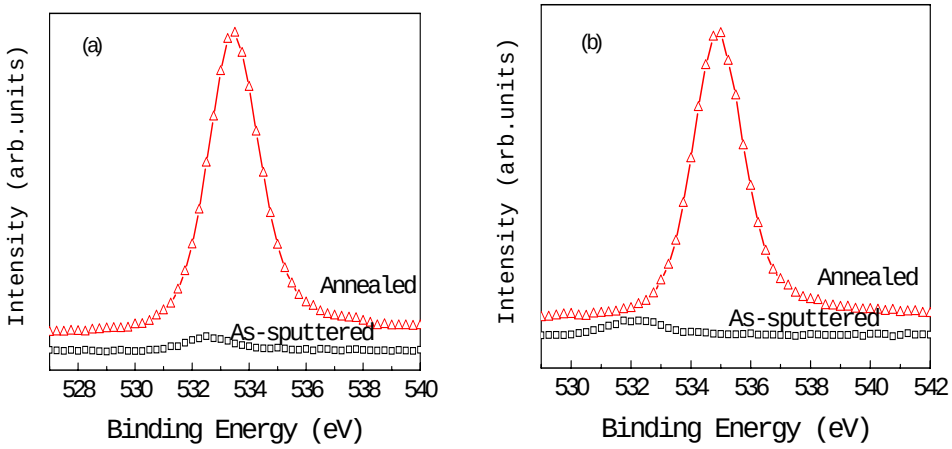

Figure 6.5. O 1*s* XPS spectra of the a) SiC film and b) Si rich SiC film before and after annealing

Figure 6.6 displays C 1*s* XPS spectra of the SiC and Si rich SiC film before the annealing process. For the as-deposited SiC and Si:SiC film, C 1*s* was centered at 284.4 and 283.3 eV, respectively. Since C 1*s* peak is commonly measured at 284.5 eV for C-C bonds, this shift towards lower binding energy value is an indication of C-Si bond formation [118]. For C 1*s* spectrum of the SiC film, the deconvoluted peaks at 284.4 and 286.5 eV are related to C-Si and C-C bonds,

respectively [147]. The presence of the C-C bond has also been confirmed by the graphite signal observed in the Raman spectroscopy.

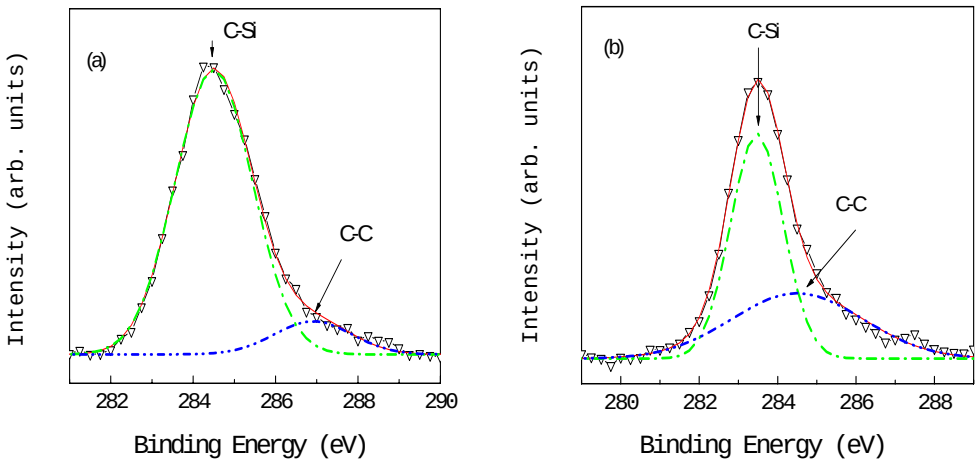

Figure 6.6. C 1*s* XPS spectra of a) SiC b) Si rich SiC film before annealing

Figure 6.6 b) shows that, for C 1*s* spectrum of the Si rich SiC sample, this peak significantly shift towards the SiC phase up to 283.3 eV [134]. The deconvoluted peaks at binding energy of 283.4 and 284.6 eV were attributed to C-Si and C-C bonds [147]. It can be noted that for the SiC film without any excess Si, some of the carbon atoms are in graphite phase, and some of them forms SiC phase, while for the Si rich SiC sample, the additional Si atoms are either bonded to carbon atoms or precipitated as Si nanocrystals.

After the annealing, the carbon intensity is too weak to allow reliable analysis of SiC and Si rich SiC films. The possible reason of that can be formation of the CO that leaves the surface in the gas form after the annealing process.

The XPS Si 2*p* spectrum is seen in Figure 6.7 for the SiC and Si rich SiC samples before and after the annealing. For as-sputtered SiC film, deconvoluted Si 2*p* XPS signal, located at 101.2 and 102.1 eV [118] corresponds to the Si-C and O-Si-C bonds (Figure 6.7(a)). The XPS Si 2*p* spectra of the sample Si:SiC film is seen in Figure 6.7(b). Before the annealing process, Si 2*p* deconvoluted XPS peaks

centered at 100.8 and 101.9 eV [118], were related to formation of Si-C and O-Si-C bonds in Figure 6.7(b).

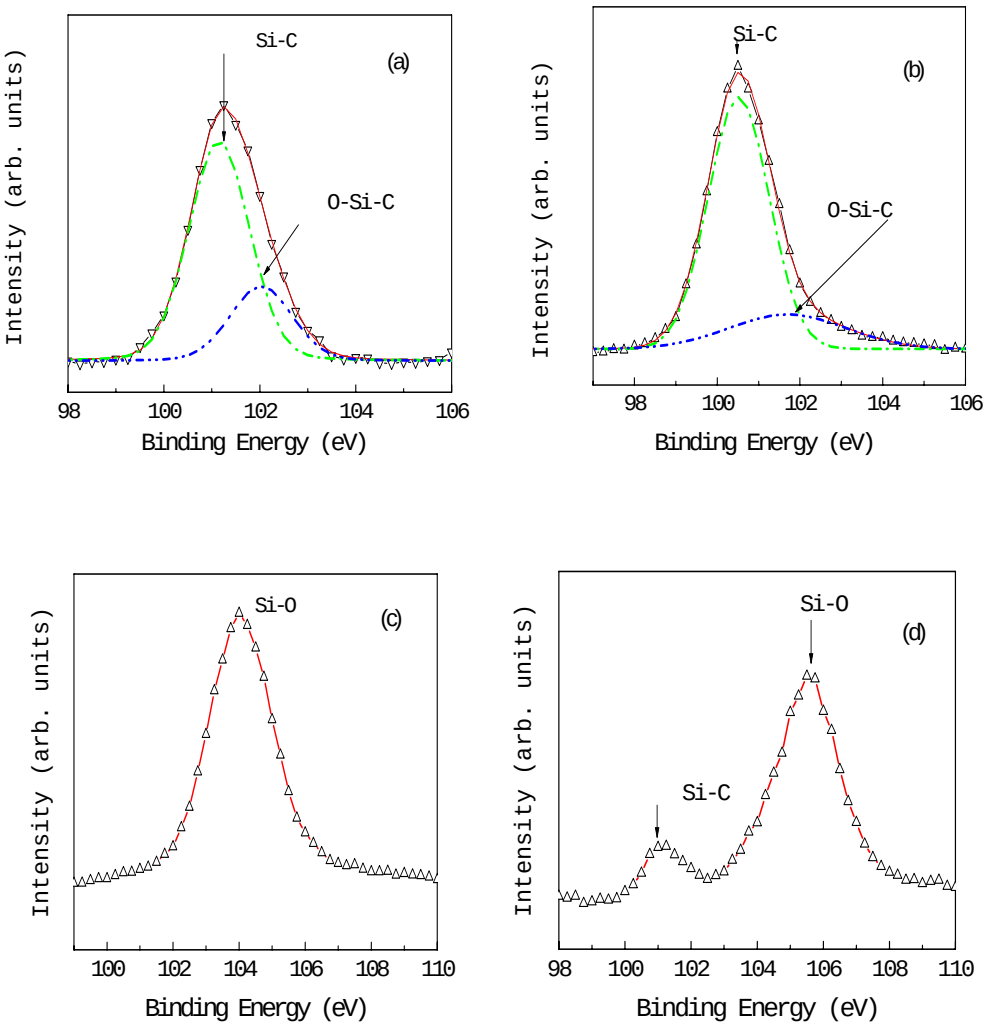

Figure 6.7. Si 2*p* XPS spectra of the samples of SiC film a) before and c) after annealing and Si 2*p* XPS spectra of the samples of Si:SiC film b) before and d) after annealing

Upon annealing, this peak shifts to the higher bonding energy up to ~104.1 eV, which is related to Si-O bonds in the SiO_2 phase as shown in Figure 6.7(c) [101]. For Si rich SiC films, this peak splits into two subbands which are located 101.0 and 105.6 eV corresponding to Si-C and Si-O bonds, respectively (Figure 6.7(d)).

This can be explained that Si atoms at the top few layers of the film can be oxidized during the annealing process [114,148]. It is known that there are 4 oxidation states of Si atom, associated with the number of oxygen in the network of Si [147,148]. The higher oxidation states cause a shift towards higher binding energy values.

6.3.4. Energy Dispersive X-Ray Analysis

The qualitative EDX measurements were performed to investigate the chemical composition of the deposited films. EDX analysis of SiC films yielded silicon, oxygen, carbon related peaks before and after annealing shown in the Figure 6.8. From this analysis we see that oxygen concentration of the SiC and Si rich SiC films increased after the annealing. This is in agreement with FTIR and XPS results. The relative quantitative concentrations of the elements in the SiC and Si rich SiC films are given in the Table 6.2. It can be interpreted from the relative concentrations of the elements in the films that the SiC films have high carbon concentration with the sensitivity factor of the EDX system.

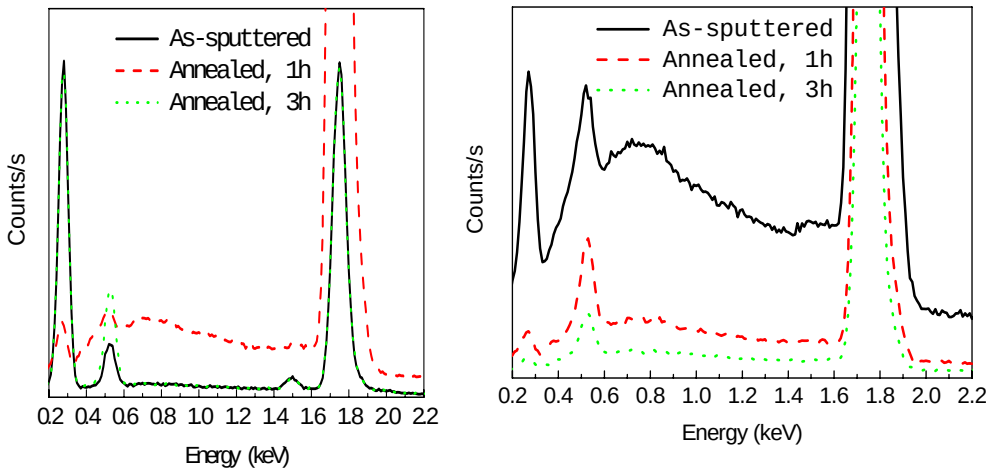

Figure 6.8 The qualitative EDX spectra of as-deposited and annealed a)SiC b)Si rich SiC films

After the annealing of the SiC films, some of the carbon atoms formed CO or CO_2 and left the sample, resulting in the reduction of the carbon concentration in the

films as also reported by others [119,149,150]. Also some of the oxygen atoms available in the annealing environment created Si-O bonds, giving rise to concentration of oxygen atoms.

Relative silicon concentration in the Si rich SiC films after and before annealing is higher than SiC films, as it is expected. On the other hand, the silicon concentration is much higher than what we would expect from these samples. One possible explanation for this result might be related to the detection limits of C atoms. EDX is not a very reliable technique for the detection of C atoms. Raman results given in Figure 6.4 do not indicate any Si-Si formation in these samples before the annealing. It is clear that a thin film with 92 % Si content would have generated a good Raman signal. For this reason the quantitave values obtained from EDX analysis may not represent the actual values.

Table 6.2. Relative quantitative concentration of Si, O, C elements in the SiC and Si rich SiC films before and after annealing

	Carbon	**Oxygen**	**Silicon**
SiC, as-sputtered	64 ± 1	4 ± 1	32 ± 1
SiC, annealed	61± 1	8 ± 1	31 ± 1
Si:SiC, as-sputtered	7 ± 1	1 ± 1	92 ± 1
Si:SiC, annealed	3 ± 1	3 ± 1	94 ± 1

6.3.5. Scanning Electron Microscopy

The surface topology of the films before and after annealing was investigated with SEM at 30 keV e-beam energy. Figure 6.9 and Figure 6.10 show the SEM images of the SiC and Si:SiC films before and after annealing. The surface topology of the film is very smooth, homogenous without any observable crack formation for

both as-sputtered and annealed samples. Also there are no evidence crystal-like or cluster-like structures within the limits of detectibility.

as-sputtered 1100 ^{o}C, 60 min 1100 ^{o}C, 180 min

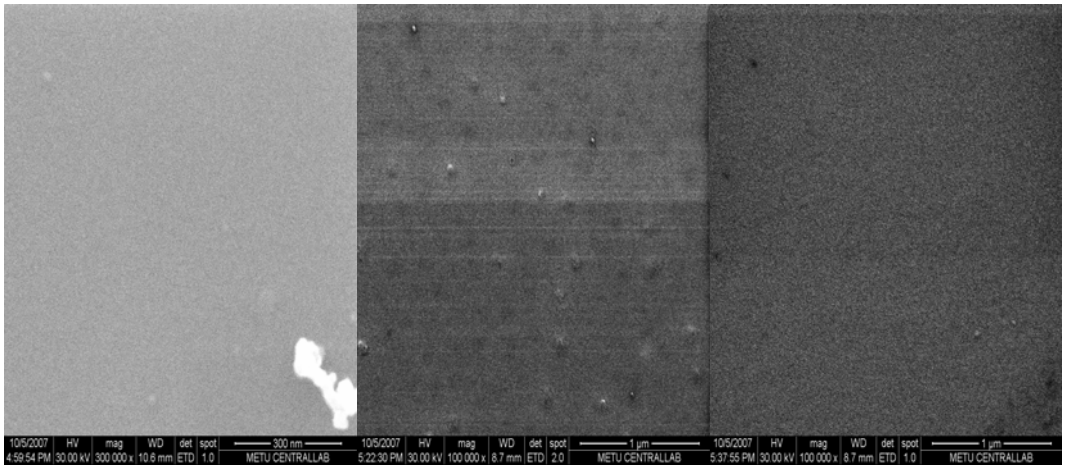

Figure 6.9 SEM images of the as grown and annealed SiC films

as-sputtered 1100 ^{o}C, 60 min 1100 ^{o}C, 180 min

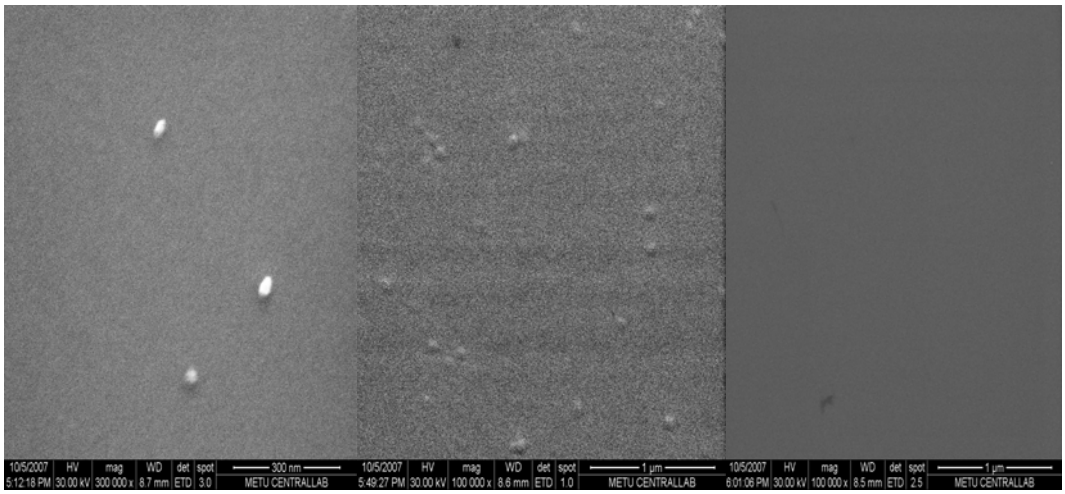

Figure 6.10. SEM images of the as grown and annealed Si rich SiC films

6.3.6. Optical Transmission Spectroscopy

Optical band gap of SiC and Si rich SiC films was investigated from the absorption spectra. It is known that the relation between the absorption coefficient

and the absorption edge energy in amorphous materials may be described as $\alpha h\nu = (h\nu - Eg)^n$ by Tauc et al. [100]. After performing the absorption measurements, absorption coefficient, α was calculated. For the amorphous material having indirect band gap, the graph of $(\alpha h\nu)^{1/2}$ versus incident photon energy is plotted to extract the band gap value. The optical band gap (E_g) of amorphous materials is found from intersection point of the line fitted to the linear part of the graph.

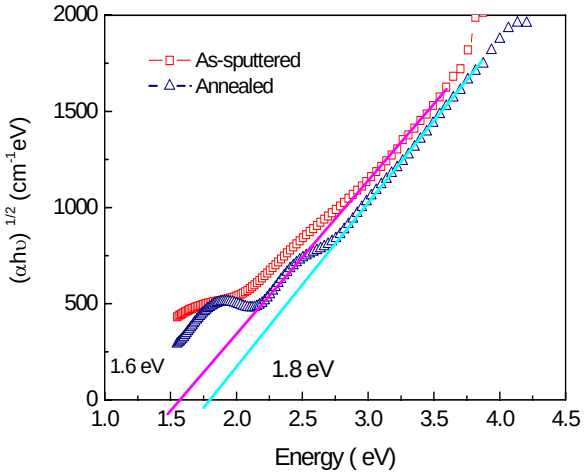

Figure 6.11. The variation of $(\alpha h\nu)^{1/2}$ as a function of incident photon energy for the SiC film before and after annealing

As indicated in Figure 6.11, optical band gap of the as-sputtered SiC thin film is 1.6 eV and that of annealed one is 1.8 eV. The band gap increases with the annealing temperature. Before the annealing, there can be some localized states below the conduction band edge due to the large amount of defects in the film. The apparent band gap is then found to be narrower. The heat treatment removes some of these defects and consequently a wider band gap is obtained [151].

Figure 6.12 shows the optical band gap of Si rich SiC films before and after the annealing. As seen in the figure, optical band gap of the as-sputtered Si rich SiC thin film is 1.5 eV and that of annealed one is 2.0 eV. As in the case for SiC film, the optical band gap increased with the annealing temperature due to presence of

some localized states. Similarly, following the heat treatment, optical band gap is increased as a result of better film structure.

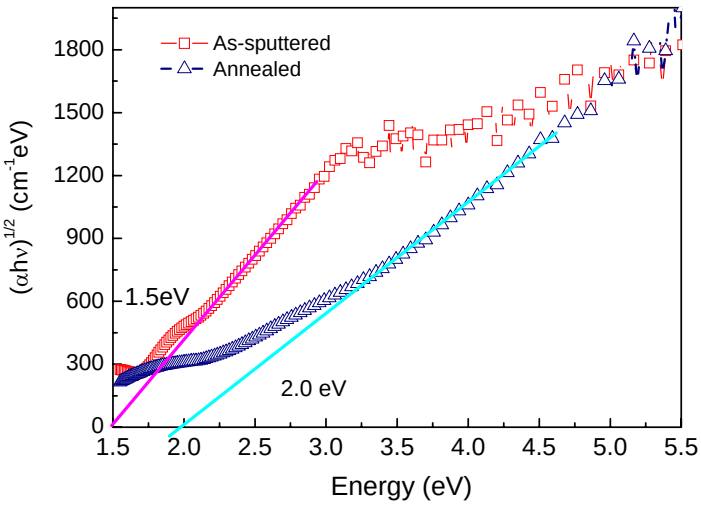

Figure 6.12. The variation of $(\alpha hv)^{1/2}$ as a function of incident photon energy for the samples Si rich SiC film before and after annealing

It is interesting to note that, the optical band gap of Si rich SiC film is lower than that of SiC film. This can be resulted from the additional Si atoms that formed new states in the band gap which ultimately reduces the energy gap [152]. After standard heat treatment procedure, Si-Si bonds are gradually replaced by the stronger Si-C, so the energy gap opens up. The optical band gap of annealed Si rich SiC film environment is very close to that of stoichiometric SiC. So, we can conclude that, the annealed Si rich SiC film is getting more stoichiometric than the annealed SiC film. This result is in good agreement with FTIR represented above.

6.4. Summary and Conclusion

The silicon carbide and silicon rich silicon carbide thin films were deposited on silicon and quartz substrate by RF magnetron sputtering. Structural and optical properties of the film before and after the annealing were studied by analytical techniques. The aim of this study was to reach an understanding of Si nanocrystal formation in SiC films prepared by magnetron sputtering technique.

FTIR spectroscopy has been used effectively. Firstly, the stretching vibration of Si-C bond has been monitored before and after annealing to see whether we have formed good quality SiC films. We found that the intensity of this peak increased, while its FWHM decreased, indicating good stoichiometry and uniformity. Also, the asymmetric stretching vibration of Si-O bonds is seen in the FTIR spectra after the annealing, due to oxidation which was found to be unavoidable in the system we used for annealing process. It is interesting to note that Si rich SiC films are more stoichiometric than SiC. This is understandable because C atoms can easily reach Si atoms when they are more available in the Si rich samples. Si crystallization is seen in the Raman signal. In the Si rich SiC films, some of the additional Si atoms are consumed to form Si-C bonds as evidenced by FTIR, EDX, and Raman analysis. SEM images of the films showed that the surface of the sputtered film was homogenous with no grains or crack like structure before and after the annealing.

As a conclusion, we have shown that Si nanocrystals can be formed in amorphous SiC layers by magnetron sputtering. Presence of excess Si ensures more stoichiometry in the matrix surrounding Si nanocrystals.

CHAPTER 7

SYNTHESIZING AND CHARACTERIZATION OF Si NANOCRYSTALS IN SiC BY MAGNETRON CO-SPUTTERING

7.1 Introduction

As a wide band gap semiconductor, SiC has been an attractive electronic material for high power, high speed, and high temperature applications [23,130]. Recently, it has also attracted attention as a matrix material to host Si nanocrystals (Si NC) for the fabrication of third generation solar cells [16,131]. Since the band gap of Si NCs can be tuned by the quantum size effect, the solar spectrum can effectively be absorbed by Si NCs with different sizes and band gaps in the same solar cell device. Tandem solar cells which have stacked p-n junctions formed by Si NCs with varying sizes have been designed for solar cells with a theoretical efficiency value exceeding 50% [132-134]. Si NCs embedded in a host matrix are generally produced by depositing Si rich films using the techniques such as PECVD [135], ion implantation [83,136], thermal evaporation [137], and magnetron sputtering [138-140]. However, most of the recent studies have focused on Si NCs in dielectric matrices such as SiO_2 (E_g ~9eV) and Si_3N_4 (E_g ~5.3eV) with relatively large band gaps. As these dielectrics are insulating materials the electronic transport through the main body of the device is not a simple process. In these systems, an effective carrier transport should rely on the direct tunneling with stringent requirements on the thickness of the dielectric between nanocrystals. SiC (E_g ~2.5eV) is expected to ease the design requirements with more effective

electrical transport due to the smaller band gap of the matrix material and thus weak confinement for the charge carriers. However, one of the main challenges for the realization of an effective device operation is the fabrication of Si NCs in a SiC matrix in a well controllable and reproducible way. Only a few experimental studies of Si NCs embedded in a-SiC matrix have been reported so far [142]. This work extends the research effort in this field to reach a comprehensive understanding of the SiC : Si system and presents new results on this system.

In this chapter, Si rich SiC single layer and multilayer films with different Si content were prepared by RF magnetron co-sputtering from Si and SiC targets. Following the deposition, samples were annealed at 900, 1000, 1100 and 1200 ^{o}C for 1 h under nitrogen ambient to form Si NCs. The reason of the production of multilayer film instead of single layer film is that the size of the Si NCs can be better controlled and constrained by thickness of the Si rich SiC layer. The fabricated films were characterized using FTIR spectroscopy, Raman Spectroscopy, XPS, GIXRD, and TEM to understand chemical and structural properties of the films containing excess Si which was converted to Si nanocrystals upon annealing. The effects of annealing temperature and the Si amount on the size distribution of Si NCs and on the optical properties of the films were studied and discussed comparatively.

7.2 Experimental Details

7.2.1 Film growth

SiC thin films were deposited on Si (100) and quartz substrate by sputtering single SiC target in Argon ambient at room temperature. Si rich SiC films were prepared by co-sputtering high purity Si and SiC targets by using DC and RF sources, respectively. The electronic grade Ar (6N) was used for co-sputtering of Si and SiC targets.

7.2.2. Deposition Parameters of Si rich SiC Single and Multilayer Films

Single layer end multilayer Si rich SiC films were deposited on quartz and n-type silicon substrate with (100) orientation. For single layer sputtered films, four sets

of samples with varying Si concentrations were deposited. The RF power of SiC was kept constant at 350 W during the deposition. Si concentration of the film was controlled with the varying DC power during the sputtering process. The details of the fabrication parameters are given in Table 7.1.

Table 7.1. Deposition parameters of the Si rich SiC films

Sample ID	Ar Gas Flow (sccm)	Base Pressure (Torr)	Ar Pressure (Torr)	RF Power SiC (W)	DC Power Si (W)
G1	40	1.5×10^{-6}	3×10^{-3}	350	---
G2	40	1.2×10^{-6}	3×10^{-3}	350	70
G3	40	7.1×10^{-7}	3×10^{-3}	350	100
G4	40	7.7×10^{-7}	3×10^{-3}	350	130

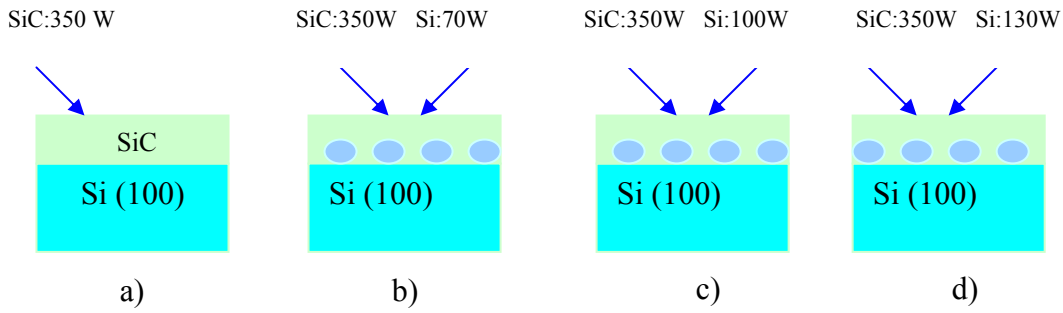

Figure 7.1. The schematic diagrams of the sputtered samples of (a) G1 (b) G2 (c) G3 and (d) G4

For multilayer structures, firstly SiC layer deposited on the Si (100) substrate, secondly Si rich SiC (Si:SiC) layer deposited on SiC layer. This process was repeated 10 times to obtain multilayer structures. The process parameter of SiC layer is same as sample G1, and that of Si rich SiC layer is same as sample G4

seen in the Table 7.1. SiC and Si rich SiC single and multilayer films deposited on silicon and quartz substrate were cut into small pieces and annealed in a fused quartz furnace at 900, 1000, 1100 and 1200 ^{o}C under nitrogen atmosphere for 60 minutes.

7.2.3. Analysis Techniques

FTIR and Raman measurements were performed to monitor vibrational modes of SiC and Si. GIXRD measurements were applied to examine the crystalline structure of the single layer films. The grazing angle between the incident X-ray and the sample surface was fixed at 0.3^{o} to eliminate the substrate contribution. The detector (2θ) was scanned in the range between 30° and 70° at 0.02° steps. XPS depth profiling analyses was used to determine the chemical bonding state and the composition of the throughout films. A TEM analyses was used to obtain the image of the nanocrystals in the deposited film by JEOL2100 TEM operating at 200 kV.

7.3 Characterization of Si rich SiC Single layer Sputtered Films

7.3.1 FTIR spectroscopy

FTIR absorption spectra were recorded to collect the information about the influence of annealing and the Si content on chemical bonding in the sputtered films. The FTIR spectra of SiC thin film without any excess Si are shown in Figure 7.2(a). The peak which is commonly assigned to the Si-C stretching vibration is located at wave number ~776 cm^{-1} for as-deposited sample (Figure 7.2(a)) [20,101,118]. Upon annealing, the position of this peak shifts to the higher wave number to ~799 cm^{-1}, indicating the formation of SiC. The intensity of the peak increases significantly at higher annealing temperatures. We see also that a new peak emerges at ~1082 cm^{-1} and gradually increases with the annealing temperature. This peak, which is typically assigned to the stretching vibration of Si-O-Si bonds [101,154], is indicating that samples are slightly oxidized during the annealing process. Although the annealing was carried out in N_2 atmosphere it appears that the annealing ambient has some oxygen molecules which are sufficient to oxidize the top few layers of the samples. The peak shape of the as-

grown samples is Gaussian type which indicates the amorphous nature of the as-deposited films while that of annealed ones is Gaussian-Lorentzian type which is a good sign for more uniform Si-C bond environments [113,155].

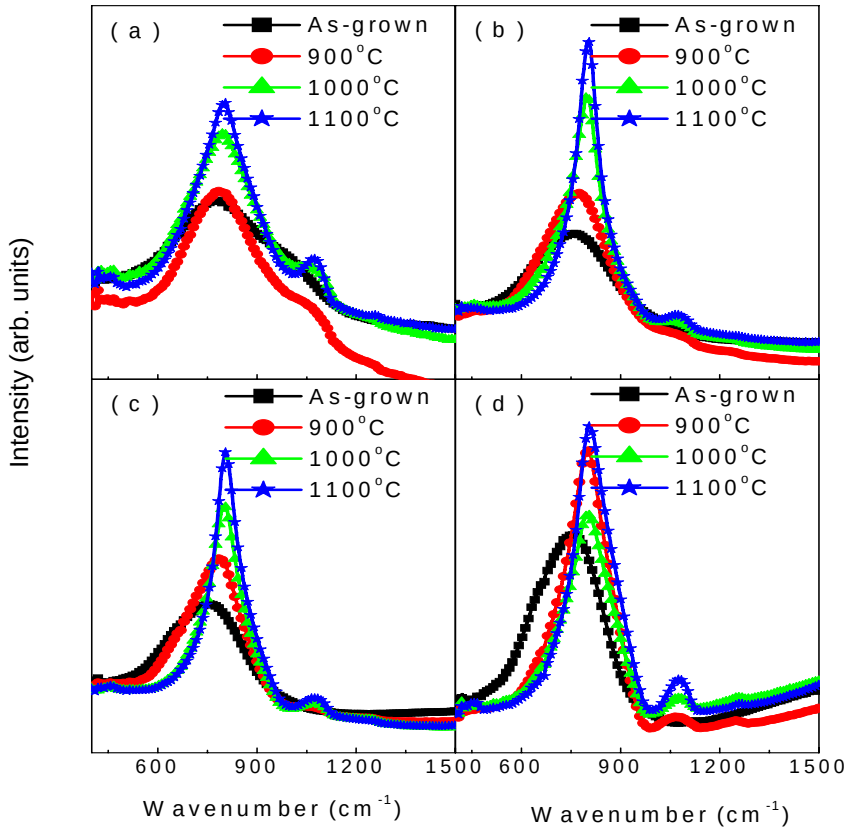

Figure 7.2. FTIR spectra of the samples a) G1 b) G2 c) G3 and d) G4 as a function of annealing temperature.

The FTIR spectra of samples G2, G3 and G4 films with excess Si are seen in Figure 7.2(b), (c), and (d) before and after the annealing process, respectively. As in the sample G2, G3, and G4, FTIR peak position is located at lower wave numbers (742, 746 and 750 cm^{-1}) before the annealing process. They shift to ~ 800 cm^{-1} after the annealing. We see also that the peak width of the samples having excess Si is narrower than the sample (G1) having no intentional excess Si

[154,155]. In order to see the evolution of the film more clearly, the peak position and the FWHM of the Si-C absorption bands are plotted as a function of annealing temperature and Si content of the films in Figure 7.3(a) and (b).

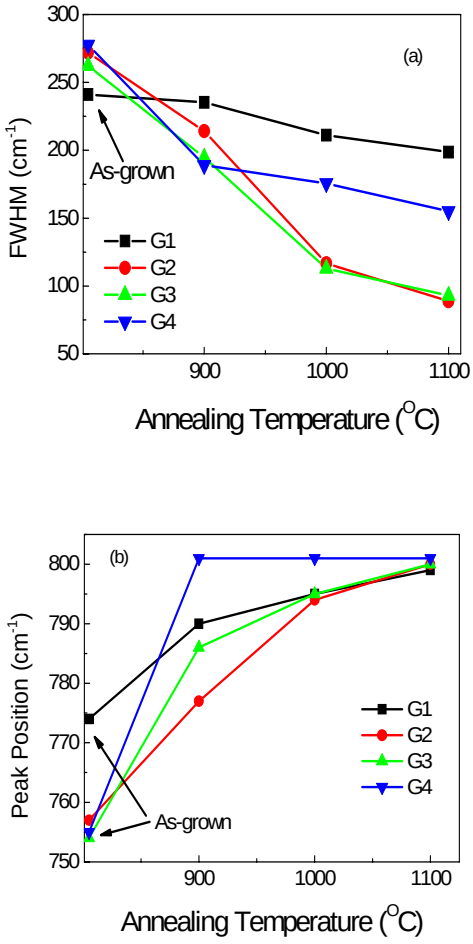

Figure 7.3. a) FWHM and b) Peak position of symmetric stretching Si-C vibration of G1, G2, G3, and G4 with annealing temperature

As shown in the Figure 7.3(a), FWHM of Si-C vibration decreases from 241 cm^{-1} to 199 cm^{-1} with the annealing temperature for the sample G1. The peak position of that peak shifts from 774 to 799 cm^{-1} (Figure 7.3(b)). Samples G2 and G3 exhibit a drastic difference in the variation of FWHM whose value dropped from 260-270 range to 80-90 cm^{-1}. The variation in FWHM is less for the sample G4 which has the highest Si content (from 278 to 156 cm^{-1}). The increase in the

FWHM of the FTIR signal can be attributed to the short range order and the uniformity in the film. On the other hand, the peak position is related to the stoichiometry of the film. It is clear from the observed shift in FTIR that we obtained more stoichiometric and uniform SiC films in samples G2 and G3 after the annealing. However, it should be noted that the FWHM in any of these films couldn't reach that of crystalline SiC films (30-50 cm^{-1}) [154,155]. The uniformity of the SiC without excess Si (sample G1) appears to be worse than the samples with some more Si additions (G2, G3). The average stoichiometry of the films, which can be inferred from the peak position of the FTIR signal, reaches the desired value (800 cm^{-1}) for all samples after the annealing at sufficiently high temperatures [143,144]. This variation appears to have happened at relatively low temperature for sample G4. This is probably due to the availability of more Si atoms in the matrix to form SiC easily. The FWHM is however, smaller in this sample even after very high temperature annealing [144].

7.3.2 Raman Spectroscopy

Figure 7.4 shows the Raman spectra of the (a) G1, (b) G2, (c) G3 and (d) G4 films before and after the annealing. Raman spectra obtained from the sample without excess Si show no indication of the presence of Si-Si and C-C bonds which are typically observed at 521 cm^{-1} and in the range of 1300-1600 cm^{-1}, respectively. The absence of these peaks even after very high temperature annealing ensures that this sample (G1) does not contain any Si or C cluster formation. Carbon clusters in the form of graphite, which could be observed by Raman peaks at 1335 and 1600 cm^{-1} associated with C-C bonds G line (sp^2) and D line (sp^3) [113], has not been detected in any of the samples fabricated in this study.

The broad band seen in between 350 and 500 cm^{-1} in sample G1 can have contribution from SiC in amorphous phase [120]. However, the main contribution to the Raman signal in this range results from amorphous Si especially in the samples with higher Si content. Amorphous Si is known to generate an asymmetric Raman peak resulting from transverse optical modes of oscillations [112,145,145]

Upon annealing at 1000 ^{o}C, all samples are still showing amorphous characteristic with the band at around 470 cm^{-1} in Figure 7.4(a). However, at higher annealing temperatures (> 1000 ^{o}C), Raman spectra of Si rich SiC films (G2, G3, G4) exhibit the characteristic Si peak at around 520 cm^{-1} associated with Si-Si bond formations [127]. The strong asymmetry seen in the main Raman peak is an indication of formation of nanocrystals with varying size [19]. The intensity of the peak depends on the amount of Si and the temperature of the annealing. As seen from Figure 7.4(b), sample G2 with least amount of excess Si exhibits a weak Si-Si signal only after the annealing at 1200 ^{o}C. For samples G2 and G3, the nanocrystal formation is clearly observable even at 1100 ^{o}C. For G4 with maximum Si content the signal strength is very high and nanocrystal formation is almost visible even at 1000 ^{o}C.

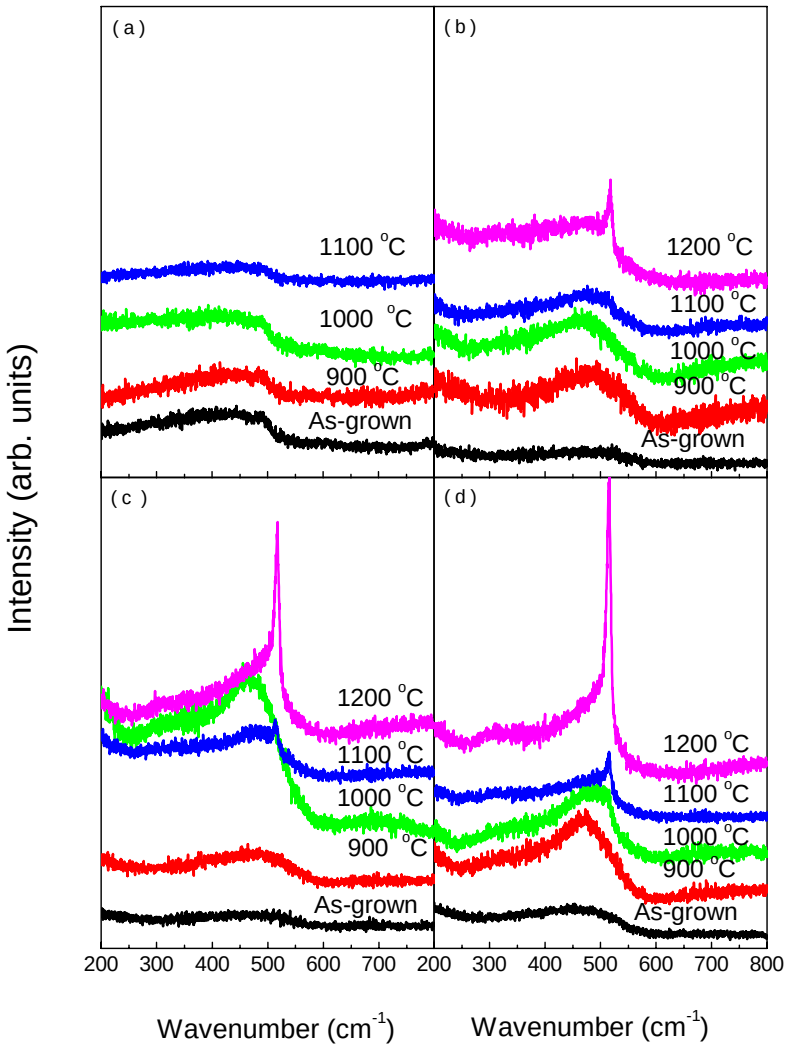

Figure 7.4. Raman spectra of a) G1 b) G2 c) G3 and d) G4 with the annealing temperature

7.3.3. X-Ray Diffraction

GIXRD analysis was used to provide the information about the structural investigation and to confirm the formation of Si NCs with annealing temperatures. Figure 7.5 shows the XRD spectra of the Si rich SiC film as a function of annealing temperatures. XRD spectrum of the as-deposited single layer film does not contain any crystalline peaks, which is pointing to amorphous characteristic of

the film (Figure 7.5). After annealing at 900 ^{o}C, XRD spectra of the single layer film show the presence of crystalline phase that can be associated with formation of Si NCs. The two major diffraction peaks centered at around 2θ=35.4^{o} and 56.2^{o} are from Si(211) and Si(311) planes, respectively [127,131]. This reveals that Si NCs formation has occurred at 900 ^{o}C. In addition to these peaks, several new peaks were detected in the single layer film annealed at temperature >900 ^{o}C. According to the data from the Joint Committee on Powder Diffraction Standards these additional peaks centered at 2θ=28.3^{o}, 47.3^{o} and 60.8^{o} corresponds to Si(111), Si(220) and Si(331) planes, respectively [127,131]. The intensity of these peaks increases with the annealing temperature. These results are in agreement with the HRTEM and Raman results.

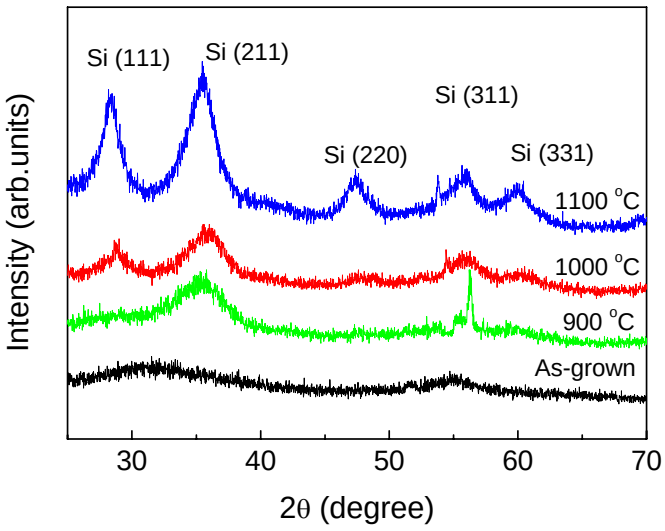

Figure 7.5. XRD spectra of the sample G4 with the annealing temperature

The nanocrystal size was calculated using Scherrer's equation [72] from the dominant Si diffraction peak as a function of the annealing temperature. Figure 7.6 shows the calculated sizes of Si nanocrystals as a function of annealing temperature in the Si rich SiC films. As seen from Figure 7.6, the Si nanocrystal size increases from ~3 to 6 nm for Si rich SiC film as a function of annealing temperatures.

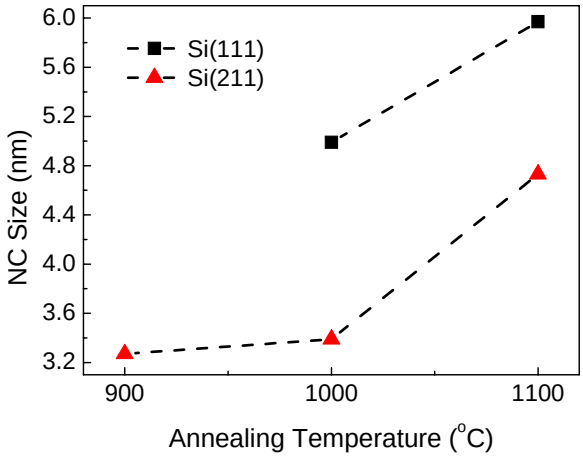

Figure 7.6. Si NC size calculated by Scherrer's formula with the annealing temperature

7.3.4. X-Ray Photoelectron Spectroscopy

XPS analysis of the as-deposited and annealed samples was performed to understand the chemical structure of Si rich SiC sputtered films. The depth profile measurements of the Si rich SiC films were carried out by sputtering with an Ar^+ beam having the acceleration voltage 2000 V. The peak fitting procedure and Shirley background correction were applied by XPSPEAK95 software. C 1*s*, Si 2*p* and O 1*s* states were monitored for all studied samples. As a representative example, we display the illustration of the Si 2*p* peak of the sample G4 after the annealing as a function of the depth in Figure 7.7. A similar depth profiling was obtained for C 1*s* and O 1*s* peaks, but not displayed here as it does not carry any additional information. In all cases, the surface layer was sputtered before starting the analysis to remove the contamination caused by the direct contact with air prior to loading the samples into the UHV chamber.

For the as-sputtered film, C 1*s* and Si 2*p* peaks were measured to be at 282.8 eV and 99.8 eV, respectively. The peak position of these signals was almost constant throughout the film. C 1*s* peak is slightly lower than the commonly measured

value (284.5 eV) for C-C bonds [101,118]. This shift in the binding energy towards lower energy value is an indication of the Si-C bond formation in agreement with the results obtained from Raman and FTIR analysis. Similarly Si peak is located at a position shifted to higher energy value as a result of the Si-C formation [118].

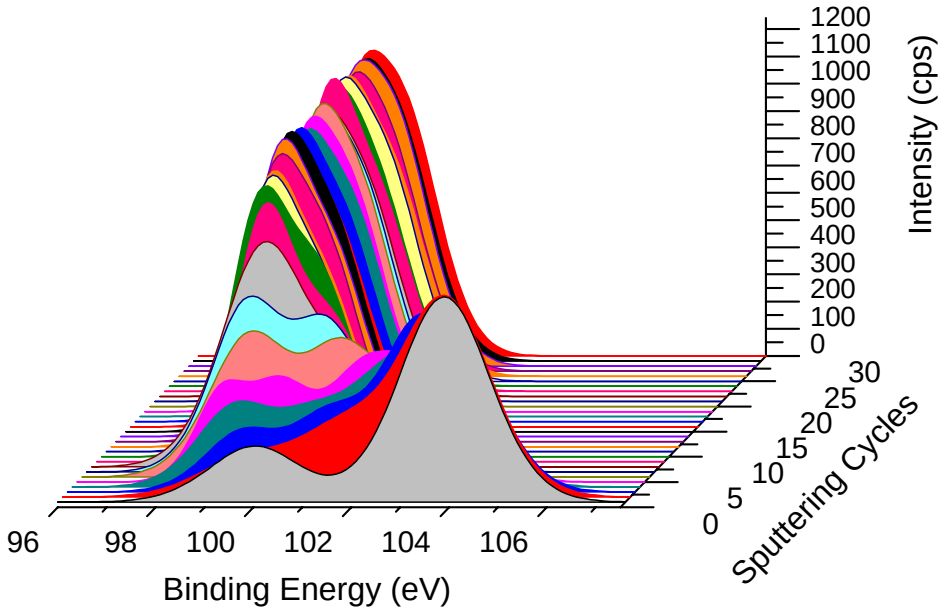

Figure 7.7. XPS depth profiles of the annealed sample G4 for Si 2*p*.

The chemical structure of the annealed films with excess Si was found to be different than that of the as-sputtered sample. During the annealing process, the residual oxygen in the nitrogen gas of the ambient oxidized Si atoms in the top layers of the film as can be seen from Figure 7.7 [101,148]. The variation in the oxidized region with the depth is clearly seen as the top layers of the sample were successively removed by Ar^+ sputtering. The presence of oxidation states of Si (Si^{1+}, Si^{2+} Si^{3+} and Si^{4+}) is detectable with the shift towards higher the binding energy values with the increasing oxidation state [119,148]. The oxidation states of Si change from Si^{4+} to the lower states gradually as the surface layers were

removed by Ar^+ sputtering. This variation is accompanied by a decrease in the peak intensity of the higher oxidation states. The peak position is stabilized at around 100 eV of unoxidized Si after 10^{th} sputtering cycle. While the oxidation states of Si atoms are easily detectable, the differentiation of Si-C and Si-Si peaks is rather challenging.

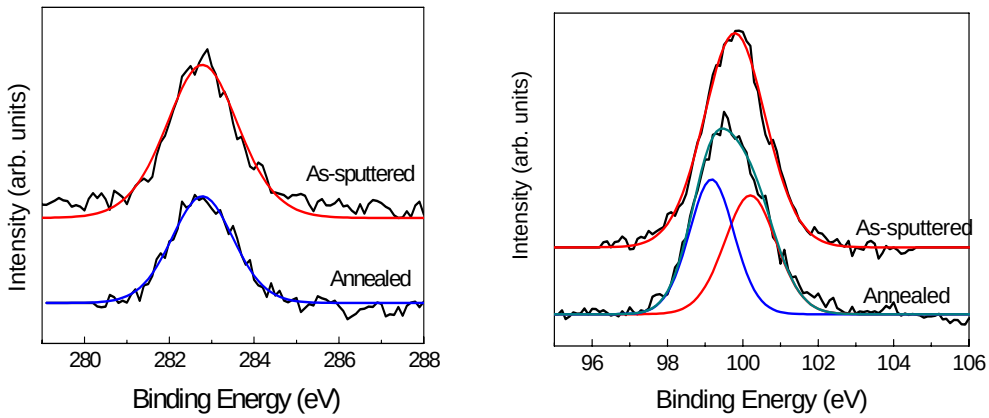

Figure 7.8. Deconvoluted XPS spectra of a) Si 2*p* and b) C 1*s* before and after annealing for the sample G4

For the separation of Si-Si and Si-C peaks in the XPS spectrum, a deconvolution process was applied to Si 2*p* and C 1*s* signals obtained after the 10^{th} sputtering cycle. An example from this analysis is shown in Figure 7.8(a) which displays XPS spectra of the Si 2*p* after 19^{th} sputtering cycle before and after the annealing. For the as-sputtered sample, XPS raw data of the Si-C peak was well fitted to a single Gaussian peak centered at 99.8 eV [118,127]. After the annealing, the measured signal could be fitted to two Gaussian peaks located at 100.2 eV and 99.3 eV. In this curve fitting process, we attempted to fit different peak combinations including one single peak to the experimental data [154,155]. These attempts yielded no better fit than the double peak fit shown in Figure 7.8(b). It is then concluded that the Si 2*p* peak can be decomposed to two peaks corresponding to Si-C and S-Si bonds which are coexisting in the fabricated film. This is in agreement with the TEM and Raman results.

We observed no indication of the presence of other C phases such as C-C bonds in the samples studied [154]. Moreover, it is also seen that the annealing caused a slight shift in the Si 2*p* signal to lower binding energy while the C 1*s* peak was not affected by the annealing process. This is an indication of Si-Si bond formation associated with Si nanocrystals which is usually identified by a binding energy at around 99 eV [101,128,147].

7.3.4. Transmission Electron Microscopy

Finally, we performed the TEM analysis of the Si rich SiC samples annealed at high temperature in order to observe the presence of Si nanocrystals directly. Results are used to obtain information about the shape, size and the crystallinity of the Si nanocrystals in the SiC matrix. Figure 7.9. shows a typical cross-sectional HRTEM image of the sample G4 annealed at 1100 ^{o}C for 1h. The Si nanocrystals in the a-SiC matrix was not detectable in the samples annealed at lower temperatures (900 ^{o}C and 1000 ^{o}C). This is in line with the Raman results presented above. In the annealed sample, the HRTEM image clearly shows formation of Si nanocrystals in the amorphous SiC matrix. Lattice fringes of Si nanocrystals are visible in the selected areas as marked by circles in Figure 7.9. We estimated the mean grain size of the Si nanocrystals as 2-5 nm from a series of pictures obtained from different sample pieces. The corresponding selected area diffraction (SAD) pattern showed crystalline phases with no special orientation.

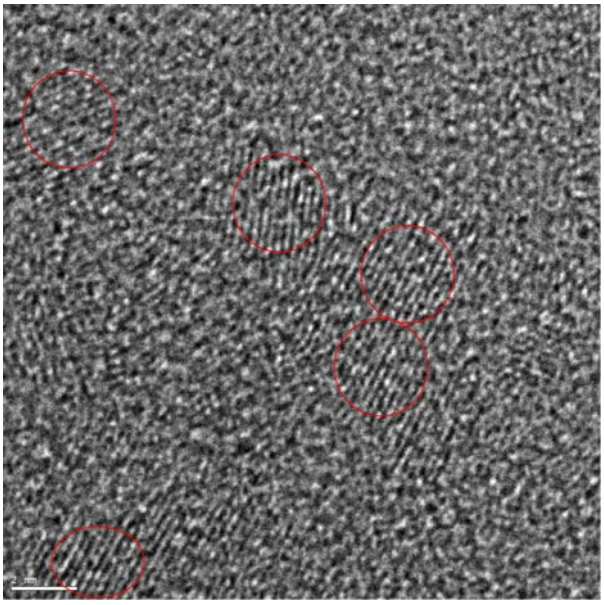

Figure 7.9. HRTEM cross-sectional image of sample G4 after annealing. Circles are drawn to guide the eye.

7.4 Characterization of Si rich SiC Multilayer Sputtered Films

7.4.1 FTIR Spectroscopy

FTIR spectra of SiC/Si:SiC multilayer film are shown in Figure 7.10(a). The FTIR peak which is typically attributed to Si-C stretching vibration is located at wave number at 757 cm^{-1} for as deposited sample (Figure 7.10(a)) [101,118]. Upon the high temperature treatments, the position of this peak shifts to the higher wave number at 797 cm^{-1}, indicating the formation of SiC. The intensity of this peak enhances significantly at higher annealing temperature. We observe also that a new additional peak emerges at ~1080 cm^{-1} and gradually increases with the annealing temperature. This peak, which is related to asymmetric stretching vibration of Si-O-Si bonds, is indicating that samples are slightly oxidized during the annealing process. It is seen that the annealing ambient has some oxygen molecules which are sufficient to oxidize the top few layers of the sample. The peak shape exhibits similar properties as the single layer structures. We see also that the peak width of the sample becomes narrow with the annealing temperature [154]. In order to see the progress of the film, the peak position and FWHM of the

Si-C absorption bands are drawn as a function of annealing temperature in the Figure 7.10(b).

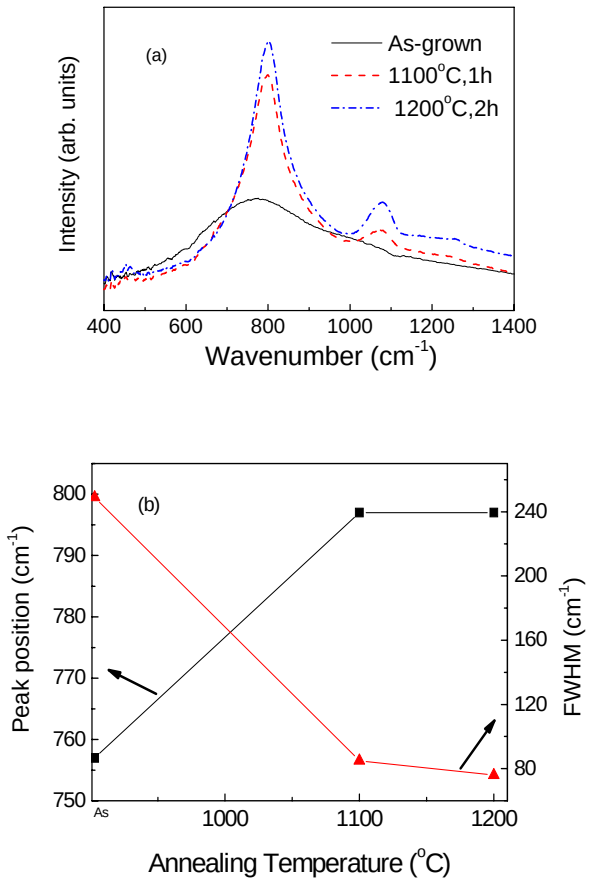

Figure 7.10. (a) FTIR spectra of the multilayer sample and (b) the variation of peak position and FWHM with the annealing temperature

As shown in the Figure 7.10(b) FWHM of Si-C vibration decreases drastically from 249 to 76 cm^{-1} with the annealing temperature. The peak position of that peak shifts from 757 to 797 cm^{-1} (Figure 7.10(b)). This variation of FWHM can be attributed to the improvement of the film in the short range order and thus the uniformity in the film [142]. On the other hand, the peak position is related to the stoichiometry of the film [132,142]. The peak position of the FTIR signal approaches the ideal value (~800 cm^{-1}) for the SiC formation upon annealing at sufficiently high temperatures [144,153]. As in the case of single layer structure, we reached more stoichiometric and uniform SiC formation in the sputtered

multilayer film with the annealing. However, it should be pointed out that the value of the FWHM in the film couldn't reach that of fully crystalline SiC film (30-50 cm^{-1}) [154,143].

7.4.2. Scanning Electron Microscopy

The cross-sectional image of the multi layer film after annealing was investigated with SEM operating at 30 kV. Figure 7.11 shows the cross-sectional SEM image of sputtered multilayer sample. Even though the contrast between Si:SiC and SiC layer is not so clear, the micrographs shows the presence of each layer. The thickness of SiC and Si:SiC layer is about 18 and 16 nm, respectively. Both SiC and Si:SiC layer is homogeneous and free from major defects such as voids and cavities. The resolution of the SEM is not enough to observe the nanocrystalline Si in the Si:SiC layer. In order to get further information about the multilayered structure of the samples, TEM results will be discussed in the section 7.4.4.

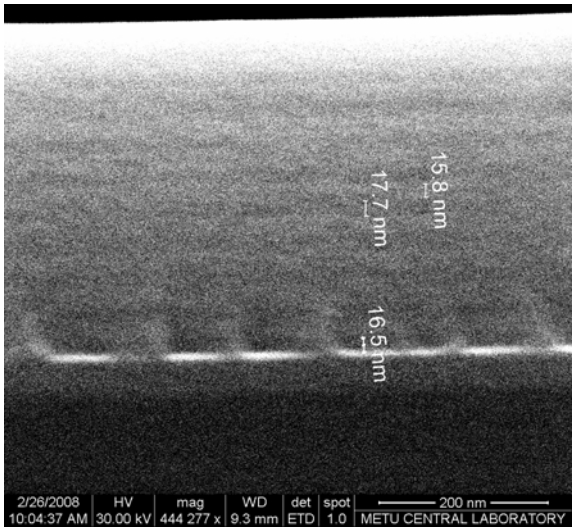

Figure 7.11. Cross-sectional SEM image of the sputtered multilayer film

7.4.3 Transmission Electron Microscopy

For further investigation, we carried out TEM analysis of the multilayer film annealed at high annealing temperature in order to detect the presence of Si

nanocrystals directly. TEM investigation should provide information about the shape, the size and the crystallinity of the Si nanocrystals in the multilayer film. Figure 7.12 presents a typical cross-sectional micrograph of the SiC/Si rich SiC multilayer film annealed at 1100 ^{o}C for 1 h. The layered structure of the annealed sample with interfaces is seen in the TEM pictures shown in Figure 7.12(a) and (b). The SiC and Si rich SiC layers can be recognized light and dark bands in the picture, respectively. The presence of Si nanocrystals are detectable in the Si rich SiC layers annealed at 1100 ^{o}C in the high resolution images shown in Figure 7.12 (c) and (d).

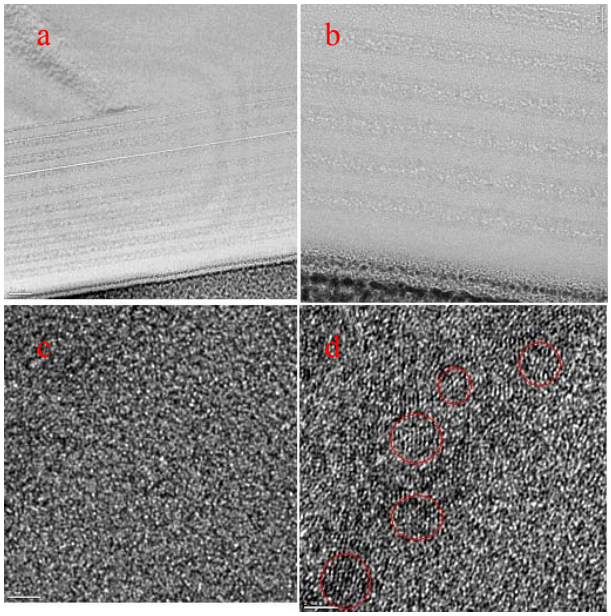

Figure 7.12. a) TEM cross-sectional overview image of the SiC/Si rich SiC multilayer annealed at 1100 ^{o}C, b) TEM cross-sectional image of first 6 periods in the $Si_{1-x}C_x$ multilayer of sample after annealing, c) TEM cross-sectional image of SiC layer in the multilayer film annealed at 1100 ^{o}C, d) TEM cross-sectional image of Si rich SiC layer in the multilayer film annealed at 1100 ^{o}C (the visible Si NCs are indicated by solid-line circles)

Lattice fringes of Si nanocrystals are visible in the selected areas as marked by circles in Figure 7.12(d). We estimated the mean grain size of the Si nanocrystals as 2-5 nm from a series of pictures obtained from the different sample pieces. The

corresponding SAD pattern showed crystalline phases with no special orientation. The SiC layers between Si rich layers features a uniform amorphous phase (Figure 7.12(c)). No lattice fringes associated with the nanocrystal formation were observed in the SiC layers.

7.4.4 X-Ray Photoelectron Spectroscopy

Finally, XPS depth profile analysis of the multilayer samples was performed to understand the chemical structure, bonding formation of the multilayer films before and after annealing. XPS peaks of C 1*s*, Si 2*p*, and O 1*s* states were observed for all studied samples. Before starting the analysis for all studied samples, the surface layer of the multilayer film was sputtered to remove the unwanted contamination.

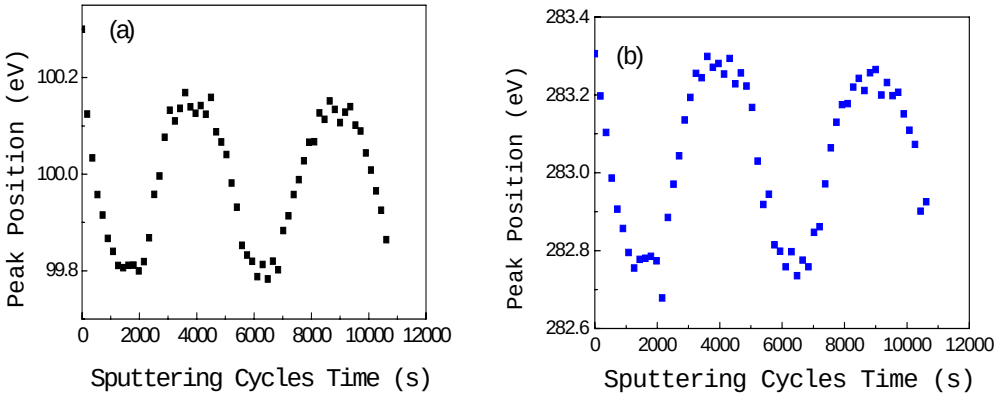

Figure 7.13. Peak position of a) Si 2*p* and b) C 1*s* state for as-sputtered multilayer film

Figure 7.13 shows the peak position of Si 2*p* and C 1*s* state for the as-sputtered multilayer film. For as-sputtered multilayer film, the peak position of Si 2*p* signal oscillates between 99.8-100.2 eV, while that of C 1*s* signal oscillates in the range of 282.7-283.3 eV from the surface to the depth shown in Figure 7.13. XPS binding energy peaks of Si 2*p* and C 1*s* are usually measured at around 99.3 and 284.5 eV, respectively [103]. The shift in the binding energy of Si 2*p* state

towards higher value indicates the Si-C bond formation in agreement with the results obtained from the Raman and FTIR measurements. Similarly, the binding energy of C 1*s* shifts towards a lower value indicates the presence of Si-C formation. The oscillation in the peak position of Si 2*p* and C 1*s* signals illustrates the multilayer structure with and without excess Si. The peak position of the Si signal is at 99.8 eV in the Si rich layer , which is closer to the Si 2*p* value in the Si matrix, while that of Si signal reaches the value of 100.2 eV indicating to Si-C bond formation in the SiC layer [103]. Similarly, the shift towards lower binding energy value of the C 1*s* state in the Si rich SiC layer indicates more Si atom in the environment.

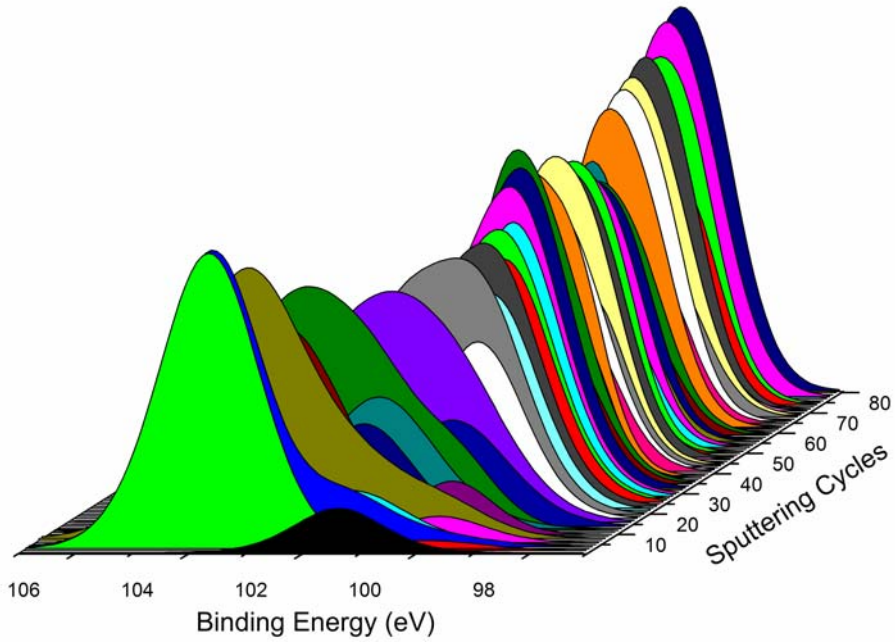

Figure 7.14. XPS depth profiles of 1100 ^{o}C annealed multilayer sample for Si 2*p*

During the annealing process, Si atoms in the very top layers in the multilayer film was oxidized by the residual oxygen in the nitrogen gas ambient as can be seen in Figure 7.14 [101.113]. The oxidized surface layers were removed by Ar^{+} sputtering. During this process, the intensity of the higher oxidation state was decreased and the binding energy of these states shifts from 104 eV to 99.8, as a result of less oxidation as we reach deeper layers. After 8 sputtering cycles, the

peak position of Si signal is saturated at around 100 eV corresponding to unoxidized Si in the multilayer film.

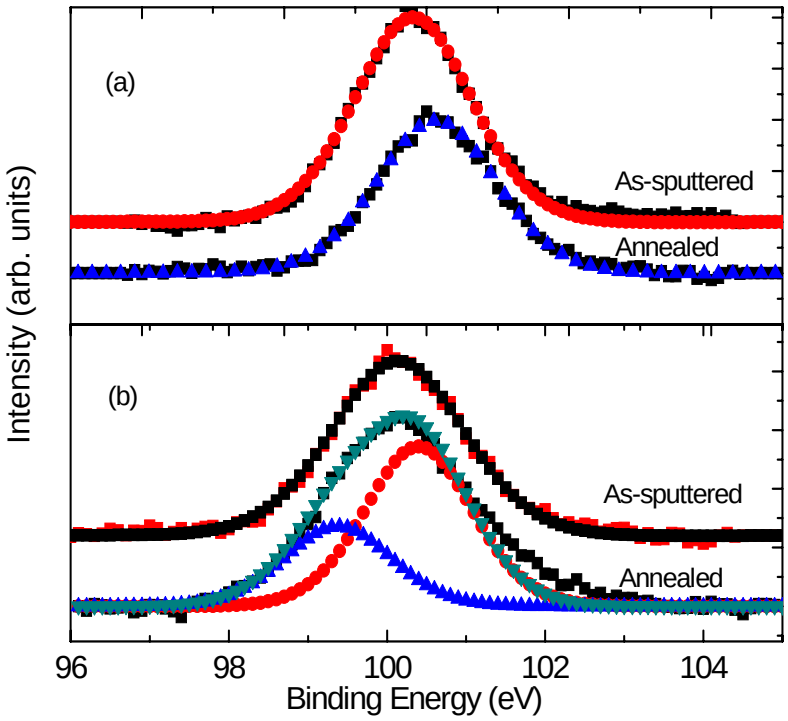

Figure 7.15. Deconvoluted spectra of Si 2*p* a) SiC b) Si rich SiC layer in the multilayer film before and after annealing

In order to differentiate Si-C and Si-Si signals in the XPS spectrum, a deconvolution process was performed to Si and C peaks after the 8th sputtering cycle for Si rich SiC and SiC layer in the multilayer film. An example of deconvoluted spectrum of the Si 2*p* 10th and 28th layer in Si rich SiC and SiC layers is shown in Figure 7.15. For the as-deposited sample, XPS measured signal of the Si 2*p* peak is well fitted to one Gaussian peaked at 99.8 eV [118,127]. Upon annealing, experimental data of the Si 2*p* 10th cycle could only be fitted to two Gaussian peaks located at 100.1 and 99.3 eV, while that of 28th cycle could be fitted to a single peak. Therefore, it can be concluded that Si 2*p* signal can be well

fitted to double peaks corresponding to Si-C and Si-Si bonds, which are coexisting in the Si rich SiC layer. On the other hand, this is not possible in for the signal resulted from Si substrate or pure SiC layer. XPS results show that the presence of Si-Si bond formation associated with Si nanocrystals was only monitored in the Si rich SiC layer.

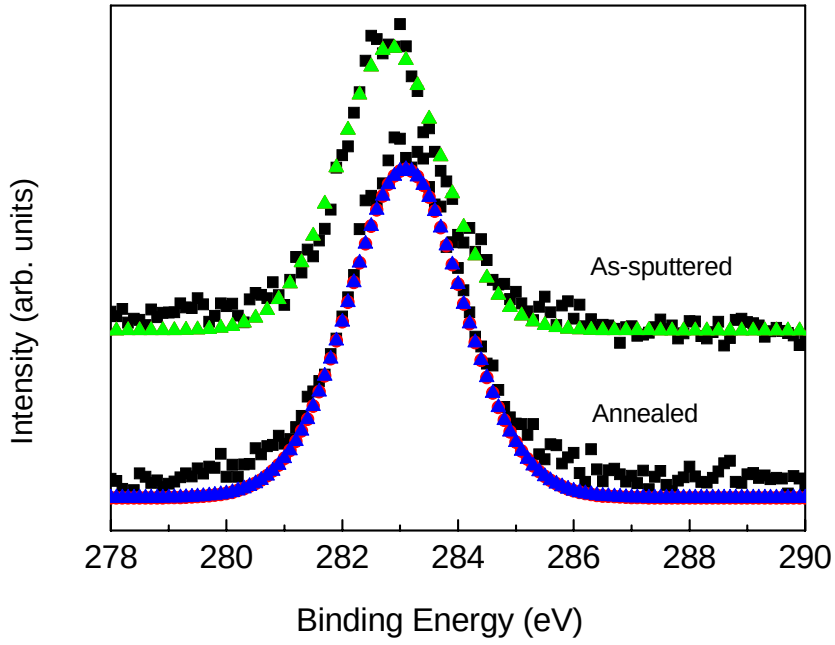

Figure 7.16. Deconvoluted spectra of C 1s before and after annealing for multilayer film

XPS raw data of C 1s signal is fitted to the single peak at 282.5 eV corresponding to Si-C bond seen in Figure 7.16. We could not observe any indication of C-C bonds in both Si rich SiC and SiC layer of the multilayer sample studied. On the other hand it is seen that the annealing caused a slight shift in the C 1s signal to the higher energy.

7.5. Summary and Conclusion

Si rich SiC single and multilayer films were fabricated on silicon and quartz substrate by magnetron co-sputtering. The chemical and structural features of the single layer and multilayer films were studied by the major analytical techniques. The presence of symmetric stretching vibration of Si-C bonds was confirmed in the FTIR spectra of the sample. High temperature annealing resulted in an enhancement in the intensity accompanied by a decrease in the FWHM of the Si-C bonds. After the annealing, we observed also asymmetric stretching vibration of Si-O bonds in the FTIR spectra, due to the surface oxidation during the annealing process. The evidence of Si crystallization was obtained from Raman measurements, where the intensity of Si Raman shift increased with the Si content of the film and annealing temperature. Although some weak sign of Si crystallization could be seen in the samples annealed at 1000 ^{o}C annealing, Raman signal was clearly visible only after 1100 ^{o}C annealing. Also, grazing incidence XRD provided us with the information about the Si crystallization. The grain size of the Si nanocrystal was estimated as 3-5 nm by Scherrer's formula. XPS provided us with the elemental information and their chemical states of the atomic species of the SiC films with and without excess Si. Depth profiling with XPS revealed that the top surface of the film was oxidized during the annealing process while the main bulk of the structure is composed of SiC matrix without the presence of oxygen. In the Si rich SiC layer of the multilayer films, the formation of Si nanocrystals could be inferred from the shift in the binding energy and the presence of two peaks corresponding Si-Si and Si-C bonds in the Si 2*p* signal. Finally, the conclusive evidence for the Si nanocrystal formation was obtained from the high resolution TEM study which showed the images of Si nanocrystals with sizes of 2-5 nm. The localized structure and lattice fringes could be seen from the cross sectional images of the samples.

CHAPTER 8

SUMMARY AND CONCLUSIONS

In this thesis, fabrication and characterization of nanocrystals in different matrices has been studied. Various diagnostic techniques have been employed for the characterization of the semiconductor nanocrystals. FTIR spectroscopy was performed to study the hosting matrix during the formation of Si and Ge nanocrystals. Recovery of the SiO_2 matrix was investigated for different process parameters. Particularly, the deconvoluted asymmetric stretching bond of SiO_x was examined to monitor the structural perfectness of the host matrix. It was shown that the SiO_2 matrix was getting better stoichiometry during the formation of nanocystals. These results can be used to confirm the nnocrystal formation in the SiO_2 matrix. We have shown in this study that can be used to study not only the matrix material but also nanocrystals formed in it.

In the second part of this work, Si nanocrystal formation in SiC matrix was studied for the purpose of new generation light emitting diodes and solar cells. For this purpose, SiC and Si rich SiC single and multilayer films were fabricated by using magnetron co-sputtering and PECVD techniques. This work presents new contributions to the recent research efforts in this direction. Post annealing at different temperatures was carried out in order to investigate the evolution of SiC

matrix and/or Si nanocrystals during a heat treatment. Spectroscopic techniques were employed in order to probe the physical and chemical structures of the samples.

Raman spectroscopy was used to obtain information about the formation of the Si nanocrystals in a mixed system. The effect of the high annealing temperature and amount of Si in the SiC films was studied with Raman spectroscopy. As expected, the intensity of the Raman signal increased with increasing temperature. The strong asymmetry of the Raman signal is related to the size distribution of the Si nanocrystals. The crystallinity of the SiC matrix with annealing temperatures can also be studied with Raman spectroscopy.

XRD was used to identify the crystallinity of the SiC at different annealing Temperatures. It was shown that as the temperature increases, the transition from amorphous to crystalline phase is seen. For the SiC samples with excess Si, a very broad peak emerged at around $2\theta=28.5^{o}$, where it corresponds to the scattering from the successive (111) planes of Si clusters. The width of the peak decreases with increasing annealing temperature. This indicates that the nanocrystal size consistently increases with increasing temperature. The size of the nanocrystals, which was calculated by using Scherrer's formula were changing between ~ 2 to 5 nm depending on the Si content and annealing temperature. These values are in agreement with HRTEM results.

The structure of Si nanocrystals and the variation of the host matrix with respect to depth were studied by XPS. Formation of Si nanocrystals was identified from the presence of Si-Si bonds after theannealing. However, it was found that, Si atoms at the top layer of the sample are oxidized during the high temperature annealing treatment. The oxidation states of Si atom from Si^{4+} to Si^{0} were detected at the surface region of the film. The depth profile investigations of XPS were consistent with FTIR results.

Some suggestions can be made for future studies: the size of the nanocrystals should be controlled for a reliable device operation. Size control is crucially important in devices like tandem structures proposed for third generation solar cells. Optical properties of SiC matrix with Si nanocrystals can be investigated in more detailed manner by using PL and temperature dependent PL spectroscopy. Electrical properties of Si containing SiC multilayer structure can be investigated C-V and I-V measurements. Finally, devices such as light emitting diodes and solar cells can be fabricated with the material structures investigated in this work

REFERENCES

[1] J. Bardeen and W.H. Brattain, Phys. Rev. 75, 1208 (1949)

[2] G. E. Moore, Electronics 38, 114 (1965)

[3] G. E. Moore, Tech. Dig. IEDM 21, 11 (1975)

[4] M. Law, J. Goldberger, and P. Yang, Annual Review of Material Research 34, 83 (2004)

[5] P. Avouris, J. Appenzeller, R. Martel, and S. J. Wind, Proceedings of the IEEE 91, 1772 (2003)

[6] R.A. Rao, R.F. Steimle, M. Sadd, C.T. Swift, B. Hradsky, S. Straub, T.Merchant, M. Stoker, S. G. H. Anderson, M. Rossow, J. Yater, B. Acred, K. Harber, E. J. Prinz, B. E. White, and R. Muralidhar, Solid-State Electronics 48, 1463 (2004)

[7] M.J. Lu, X.M. Wua, and W.G. Yao, Mat. Sci. Eng. B 100, 152 (2003)

[8] D. Tsoukas, P. Dimitrikas, S. Kolliopolou, and P. Normand, Mater. Sci. Eng. B 93 124 (2004)

[9] B. Kaleli, "*Towards Silicon Based Light Emitting Device: Photoluminescence From Terbium Doped Silicon Matrices With Or Without Nanocrystals"* , M. Sc. Thesis, Department of Physics, METU, Ankara (2009)

[10] A.J. Kenyon, Semicond. Sci. Technol. 20, 65 (2005)

[11] M. Kulakci, U. Serincan, and R. Turan, Semicond. Sci. Technol. 21, 1527 (2006)

[12] Y. Wang and N. Herron, J. Phys. Chem. 95, 525 (1991)

[13] D. Sahin, "*Structural And Electrical Properties Of Flash Memory Cells With HfO_2 Tunnel Oxide And With/Without Nanocrystals"*, M. Sc. Thesis, Department of Physics, METU, Ankara (2009)

[14] I. B. Akca, A. Dana, A. Aydinli, and R. Turan, Appl. Phys. Lett. 92, 052103 (2008)

[15] G. Conibeer, Mater. Today, 10, 11 (2007)

[16] G. Conibeer, M. Green, R. Corkish, Y. Cho, E.-C. Cho, C.-W. Jiang, T. Fangsuwannarak, E. Pink, Y. Huang, T. Puzzer, T. Trupke, B. Richards, A. Shalav, and K.-I. Lin, Thin Solid Films 511, 654 (2006)

[17] E. S. Marstein, A. Gunnæs, U. Serincan, S. Jørgensen, A.Olsen, R. Turan, and T.G. Finstad, Nucl. Instr. and Meth. B 207, 424 (2003)

[18] E.S. Marstein, A.E. Gunnæs, U. Serincan, R. Turan, A. Olsen, and T.G. Finstad, Surf. Coat. Technol. 158, 544 (2002)

[19] U. Serincan, G. Kartopu, A. Guennes, T.G. Finstad, R. Turan, Y. Ekinci, and S.C. Bayliss, Semicond. Sci. Technol. 19, 247 (2004)

[20] Y. Kurokava, S. Tomita, S. Miyajima, A. Yamada, and M. Konagai, Jpn. J. Appl. Phys. 46, L833 (2007)

[21] J.A. Edmond, K. Das, and R.F. Davis, J. Appl. Phys. 63, 922 (1998)

[22] J.H. Edgar, J. Mater. Res. 7, 235 (1999)

[23] H. Morkoc, S. Strite, G.B. Gao, M.E. Lin, and M. Burns, J. Appl. Phys. 76, 1363 (1996)

[24] D.J. Hayton, T.E Jenkins, P. Bailey, and T.C.Q. Naokes; Semicond. Sci. Technol. 17, L29 (2002)

[25] L.S. Ramsdell, Am. Minerol. 32, 64 (1947)

[26] N.W. Jepps and T.F. Page, Prog. Cryst. Growth Charact. 7, 259 (1998)

[27] C.H. Park, B.-H. Cheong, K.-H. Lee, and K.J. Chang, Phys. Rev. B 49, 4485 (1994)

[28] W.Y. Ching, J. Am. Ceram. Soc. 73, 3135 (1990)

[29] P. Hohenberg and W. Kohn, Phys. Rev. 136, B864 (1964)

[30] W. Kohn and L.J. Sham, Phys. Rev. 140, A1133. (1965)

[31] W.Y. Ching, L. Ouyang, and Y.-N. Xu, Phys. Rev. B 67, 245108 (2003)

[32] A.C. de Oliveiraa, J.A. Freitas Jr.b, W.J. Mooreb, A. Ferreira da Silvac, I. Pepec, J. Souza de Almeidace, G.C.B. Bragad, J.M. Osório-Guillene, C. Perssone, and R. Ahujae, Mater. Res. 6, 47 (2002)

[33] J.R. Ferraro, R. Nakamoto, and C.W. Brown, *Introductry Raman Spectroscopy*, Academic Press, 143, USA (2003)

[34] A.A. Langford, M.L. Fleet, B P.Nelson, W.A. Lanford, and N. Maley, Phys. Rev. B 45, 13367 (1992)

[35] P. Melinon, P. Keghelian, A. Perez, C. Ray, J. Lerme, M. Pellarin, M. Broyer, M. Boudeulle, B. Champagnon, and J.L. Rousset, Phys. Rev. B. 58, 16481 (1998)

[36] W. Bolse, J. Conrad, T. Roedle, and T. Weber, Surf. Coatings. Technol. 74, 927 (1995)

[37] R.J. Iwanowski, K. Fronc, W. Paszkowicz, and M. Heinonen, J. Alloys and Compounds 286, 143 (1999)

[38] M. Wang, A.P. Huang, B. Wang, H. Yan, Z.Y. Yao, A. Morimito, and T. Shimizu, Mater. Sci. Eng. B85, 25 (2001)

[39] S. Yerci, M. Kulakci, U. Serincan, R. Turan, M. Shandalov, and Y. Golan, J. of Nanosci. Nanotechnol. 8, 759 (2008)

[40] L. X. Yi, J. Heitmann, R. Scholz, and M. Zacharias, Appl. Phys Lett. 81, 4248 (2002)

[41] W. Skorupa, L. Rebohle, and T. Gebel, Appl. Phys. A 76, 1049 (2003)

[42] M.K. Gunde, Physica B 292, 286 (2000)

[43] M. Modreanu, M. Gartner, E. Aperathitis, N. Tomozeiu, M. Androulidaki, D. Cristea, and P. Hurley, Physica E 16, 461 (2003)

[44] U. Serincan, S. Yerci, M. Kulakci, and R. Turan, Nucl. Instr. Meth. Phys. Res. B 239, 419 (2005)

[45] M.M Donald, *Handbook of PVD Processing*, Noyes, Westwood, NJ, 343 (1998)

[46] P.R. Wilmott, Prog. Surf. Sci. 76, 163 (2004)

[47] Institute of Materials & Machine Mechanics, Slovak Academy of Sciences, http://www.umms.sav.sk/ (Last visited 15/07/2009)

[48] A.S. Alagöz, *Synthesizing Germanium and Silicon Nanocrystals Embedded in Silicon Dioxide by Magnetron Sputtering Deposition Technique*, M.Sc. Thesis, Department of Physics, METU, Ankara (2007)

[49] VAKSIS, AR-GE and Engineering, http://www.vaksis.com/ (Last visited 19/07/2009)

[50] M. Kanuma, *Plasma Techniques for Thin Film Deposition,* Alfa Science, 243, USA, (2005)

[51] K.L Choy, Prog. Mater. Sci. 48, 57 (2003)

[52] Mems and Nanotechnology Exchange, http://www.mems-exchange.org/ (Last visited 27/07/2009)

[53] S. Perkowitz, *Optical Characterization of Semiconductors:Infrared, Raman, and Photoluminescence Spectroscopy,* Academic Pres, 159, London (1993)

[54] Albert Ludwigs University, Freiburg, Spectroscopy of Biologic molecules, http://www.biophysik.uni-freiburg.de/Spectroscopy/FTIR (Last visited 13/07/2009)

[55] A. Skoog Douglas, and M.West Donald, *Principle of Instrumental Analysis*, Saunders College Publishing, 252, USA (1992)

[56] K.T. Queeney, N. Herbots, J.M. Shaw, V. Atluri, and Y.J. Chabal, Appl. Phys. Lett. 84, 493 (2004)

[57] M. Trchova, J. Zemek, and K. Jurek, J. Appl. Phys. 82, 3519 (1997)

[58] A. Gencer Imer, S. Yerci, A.S. Alagoz, M. Kulakci, U. Serincan, T.G. Finstand, and R. Turan, J. Nanosci. Nanotechnol. 10, 525 (2010)

[59] D.V Tsu, G. Lucovsky, and B.N. Davidson, Phys. Rev. B 40, 1795 (1989)

[60] E. Dehan, P. Temple-Bojer, R. Henda, Pedroviejo, and E. Scheid, Thin Solid Films 266, 14 (1995)

[61] M. Zacharias, T Drusadau, A. Panckow, H. Freistedt, and B. Garke, J. Non-cryst. Solids 169, 24 (1994)

[62] S. Perkowitz, *Optical Characterization of Semiconductors: Infrared, Raman, and Photoluminescence Spectroscopy,* Academic Press, 105, USA (1993)

[63] J.R. Ferraro, R. Nakamoto, and C.W. Brown, *Introductry Raman Spectroscopy*, Academic Press, 256, London (2003)

[64] Wikipedia, Raman Scattering, http://www.scisoft.blogspot.com (Last visited 01/08/2009)

[65] K. Schoder Dieter, *Semiconductor Material and Device Characterization,* Wiley-Interscience Publication, 629, USA (1998)

[66] U. Serincan, *Formation of Semiconducor Nanocrystals in Silicon Dioxide by Ion Implantation,* Ph.D. Thesis, Department of Physics, METU, Ankara (2004)

[67] S. Yerci, I. Dogan, M. Genisel, S. Tokay, U. Serincan, A. Aydinli, and R. Turan, J. Appl. Phys. 100, 074301 (2006)

[68] S. Yerci, *Spectroscopic Characterization of Semiconductor Nanocrystals*, M.Sc. Thesis, Department of Physics, METU, Ankara (2007)

[69] B.E. Warren, *X-Ray Diffraction*, Addison-Wesley, USA (1969)

[70] Humboldt University, Berlin, c/ (Last visited 11/08/2009)

[71] W.L. Bragg, Prog. Cambridge Phil. Soc. 17, 43 (1913)

[72] P. Scherrer, Gottinger Nachrichten 2, 98 (1918)

[73] B.D. Cullity, *Elements of X-Ray Diffraction*, Addison Wesley, 365, Reading, MA (1978)

[74] K. Schoder Dieter, *Semiconductor Material and Device Characterization,* Wiley-Interscience Publication, 700, USA (1998)

[75] H. Bubert and H. Jenett, *Surface and Thin Film Analysis: Principles, Instrumentation, Applications*, Wiley-VCH, Weinheim (2002)

[76] S. Hufner, *Photoelectron Spectroscopy Principles and Applications*, Springer Verlag, Berlin (2002)

[77] D.A. Shirley, Phys. Rev. 55, 4709 (1972)

[78] S. Tougaard, Surf. Interface Anal. 11, 453 (1988)

[79] I. Doğan, *Fabrication and Characterization of Al_2O_3 And Si/Al_2O_3 Films with Si Nanocrystals Formed By Magnetron Co-Sputtering Technique,* M.Sc. Thesis, Department of Physics, METU, Ankara (2008)

[80] J. Wang, B. Zou, and M.A. El-Sayed, J. Mol. Struc. 508, 87 (1999)

[81] Y. Liu, T. P. Chen, Y. Q. Fu, M.S. Tse, J. H. Hsieh, P. F. Ho, and Y. C. Liu, J. Phys D: Appl Phys. 36, L97 (2003)

[82] J.S. Biteen, N.S. Lewis, H.A. Atwater, and A. Polman, Appl. Phys. Lett. 84 5389 (2004)

[83] U. Serincan, G. Aygun, and R. Turan, J. Lumin. 113, 229 (2005)

[84] P. Lange, J. Appl. Phys. 66, 201 (1988)

[85] C.T. Kirk, Phys. Rev. B 38, 1255 (1988)

[86] D.W. Berreman, Phys Rev. 130, 2193 (1963)

[87] D. Nesheva, I. Bineva, Z. Levi, Z. Areneva, Ts. Merdzahanova, and J.C. Pivin, Vacuum 68, 1 (2003)

[88] R. Turan and T.G. Finstand, Semicond. Sci. Technol. 7, 75 (1992)

[89] M. Yamamoto, T. Koshikawa, T. Yasue, H. Harima, and K. Kajiyama, Thin Solid Films 369, 100 (2000)

[90] S. Rivillon, Y.J. Chabal, F. Amy, and A. Kahn, Appl. Phys. Lett. 87, 253101 (2005)

[91] V. Drinek, J.Pola, Z. Bastl, and J. Subrt, J. Non-Crys. Solids 288, 30 (2001)

[92] H.C. Swart, E.D. Van Hattum, W. M. Arnoldbik, and F.H.P.M. Habraken Phys. Stat. Sol. C 1, 2286 (2004)

[93] J. F. Bobo, L. Gabillet, and M. Bibes, J. Phys: Condens. Matter 16, 471 (2004)

[94] W. Voit, W. Zapka, L. Belova, and K.V. Rao, Sci. Meas. Technol. 150, 5 (2003)

[95] C. Billotey, C. Wilhelm, M. Devaud, J.C. Bacri, J. Bittoun, and F. Gazeau, Magnetic Resonance in Medicine 49, 646 (2003)

[96] S. Ponce-Castaneda, J.R. Martínez, S. Palomares-Sánchez, F. Ruiz, O. Ayala-Valenzuela, and J.A. Matutes-Aquino, Sol-Gel Sci. Technol. 27, 247 (2003)

[97] B. Tural, M. Ozenbas, S. Atalay, and M. Volkan, J. Nanosci. Nanotechnol. 8, 861 (2008)

[98] S.J. Taol, H.S. Reehall, S.J. Webb, N.P.Barradas, and C. Jeynes, Thin Solid Films 343, 292 (1999)

[99] I. Preyra, C.A. Villacorta, M.N.P. Correno, R.J. Prado, and M.C.A. Fantini, Brazilian J. Phys. 30, 533 (2000)

[100] J. Tauc, R. Grigorovici, and A. Vancu, Phys. Stat. Sol. 15, 627 (1966)

[101] A. Mahmood, S. Muhl, R. Machorro, A. Lausa, J. Esteve, and J. Heiras, Diamond Relat. Mater. 15, 71 (2006)

[102] U. Coscia, G. Ambrosone, S. Lettieri, P. Maddalena, P. Rava, and C. Minarini, Thin Solid Films 427, 284 (2003)

[103] Q. Cheng and S. Xu, J. Appl. Phys. 102, 056101 (2007)

[104] S. Kerdiles, R. Rizk, F. Gourbilleau, A. Perez-Rodriguez, B. Garrido, O. Gonzalez-Varona, and R. Morante, Mater. Sci. Eng. B 69, 530 (2000)

[105] Y. Yang, J. Lin, C. H.A. Huan, Z.C. Feng, and S.J. Chua, Thin Solid Films 384, 173 (2001)

[106] S. Kerdiles, A. Berthelot, F. Gourbilleau, and R. Rizk, Appl. Phys. Lett. 76, 2373 (2000)

[107] D.W. Feldman, J.H. Parker, W.J. Choyke, and L. Patrik, Phys. Rev. 173, 787 (1968)
[108] S. Nakashima and H. Harima, Phys. Stat. Solidi (A) 162, 39 (1997)
[109] H. Zhang and Z. Xu, Thin Solid Films 446, 99 (2004)
[110] H. Zhang and Z. Xu, Optical Materials 20, 177 (2002)
[111] Z. Hu, X. Liao, H. Diao, G. Kong, X. Zeng, and Y. Xu, J. Cryst. Growth 264, 7 (2004)
[112] T. Rajagopalan, X. Wang, B. Lahlouh, C. Ramkumar, P. Dutta, and S. Gangopadhyay, J. Appl. Phys. 94, 5252 (2003)
[113] N.A.E. Forhan, M.C.A. Fantini, and I. Preyra, J. Non-Cryst. Solids 338, 119 (2004)
[114] R.J. Prado, T.F. D'Addio, M.C.A. Fantini, I. Preyra, and A.M. Flank, J. Non-Cryst. Solids 330, 196 (2003)
[115] C.-C. Liu, C. Lee, K-L Cheng, H.-C. Cheng, and T.-R. Yew, Appl. Phys. Lett. 66, 169 (1995)
[116] Q. Wahab, L. Hultman, I.P. Ivanov, M. Willander, and J.-E. Sundgren, Thin Solid Films 261, 317 (1995)
[117] P. Mandarcci, A. Chiodoni, G. Cicero, S. Ferrero, F. Giorgis, C.F. Pirri, G. Barucca, P. Musumeci, and R. Reitano, Appl. Surf. Sci. 184, 43 (2004)
[118] Q. Cheng, S. Xu, J.W. Chai, S.Y. Huang, Y.P. Ren, J.D. Long, P.P. Rutkevych, and K. Ostrikov, Thin Solid Films 516, 5991 (2007)
[119] M. Wang, A.P. Huang, P.K. Chu, B. Wang, and H. Yan, Diamond Relat. Mater. 16, 826 (2007)
[120] M. Losurdo, M. Giangregorio, P. Capezzuto, G. Bruno, and F. Giorgis, J. Appl. Phys. 97, 103504 (2005)
[121] B. Recha, T. Repmann, M.N. van den Donker, M. Berginski, T. Kilper, J. Hupkes, S. Calnan, H. Stiebig, and S. Wieder, Thin Solid Films 511, 548 (2006)
[122] M. N. van den Donker, S. Klein, B. Rech, F. Finger, W. M. M. Kessels, and M. C. M. van de Sanden, Appl. Phys. Lett. 90, 183504 (2007)
[123] W. Beyer, J. Hupkes, and H. Stiebig, Thin Solid Films 516, 147 (2007)
[124] Y. Mai, S. Klein, X. Geng, M. Hulsbeck, R. Carius, and F. Finger, Thin Solid Films 501, 272 (2006)

[125] S. Klein, R. Carius, F. Finger, and L. Houben, Thin Solid Films 501, 169 (2006)
[126] Y. Huang, A. Dasgupta, A. Gordijn, F. Finger, and R. Carius, Appl. Phys. Lett. 90, 203502 (2007)

[127] D. Song, E.-C. Cho, Conibeer G, Y. Huang, C. Flynn, and M. Green, J. Appl. Phys. 103, 083544 (2008)
[128] S. Yerci, U. Serincan, I. Dogan, M. Genisel, A. Aydinli, and R. Turan, J. Appl. Phys. 100, 074301 (2006)
[129] L.V. Azaroff, *Elements of X-ray Crystallography*, McGraw-Hill, New York, NY, 552 (1968)
[130] A. Henry, I.G. Ivanov, T. Egilsson, C. Hallin, A. Ellison, O. Kordina, U. Lindefelt, and E. Janzen, Diamond Relat. Mater. 6, 1289 (1997)
[131] D. Song, E.-C. Cho, Y.-H. Cho, G. Conibeer, Y. Huang, S. Huang, and M.A. Green, Thin Solid Films 516, 3824 (2008)
[132] E.-C. Cho, M.A. Green, G. Conibeer, D. Song, Y.-H. Cho, G. Scardera, S. Huang, S. Park, X. J. Hao, Y. Huang, and L.V. Dao, Adv. Opto Electron. 2007 69578 (2007)
[133] C.-W. Jiang and M. A. Green, J. Appl. Phys. 99, 114902 (2006)
[134] E.-C. Cho, S. Park, X.J. Hao, D. Song, G. Conibeer, S.C. Park, and M.A.Green, Nanotechnol. 19, 245201 (2008)
[135] Y. Kurokava, S. Tomita, S. Miyajima, A. Yamada, and M. Konagai, Jpn. J. Appl. Phys. 46, L833 (2007)
[136] D. Barba, F. Martin, C. Dahmoune, and G.G. Ross, Appl. Phys. Lett. 89, 034107 (2006)
[137] D. Riabinina, C. Durand, J. Margot, M. Chaker, G.A. Botton, and F. Rosei, J. Phys. Rev. B 74, 075334 (2006)
[138] S. Takeoka, M. Fujii, and S. Hayashi, Phys. Rev. B 62, 16820 (2000)
[139] N.A.P. Mogaddam, A.S. Alagoz, S. Yerci, R. Turan, S. Foss, and T.G.Finstand, J. Appl. Phys. 104, 124309 (2008)
[140] M. Zacharias, J. Heitman, R. Scholz, U. Kahler, and M. Schmidt, Appl. Phys. Lett. 80, 661 (2002)
[141] J.Y. Fan, X.L. Wu, and P. K Chu, Prog. Mater. Sci. 51, 983 (2006)

[142] D. Song, E.-C. Cho, G. Conibeer, Y.-H. Cho, Y. Huang, S. Huang, C. Flynn, and M.A. Green, J. Vac. Sci. Technol. B: Microelectron. Nanometer Struct.-Process. Meas. Phenom. 25, 1327 (2007)

[143] Y. Wang, H. Wang, and G. Ma, Thin Solid Films 335, 249 (1998)

[144] Y. Wang, J. Lin, C.H.A. Huan, Z.C. Feng, and S.J. Chua, Thin Solid Films 384, 173 (2001)

[145] D. Gracin, K. Juraic, P. Dubcek, A. Gajovic, and S. Bernstorff, Appl. Surf. Sci. 252, 5598 (2006)

[146] M. Marinow and N. Zotov, Phys. Rev. B 55, 2938 (1997)

[147] N. Kikuchi, E. Kusano, T. Tanaka, A. Kinbara, and H. Nanto, Surf. Coat. Technol. 149, 76 (2002)

[148] I. Dogan, I Yildiz, and R Turan, Physica E 41, 976 (2009)

[149] A. Markwitz, S. Jonson, M. Rudolphi, H. Baumann, and A. Mulklich, Appl. Phys. Lett. 86, 043107 (2005)

[150] Z.J. Zhang, K. Narumi, H. Naramoto, S. Yamamoto, and A. Miyashita, J. Phys D: Appl Phys 32, 2236 (1999)

[151] B.P. Swain, S.B. Patil, A. Kumbhar, and R.O. Dusane, Thin Solid Films 430, 186 (2003)

[152] W. Yu, W. Lu, L. Han, and G. Fu, J. Phys D: Appl. Phys. 37, 3304 (2004)

[153] C. Yuan, A.J. Steckl, and M.J. Loboda, Appl. Phys. 64, 3000 (1994)

[154] A. Gencer Imer, I. Yildiz, and R. Turan, Physica E, in press (2010)

[155] A. Gencer Imer, I. Yildiz, and R. Turan, Proceedings of the PVSEC, 425 (2009)

CURRICULUM VITAE

Surname, Name: Gencer İmer, Arife

Nationality: Turkish (TC)

Date and Place of Birth: 17 May 1977, İzmit

Marital Status: Married, 1 son

Address: Department of Physics, No:121, 06531, Ankara TURKEY

e-mail: agencer@metu.edu.tr

Phone: +903122104314

Fax: +903122105099

EDUCATION

2010-: Doctor of Phylosophy: METU, Ankara, Turkey (Cum. GPA: 3.18)

2005 - : Master of Science: Karaelmas University, Zonguldak, Turkey (Cum. GPA: 3.82)

1997 – 2001: Bachelor of Science: Gazi University, Ankara, Turkey (Cum. GPA: 83)

1994-1996: Pre-Bachelor Degree: Selçuk Universitesi, Konya, Turkey (Cum. GPA: 87)

EMPLOYMENT AND VISITING EXPERIENCES

2002 - : Research and Teaching Assistant at the Department of Physics, METU, Ankara, Turkey

2008 February-June: Visiting Researcher, Photovoltaic Department, Institute of Energy Research, Research Center Jülich, Germany

TEACHING EXPERIENCES

2002 - : Freshmen Physics Laboratory

2007: General Physics Laboratory for Physicists

ACADEMIC SKILLS

Experimental Techniques: Photoluminescence, Raman Spectroscopy, Fourier Transform Infrared Spectroscopy, X-Ray Diffraction, X-Ray Photoelectron Spectroscopy, Scanning Electron Microscopy, Magnetron Sputtering, Plasma Enhanced Chemical Vapur Deposition, Ion Implantation.

Scientific Awards: Dean's High Honor List of Students (for eight times).

Academic Interests: Solid State Physics (Theoretical & Experimental), Nano-Scale Physics, Photovoltaic, Medical Science.

CONFERENCE AND WORKSHOP ATTENDED

2009, 16-19 November: METU & TUD Research and Educational Network on Nanomaterials and Nanotechnology for Renewables, Ankara, Turkey

2007, 13-16 June: International workshop on SEMIconductor NANOstructures (SEMINANO), Bad Honnef, Germany.

2006, 16-20 October: Nanotechnology Research Forum, Ankara, Turkey.

2006, 9-13 September: XXVIII European Congress on Molecular Spectroscopy (EUCMOS), Istanbul, Turkey

2006, 21-23 June: International Workshop on Nanostructured Materials **(**NANOMAT), Antalya, Turkey.

2006, 3-5 May: Nanobilim and Nanoteknoloji II (NANO-TR II), Ankara, Turkey.

CONFERENCE AND WORKSHOP PRESENTATIONS

2009, 17 November: "SiC matrix with embedded Si nanocrystals for third generation solar cell", oral presentation, METU & TUD research and educational network on nanomaterials and nanotechnology for renewables, Ankara, Turkey

2007, 15 June: "Effects of hydrogen annealing on the photoluminescence characteristics of Si nanocrystals produced by ion implantation and magnetron sputtering", poster presentation, SEMINANO 2007, Bad Honnef, Germany.

2006, 12 June: "Evolution of Si-O-Si asymmetric stretching mode of SiO_2 during Si and Ge nanocrystal formation by sputtering and ion implantation." poster presentation, XXVIII European Congress on Molecular Spectroscopy (EUCMOS), Istanbul, Turkey

EXTRACURRICULAR ACTIVITIES

Hobbies: Taekwon-do, basketball, driving, literature, philosophy, and scientific magazines reading.

Foreign Languages: Fluent English and elementary German

LIST OF PUBLICATIONS

1. "Evolution of vibrational modes of SiO_2 during the formation of Ge and Si nanocrystals by ion implantation and magnetron sputtering", **A. Gencer Imer**, S. Yerci, A. S. Alagoz, M. Kulakci, U. Serincan, T.G. Finstand, and R. Turan, J. Nanosci. Nanotechnol. 10, 525 (2010)

2. "Evolution of SiO_2/Ge/HfO_2(Ge) multilayer structure during high temperature annealing", D. Sahin , I. Yildiz, **A. Gencer Imer**, G. Aygun, A. Slaoui, and R. Turan, Thin Solid Flims 518, 2365 (2010)

3. Book Chapter, "Characterization of Si nanocrystals", S. Yerci, I. Dogan, A. Seyhan, **A. Gencer Imer**, and R. Turan, Chapter 21 in Silicon Nanocrystals: Fundamentals, Synthesis and Applications, Wiley-VCH Verlag GmbH & Co. KGaA, Weinheim, (2010) ISBN: 978-3-527-32160-5.

4. “Fabrication and characterization of Si nanocrystal in SiC for third generation Solar Cells”, **A. Gencer Imer**, I. Yildiz, M. Karaman, and R. Turan, Proc. of the 24th European Photovoltaic Solar Energy Conference (24PVSEC), Hamburg, Germany, 425 (2009)

5. “Si nanocrystal in SiC for third generation solar cells” **A. Gencer Imer,** I. Yildiz and R. Turan, in press (2010) Physica E

6. “The effect of post annealing on the formation of Si nanocrystal in sputtered multilayer films” **A. Gencer Imer,** I. Yildiz and R. Turan, submitted J. Vacuum Sci. Technol.

6. “Photoluminescence from Si nanocrystals embedded in SiO_2 matrix in weak quantum confined regime”, N. A. P Mogaddam, A. Seyhan, **A. G. Imer**, R. Turan, submitted to J. Appl. Phys.